Signal Processing for Time Series of Functional Magnetic Resonance Imaging

by

Quan Zhu

Department of Electrical and Computer Engineering
Duke University

Date:_____

Approved:

_____
Jeffery Krolik, Supervisor

_____
Weili Lin

_____
Leslie Collins

_____
Rebecca Willet

_____
Stephen Smith

Dissertation submitted in partial fulfillment of
the requirements for the degree of Doctor
of Philosophy in the Department of
Electrical and Computer Engineering in the Graduate School
of Duke University

2008

ABSTRACT

Signal Processing for Time Series of Functional Magnetic Resonance Imaging

by

Quan Zhu

Department of Electrical and Computer Engineering
Duke University

Date:_____

Approved:

_____
Jeffery Krolik, Supervisor

_____
Weili Lin

_____
Leslie Collins

_____
Rebecca Willet

_____
Stephen Smith

An abstract of a dissertation submitted in partial
fulfillment of the requirements for the degree
of Doctor of Philosophy in the Department of
Electrical and Computer Engineering in the Graduate School
of Duke University

2008

Abstract

As a non-invasive method, functional MRI (fMRI) has been widely used for human brain mapping. Although many applications have been done, there are still some critical issues associated with fMRI.

Perfusion-weighted fMRI (PWI) with exogenous contrast agent suffered from the problems of recirculation, which could contaminate the cerebral blood flow (CBF) estimation and make its ability of prediction "tissue-at-risk" in debate. We propose a rapid and effective method that combines matched-filter-fitting (MFF) and ICA where ICA was used for regions with a prolonged TTP and MFF was utilized for the remaining areas. The calculation of cerebral hemodynamics afterwards demonstrates that the proposed method may lead to a more accurate estimation of CBF. The extent to which CBF is reduced in relationship to normal values has been utilized as an indicator to discern ischemic injury. However, despite the well known difference in CBF between gray and white matter, relatively little attention has been given as to how CBF may be differently altered in gray and white matter during ischemia due to the inability to accurately separate gray and white matter. To this end, we propose a robust clustering method for automatic classification of perfusion compartments. The method is first to apply a robust principal component analysis to reduce dimension and then to use a mixture model of multivariate T distribution for clustering. Our results in ischemic

stroke patients at the hyperacute phase show the clear advantage over the conventional technique.

BOLD fMRI, as a feasible and preferred method for developmental neuroimaging, is seldom conducted in pediatric subjects and therefore the information about brain functional development in the early age is somewhat lacking. To this end, this dissertation also focuses on how functional brain connectivity may be present in pediatric subjects in a sleeping condition. We propose a statistical method to delineate frequency-dependent brain connectivity among brain activation regions, and an automatic procedure combined with spatial ICA approach to determine the brain functional connectivity. Our results suggest that functional connectivity exists as young as two weeks old for both sensorimotor and visual cortices and that functional connectivity is highly age-dependent.

Contents

List of Tables

List of Figures

1. Introduction: Magnetic Resonance Imaging

Magnetic resonance imaging (MRI) has been well recognized as one of the most powerful tools to diagnose a wide range of pathologic conditions throughout the entire body, such as cancer, heart and vascular diseases, stroke, functional disorders, and so on [1-9]. This section will outline the basic principles of MRI and several representative applications in the area of functional magnetic resonance imaging (fMRI).

1.1 Nuclear Spins

Similar to electrical charges and mass, spin, which comes in multiples of ½ and can be either positive or negative, is one of fundamental properties of nature. Subatomic particles (electrons, protons and neutrons) possess spin, but most spins are paired against each other, and only individual unpaired electron, proton, or neutron possesses a spin of ½. A nucleus with unpaired protons and/or neutrons will have an overall nuclear spin and its quantum number I equals to half of the total unpaired number. The spin states of the nucleus or the so-called magnetic quantum number are defined as

$$\mathrm{m}=\{I, (I-1), \ldots, -I\} \tag{1.1}$$

and the corresponding energy is given by

$$E = -mhf \tag{1.2}$$

where Plank's constant h=6.626×10^{-34} J·s. A nuclear spin gives the nuclei an angular momentum and an associated magnetic moment

$$\mu = \frac{\gamma I h}{2\pi} \tag{1.3}$$

where γ is the gyromagnetic ratio and is different for different nucleus (γ=42.58 MHz/T for hydrogen). The induced magnetic moment interacts with its surroundings and is experimentally manipulated in the modern NMR experiments in order to provide MR signal. Due to its angular momentum, the nuclear spins process about the static magnetic field at the Larmor frequency

$$f = \frac{\gamma B_0}{2\pi} \tag{1.4}$$

where B_0 is the strength of the static magnetic field. It should be noted that the frequency of precession is proportional to the magnetic field strength.

The fact that fat and water contain many hydrogen atoms makes the human body, which primarily consists of fat and water, about 63% hydrogen atoms. It is the NMR signal from the hydrogen nuclei that MRI utilizes to produce images of *in vivo* tissue inside the body. We will focus on the hydrogen nuclei in the following discussion.

The hydrogen atom (H^1), which is abundant in the human body, has one unpaired proton and no unpaired neutron. Therefore, the hydrogen proton has a quantum number (*I)* of ½ and two spin states *m*={½, -½} with energy *E=-hf/2* and *hf/2*,

respectively. If there is no applied magnetic field, magnetic moments of all spins are randomly oriented and do not form any coherent magnetization (Figure (a)). When an external magnetic field is applied, hydrogen spins tend to either align with (parallel) or opposite (antiparallel) to the field, i.e., at the states of low energy or high energy, as illustrated in Figure (b). The population distribution in the two energy states are determined by thermal energy and characterized by the Boltzmann statistics

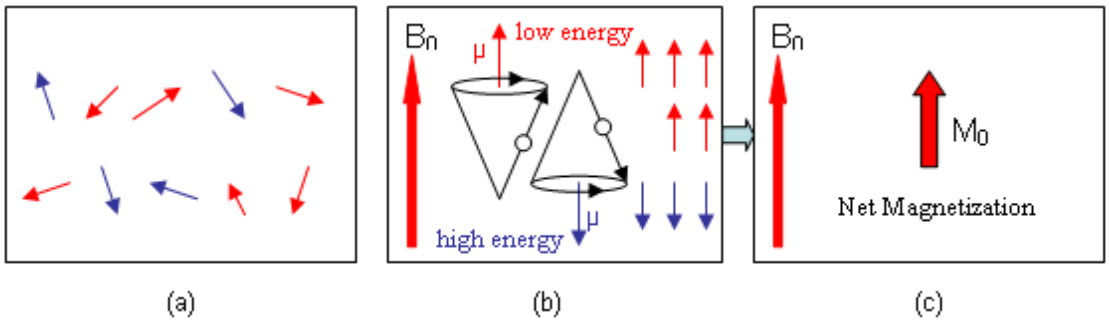

Figure 1. Randomly oriented spins without the presence of a magnetic field (a); Parallel (low energy) or anti-parallel (high energy) aligned spins (b), and the corresponding net magnetization (c) in the presence of a magnetic field.

$$\frac{N_+}{N_-} = e^{-\frac{\Delta E}{kT}} \tag{1.5}$$

where N_+ and N_- denote the total number of spins in the high and low energy states, respectively. Boltzmann's constant k is equal to 1.38×10^{-23} J/K; $\Delta E = hf$ is the energy difference between the two spin states; and T is the temperature in Kelvin. It is not

surprising that the low energy state is slightly preferred than that of the high energy state, resulting in a net magnetization, which is proportional to the population difference between the two energy states (Figure (c)). The spin can transit between the two energy states by absorption or emission of energy ($== hf$).

1.2 Magnetic Resonance (MR)

In the presence of a static magnetic field B_0 which results in a net Magnetization M_0, a small time-varying magnetic field (B_1) with a frequency (RF) identical to the Larmor frequency can be applied to promote some of the spins that are originally in the low energy state to the high energy state. If the RF field is switched off, the spins will return to the equilibrium condition.

The process that the spins return to the equilibrium condition from their excited state is called relaxation. There are two major relaxation processes. The first one, called T_1 or spin-lattice or longitudinal relaxation. After the application of a 90º excitation pulse, the magnetization will return to its equilibrium condition, governing by the equation (Figure (a))

$$M_z(t) = M_0(1 - e^{-t/T_1}) \tag{1.6}$$

or

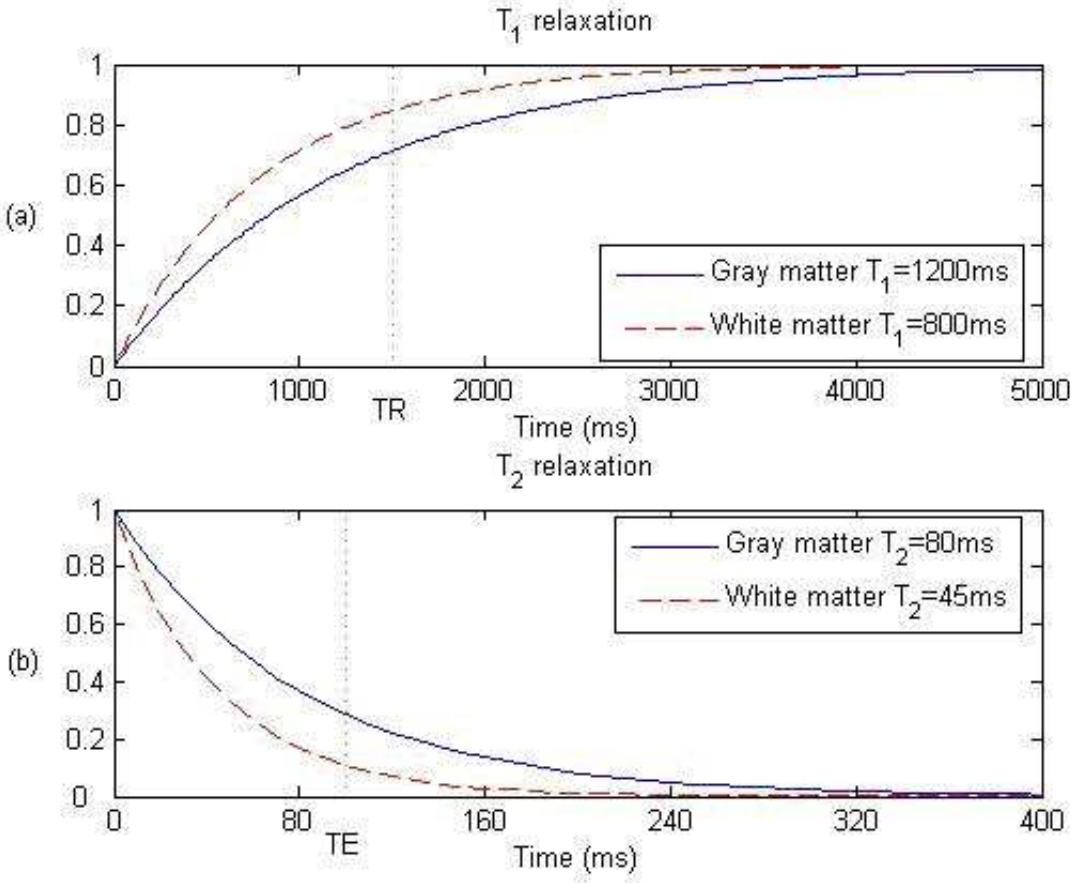

Figure 2. T1 spin-lattice relaxation (a) and T2 spin-spin relaxation (b)

$$M_z(t) = M_0(1 - 2e^{-t/T_1}) \tag{1.7}$$

if the excitation pulse is 180º. The T_1 relaxation is due to the interaction between spins and their environment. M_0 is the net magnetization at the thermal equilibrium state. If the time between two excitation pulses, referred as the repetition time (TR), is shorter than T_1, the magnetization will only be partially restored prior to the next excititation,

$$M_z(t) = M_0(1 - e^{-TR/T_1}) \tag{1.8}$$

As seen in Figure (a), the tissue with a short T_1 (white matter) recoveries faster than of the gray matter which has a longer T_1, leading to a higher signal for white matter than that of gray matter.

The second process is called T_2, spin-spin, or transverse relaxation. It is characterized by the decay of M_{xy} (transverse magnetization) to its initial value with the time constant T_2 (Figure (b)),

$$M_{xy}(t) = M_{xy0} e^{-t/T_2} . \tag{1.9}$$

Because T_2 varies for different biological tissues, it is imperative to choose a proper observation time, known as the echo time (TE), following the RF pulse. In a T_2-weighted image, tissues with a short T_2 (white matter) look dark because their signals decay away faster than those with a longer T_2 (gray matter) as shown in Figure (b).

Table 1 provides some typical values of T_1, T_2 and hydrogen density ϱ for different kinds of brain tissues [11]. It is noted that the concentration of hydrogen changes according to different tissue types and the net magnetization M_0 is proportional to its density value. Therefore, the NMR signal intensity, **I**, for a particular tissue is a function of T_1, T_2, ϱ, TR, and TE as described by

Table 1. Typical T1, T2 and ϱ values for brain tissues. *Based on r=111 for 12mM aqueous NiCl2

	T1 (s)	T2 (ms)	ρ*
Cerebro Spinal Fluid (CSF)	8 - 20	110 - 2000	70-230
White matter	0.76 - 1.08	45-100	70-90
Gray matter	1.09 - 2.15	61 - 109	85 - 125
Meninges	0.5 - 2.2	50 - 165	5 - 44
Muscle	0.95 - 1.82	20 - 67	45 - 90
Adipose	0.2 - 0.75	53 - 94	50 - 100

$$\mathbf{I} \propto \rho \cdot (1 - e^{-TR/T_1}) \cdot e^{-TE/T_2} \tag{1.10}$$

Up to now, we have not addressed how spatially resolved images are obtained using MRI. As mentioned previously, the resonance frequency of the spins depends largely on the magnetic field spins experienced. In other words, if a spatially dependent magnetic field is applied, spins at different locations will have a different resonance frequency. This is exactly the approach utilized in MR imaging to obtain spatially resolved images. By applying a magnetic field gradient across an object of interest,

different locations exhibit different resonance frequencies. As a result, Fourier transform can thus be used to obtain spatially resolved images.

1.3 Dynamic Susceptibility Contrast Perfusion-Weighted Imaging (DSC-PWI)

1.3.1 Background of DSC-PWI

PWI has been widely used as a means to reveal tissue perfusion information. In the context of our work, PWI has been used to determine regions in the brain exhibiting hypoperfusion in acute stroke patients. According to the Internet Stroke Center, stroke is the third leading cause of death and the primary cause of serious, long-term disability in the United States. About 88% of all stroke patients are caused by an abrupt blockage of arteries to the brain, namely ischemic stroke. Currently, tPA, the only thrombolytic drug approved by FDA can be given either intravenously within 3 hours or intra-arterially between 3-6hrs from symptom onset in an attempt to break up clots and restore blood flow. However, it has been shown that administering tPA is associated with an increased risk of cerebral hemorrhage. Therefore, it is imperative to determine whether stroke patients could actually benefit from the tPA prior to administering tPA.

The clinical evaluation could be done with the help of imaging techniques. The ultimate goal is to identify the brain area with perfusion deficit but is still viable and

likely saved by therapeutic intervention. Both conventional CT and MR techniques are not sensitive to access the presence of acute ischemic stroke [14, 19-21]. There is minimal signal change in CT for the first 24 to 36 hours and 6 to 12 hours after symptom onset using conventional MR. In contrast, diffusion- (DWI) and perfusion-weighted imaging (PWI) are relatively new MRI techniques and have become important in the assessment of acute stroke patients.

DWI, based on the measurement of water diffusion, can detect acute ischemic brain injury within minutes after stroke onset and PWI, highly sensitive to perfusion deficits, can identify regions with impaired perfusion. Typically, diffusion deficits indicate brain tissues with irreversible injury, while perfusion abnormality encompasses all of the tissues with reduced cerebral blood flow (CBF). If the area of perfusion abnormality is larger than that of diffusion abnormality, the mismatched area in Figure , has been postulated as the ischemic penumbra, indicating the region of salvageable brain tissues that can be restored if blood flow is re-established promptly. While diffusion lesion could be easily defined on DWI images, the assessment of perfusion abnormality is more complicated, involving quantification of perfusion data to estimate cerebral hemodynamics.

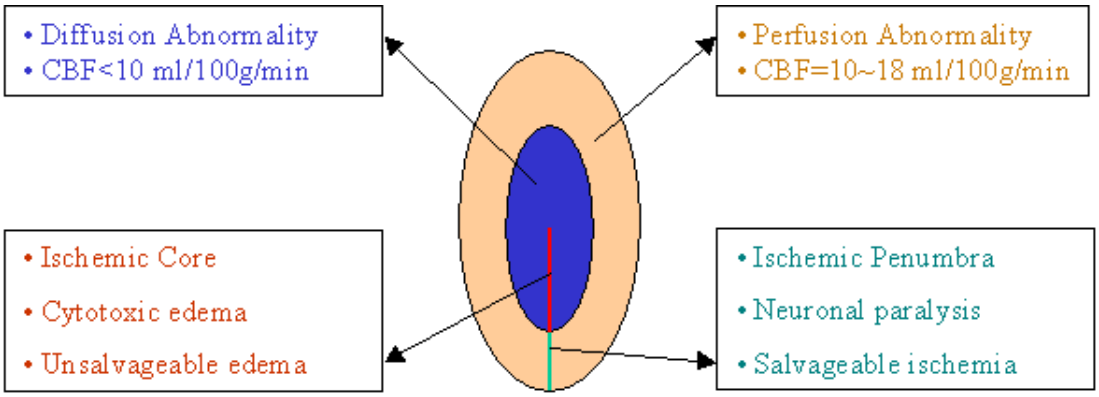

Figure 3. DWI/PWI mismatch

1.3.1.2 DSC-PWI technique

Perfusion is defined as the delivery rate of oxygen and nutrition from blood to the capillary beds of a block of tissue in a unit time (milliliters of blood per 100g of tissue per minute). It is typically characterized by three important hemodynamic parameters: cerebral blood volume (CBV), cerebral blood flow (CBF), and mean transit time (MTT) [1-3]. Dynamic susceptibility contrast magnetic resonance imaging (DSC-MRI) is a rapidly evolving technique and has already been widely used in the study of tissue perfusion [4-9]. DSC-MRI utilizes a bolus of paramagnetic contrast agent (for example, Gd-DTPA) that is injected intravenously, leading to a marked signal decrease in T_2^* / T_2 -weighted images. Specifically, MR signal in a predefined region-of-interest is attenuated

when the bolus of contrast agent passes through and returns to normal afterwards. By acquiring a series of images every 1-2s prior to (Figure (a)), during (Figure (b)) and after (Figure (c)) the injection of a contrast agent using a T2*-weighted gradient echo sequence, signal-vs.-time curves (Figure (d)), which consists of baseline signal, the first passage and the recirculation of the contrast agent, can be obtained pixel by pixel. Relative concentration time courses are subsequently converted from signal-vs.-time MR signal intensity and finally used to estimate CBV, CBF and MTT with a perfusion quantification model.

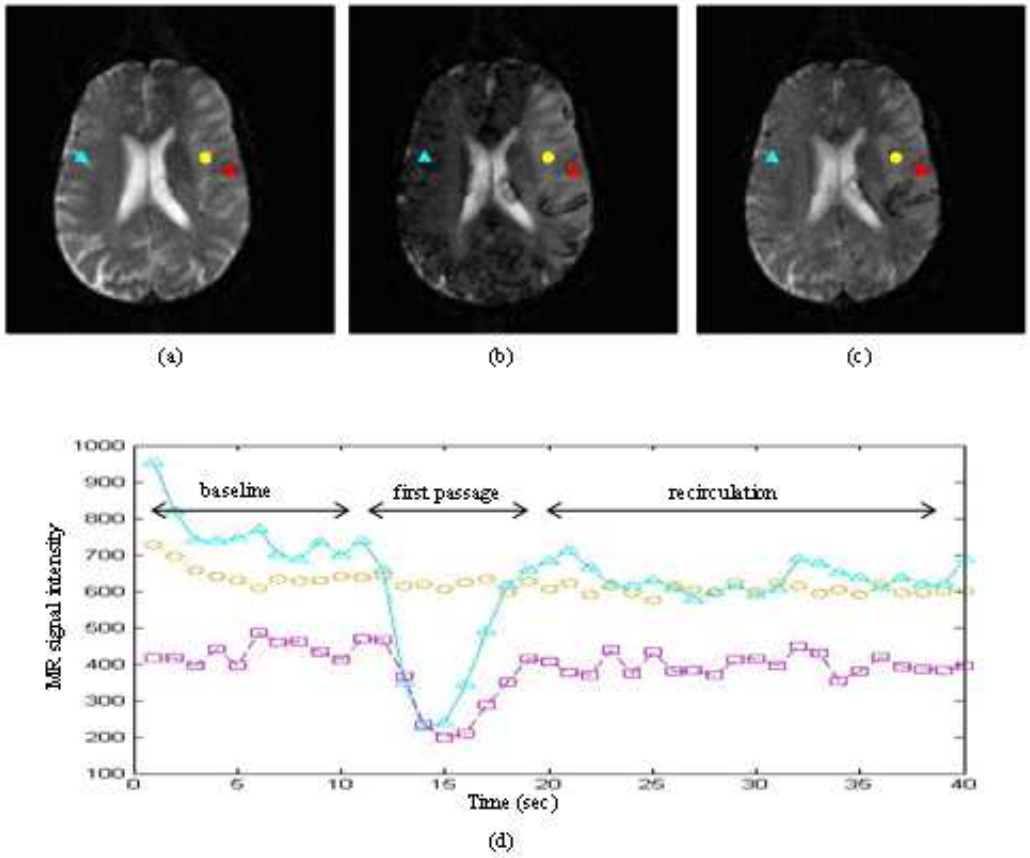

Figure 4. DSC-MRI images prior to (a), during (b) and after (c) the injection of a contrast agent, and the corresponding MR signal-vs.-time curves, which consist of baseline signal, the first passage and the recirculation of the non-diffusable contrast agent, in normal hemisphere (blue curve in (d)), penumbra (magenta curve in (d)) and core (yellow curve in (d)) of lesion area, respectively. Note that almost no contrast agent enters the ischemic center due to the very low CBF of that area.

There is a major assumption associated with this quantification model: the recirculation of the tracer is insignificant or eliminated. Several different approaches have been proposed to minimize the effects of recirculation, including the commonly

used gamma-variate fitting (GVF) [22-26] and the more recently proposed independent component analysis (ICA) [27]. While the GVF approach has been shown to work relatively well particularly for the normal brain regions, it suffers from two major limitations, including that it is time consuming (~2.5hrs for a typical study) and it may fail when the first passage and recirculation of the contrast agent are substantially overlapped i.e., in regions of compromised cerebral perfusion. Wu et al have recently proposed an ICA approach to minimize the effects of recirculation [27]. With both Monte Carlo simulation and acute stroke patient studies, they demonstrated that the ICA approach is capable of effectively minimizing recirculation even when the first pass and recirculation are substantially overlapped. Nevertheless, the computation time of the ICA approach remains long and impractical for routine clinical use (~2hrs). In addition, how recirculation may impact on the estimates of cerebral hemodynamics, particularly CBF remains elusive.

To this end, we propose a hybrid approach to minimize the effects of recirculation by combining a matched filter fitting (MFF) method and the ICA approach. Specifically, the MFF approach is used to minimize the effects of recirculation in the putative normal brain regions while the ICA approach is utilized for regions where an overlap between the first pass and recirculation is suspected. The effectiveness of the

proposed hybrid approach is evaluated using DSC images obtained from acute stroke patients.

1.3.1.3 Perfusion segmentation in DSC-PWI

CBF lesions could potentially more effectively identify the final infarction than MTT and CBV [15, 28]. For example, it has been suggested that regions with CBF below 10-12 ml/100g/min may represent irreversible injury. However, most of the studies to date have only focused on the whole brain analysis. Given the fact that there are significant differences in CBF values between white (WM) and gray matter (GM) in both normal and ischemic areas [29, 30], the global measures of CBF may confound the ability of CBF to predict final tissue outcome. In normal subjects, values of CBF in gray matter are around 40-60 ml/100g/min while those in white matter are about 20-25 ml/min/100g. These suggest that tissue-specific CBF thresholds could provide a more precise lesion map than one fix whole-brain threshold [31, 32].

Moreover, the extent to which CBF is reduced in relationship to the normal CBF values has been utilized as an indicator to discern ischemic injury. However, despite the well known difference in CBF between gray and white matter, relatively little attention has been given as to how CBF may be differently altered in gray and white matter during ischemia. The lack of attention is most likely attributed by the inability to accurately separate gray and white matter particularly during the hyperacute phase. To

this end, a robust clustering method is proposed for automatic classification of perfusion compartments. The robust clustering method is first to apply a robust principal component analysis (PCA) to reduce data dimension and then to use a mixture model of multivariate T distribution to cluster those reduced data. We then develop an Expectation-Maximization (EM) algorithm to efficiently and reliably perform mixture decomposition of multivariate T distribution.

1.3.2 BOLD-based functional connectivity MRI

Another MRI technique investigated in this thesis is blood-oxygen-level-dependent (BOLD) functional connectivity (fcMTI). Since its discovery, BOLD MRI has been widely employed as a powerful noninvasive tool to investigate brain function [33-35]. Although BOLD has been a popular approach to access function connectivity, few studies have been conducted in the pediatric population, particularly in the very young age group (0-2 years) [36]. The lack of studies in this age group is not surprising since external sensory/cognitive inputs and the cooperation of the subjects to perform or sense the specific sensory/cognitive inputs are required for BOLD MRI which are clearly difficult for subjects in these age groups to comply. As a result, our understanding of the brain function in these age groups is relatively lacking.

Unlike the conventional task-activation functional MRI, fcMRI has been used to obtain BOLD signals on subjects in a task-free or resting state. It has been reported that

fcMRI could detect cortical networks associated with motor, sensory and cognitive functions [17, 18, 37-39], even in the absence of a specifically cued task. These results suggest that the "resting" brain is never truly resting and a finite set of functionally related regions could be spatially located according to coherent brain activity.

1.3.2.1 Cross-correlation analysis on pediatric subjects

Biswal et al. [17] have observed the synchronization of low frequency BOLD signal (<0.08 Hz) in the brain. With rapid acquisition of a series of T_2*–weighted images while subjects lie resting inside the MR scanner and the use of a low pass filter (cutoff frequency 0.08 Hz), the resulting signal in a specific cortical region exhibits a high temporal correlation with other brain regions that are functionally similar. For example, the low-pass-filtered 'seed' signal from one voxel or a small region of interest (ROI) whose spatial location were chosen from the primary motor cortex exhibits high temporal correlation at the motor cortex areas in both hemispheres in the absence of a prescribed cognitive task. Therefore, Biswal et al. suggested that the observed BOLD synchronization in functionally similar brain regions may represent cortical connectivity.

Given the fact that fcMRI does not require subjects to follow specific instructions, and subjects are at a resting condition, this approach could be a powerful tool to delineate brain functional connectivity in young pediatric subjects. To this end, we

focus on how functional brain connectivity may be present in very young pediatric subjects (0-2yrs) in a sleeping condition. Specifically, we aim to investigate the following two questions: 1) does cortical functional connectivity exist in healthy pediatric subjects between 0-2yrs old and 2) if so, how does cortical functional connectivity change as a function of age? Our results suggest that functional connectivity exists as young as two weeks old for both sensorimotor and visual cortices and that functional connectivity is highly age-dependent.

Furthermore, we propose a statistical method rather than Fourier transform to depict putative brain connectivity among brain activation regions. Fourier transform decomposes a time series into a sum of sinusoids of different frequencies and forms a spectrum of its frequency components. By definition, Fourier transform cannot provide any timing information at which each frequency occurs, while the wavelet transform, as a powerful analysis tool to represent a signal as a sum of wavelets with different locations in time and scales, could identify not only frequency components but also the times at which they take place [40]. Due to its multi-resolution nature, the wavelet transform has a growing usage to enhance the power of statistical analysis of biological data [41, 42]. In this study, a highly redundant wavelet analysis approach: maximal overlap discrete wavelet transform (MODWT) is used to separate fcMRI time courses into multiple frequency ranges and their coefficients in time for further correlation

analysis. A robust regression model is then used to analyze Fisher's Z-transformed correlation coefficients data for each frequency. With the proposed statistical approach, we investigate the brain development in the early age and explore the estimation of frequency-dependent correlation matrices to characterize functional connectivity between sensory, motor and visual cortices in neonates (2-4 weeks), one and two years old children.

1.3.2.2 Spatial independent component analysis on pediatric subjects

Although it has been demonstrated that cross-correlation analysis (CCA) between between a seed signal and the whole brain on a voxel-by-voxel basis has been effective in delineating cortically connected regions, it suffers from two major shortcomings [43, 44]. First, the obtained functional connectivity maps show a high dependence on the selective of seed signals. Both the size and location of the chosen ROIs will affect the seed signals and, therefore, the outcomes of the resulting activation maps. Second, CCA is applied to each individual voxel independently and, thus, ignores the dependence between voxels.

As an effective alternative to circumvent the problems of the CCA approach, independent component analysis (ICA) requires no predefined seed signals or prior knowledge about spatial/temporal patterns of brain activity and performs a blind source separation based on 2nd and higher order relations among voxels. The rationale for the

application of the spatial ICA (sICA) to fcMRI is based on two complementary principles of brain functional organization: *localization* and *connectionism* [45]. *Localization* states that each individual function, e.g. motor, is localized to a small set of specific brain areas while *connectionism* represents that the brain activity associated with a given task may be the functional integration of activity in multiple brain regions. By maximizing both the statistical independence and the non-Gaussianity of the source signals, spatial ICA can decompose fcMRI signals into various sources consisting of a unique time course of activation and corresponding 3D component maps. Each brain function may be represented by one or more resulting spatially-independent sources.

Spatial ICA was first applied to fcMRI data analysis on anesthetized pediatric patients (5 to 12 years old) by Kiviniemi et al. [46] and then on normal adult subjects by van de Ven VG et al. [44] and Ma L et al. [43]. It has been reported in these studies that spatial ICA was able to identify functional connectivity in sensory and motor cortices, as well as in several parietal and frontal regions. The frequency analysis of function-related time courses showed a dominant peak at 0.03 Hz on anesthetized pediatric patients [46] and a prevailing frequency band within the extremely low range (0.01-0.05 Hz) on normal adults [44]. Moreover, based on the overall performance and the robustness to structured noise reported by Ma L et al., spatial ICA appears to be superior to CCA [43].

In this thesis, spatial ICA approach is applied on BOLD fcMRI data to examine the spatial, frequency, and connectivity characteristics of specific functional related cortices in neonates (2-4wks), one-year and two-years old children. This is an original study of functional connectivity on brain development in the early age of pediatric subjects with MRI techniques.

1.4 Main contributions

My doctoral research focuses on the signal processing and post analysis in time series of functional magnetic resonance imaging (fMRI) for human brain mapping. Two types of fMRI data are studied. One is the perfusion-weighted fMRI (PWI) with exogenous contrast agent: dynamic susceptibility contrast magnetic resonance imaging (DSC-MRI), which is promising to identify "tissue at risk" for acute stroke patients. The other is functional magnetic resonance imaging without exogenous contrast agent, based on blood oxygenation level dependent (BOLD) effect in functionally related brain regions, which is widely used for probing the functional connectivity of the human brain.

Although many applications have been done, there are still some critical issues associated with fMRI. PWI with contrast agent suffered from the present of recirculation, which could contaminate the cerebral blood flow (CBF) estimation and compromises its ability of prediction "tissue-at-risk". All of the existing approach cannot

minimize the recirculation quickly and correctly simultaneously. In addition, it is still unclear how recirculation affects the CBF estimation and thus the capability of predicting the tissue outcome. Moreover, although some studies have demonstrated that it is not accurate to define lesion areas by setting one CBF threshold for the whole brain, and the tissue specific thresholds are preferred, approaches allowing separately analyzing different brain tissues are lacking.

BOLD fMRI, as a feasible and preferred method for developmental neuroimaging, is rarely conducted in infants and toddlers subjects and therefore our understanding on brain functional development in the early age is somewhat lacking. In this doctoral research, there are four major contributions associated with time series of fMRI to address these issues. The overall organization of this dissertation is as follows.

In Chapter 2, the perfusion quantification model for the assessment of cerebral hemodynamics is first presented and the major problem: minimizing the recirculation effects associated with the existing applications is discussed. A hybrid approach combining both MFF and ICA is proposed to rapidly and correctly remove the recirculation effects. The efficiency and effectiveness of the proposed method are examined using clinical cases.

In Chapter 3, multiple clustering approaches for perfusion segmentation are described and evaluated. In order to correctly separate the WM and GM especially in

ischemic regions, a robust clustering method, which is less sensitive to high variance outlier profiles, is proposed. The performance is validated using synthetic data with/without outlier curves. Our results show a clear advantage of using the robust clustering method. Moreover, we apply our method to dynamic susceptibility contrast (DSC) MR perfusion data of ischemic stroke patients at the hyperacute phase and the results demonstrate its ability to separate gray and white matter in both pathological and non-pathological areas.

In Chapter 4, we focus on the brain functional connectivity study in pediatric subjects. CCA approach is applied to address 1) whether or not cortical functional connectivity exits in young and healthy children at 2wks, 1yr and 2 yrs old and 2) if so, how does it depend on age? Moreover, we propose a statistical method to delineate frequency-dependent brain connectivity among brain activation regions. To the best of our knowledge, this is the first study not only documenting the presence of cortical functional connectivity in very young healthy children, but also demonstrating how cortical functional connectivity increases in the developing brain.

In Chapter 5, spatial ICA is applied to fcMRI data to separate multiple physiological and artifact-related signal sources. The cortical connectivity maps and the activation time courses corresponding to the two specific functions: sensorimotor and

visual are investigated in three age-groups: neonates (2-4 weeks), one and two years old children.

In Chapter 6, we explore some extensions and discuss possible research arenas for future work.

2. Recirculation Minimization in DSC-PWI

Minimizing recirculation in dynamic susceptibility contrast perfusion weighted imaging should lead to more accurate estimates of cerebral hemodynamics including cerebral blood flow (CBF), cerebral blood volume (CBV), and mean transit time (MTT). Gamma-variate fit (GVF) is a commonly employed approach to minimize recirculation but it is time-consuming and may fail in regions of diminished CBF. An independent component analysis (ICA) approach has been recently proposed to circumvent the difficulties of GVF, especially in areas with hypoperfusion. While promising results have been shown with the ICA approach, computational time remains long (~2hrs), impractical for routine clinical use. In addition, the potential impacts of recirculation on CBF, CBV and MTT have not been evaluated. We propose a rapid and effective method that combines a matched filter fitting (MFF) method and the ICA approach where ICA was used for regions with a prolonged arrival time for the contrast agent and MFF was utilized for the remaining areas in the brain. Results obtained from acute stroke patients demonstrate that such a technique can effectively minimize recirculation for the entire brain with a much shorter computational time (~2.5 min). The calculation of cerebral hemodynamics demonstrates that the proposed method may lead to a more accurate estimation of cerebral hemodynamics, and therefore a more accurate prediction of final infarction areas.

2.1 Introduction

Cerebral perfusion is typically characterized by three important hemodynamic parameters: cerebral blood volume (CBV), cerebral blood flow (CBF), and mean transit time (MTT) [47, 48]. To obtain these parameters, the dynamic susceptibility contrast (DSC) perfusion weighted imaging (PWI) approach has been commonly employed [4, 49-53] where a bolus of paramagnetic contrast agent (for example, Gd-DTPA) is injected intravenously and a time series of MR images are acquired. The presence of a paramagnetic contrast agent results in a marked signal decrease in T_2^*/T_2 images. Therefore, by monitoring MR signal changes as a function of time allows an estimate of cerebral hemodynamics.

Typically, the signal-vs.-time curves in DSC images could be divided into several temporally separated segments, depending on the arrival and washout of the contrast agent. These segments include the baseline signal, a marked reduced signal, a gradual recovery of signal, an additional signal reduction but at a much less extent than the first observed signal reduction, and, finally, a complete recovery of the signal. For the calculation of cerebral hemodynamics, the first three segments, normally referred to as the first pass, are typically employed while the remaining two segments, also known as recirculation, are normally disregarded/removed. In cases when the first pass and recirculation are temporally well separated, recirculation removal is relatively

straightforward and can be accomplished either through an operator defined time point or the commonly used gamma-variate fitting (GVF) procedures [22-26]. In contrast, when cerebral hemodynamics is compromised such as in acute stroke patients, it is highly likely that the first pass substantially overlaps with recirculation [27], making it difficult to separate the two and leading to potentially inaccurate estimates of cerebral hemodynamics.

Several different approaches have been proposed to minimize the effects of recirculation, including the commonly used GVF [22-26] and the more recently proposed independent component analysis (ICA) [27]. While the GVF approach has been shown to work relatively well particularly for the normal brain regions, it suffers from two major limitations, including that it is time consuming (~2.5hrs for a typical study) and it may fail when the first passage and recirculation of the contrast agent are substantially overlapped i.e., in regions of compromised cerebral perfusion [27]. Wu et al have recently proposed an ICA approach to minimize the effects of recirculation [27]. With both Monte Carlo simulation and acute stroke patient studies, they demonstrated that the ICA approach is capable of effectively minimizing recirculation even when the first pass and recirculation are substantially overlapped. Nevertheless, the computation time of the ICA approach remains long and impractical for routine clinical use (~2hrs). In

addition, how recirculation may impact on the estimates of cerebral hemodynamics, particularly CBF remains elusive.

To this end, an effective approach capable of minimizing the effects of recirculation, independent of the presence or absence of ischemic lesions, and completing the entire data process procedures within a clinically acceptable time frame is highly desired. In this study, we propose a hybrid approach to minimize the effects of recirculation. This new approach combines a matched filter fitting (MFF) method and the ICA approach proposed by Wu et al [27]. Specifically, the MFF approach was used to minimize the effects of recirculation in the putative normal brain regions while the ICA approach was utilized for regions where an overlap between the first pass and recirculation was suspected. The effectiveness of the proposed hybrid approach was evaluated using DSC images obtained from acute stroke patients.

2.2 Data Acquisition

Ten acute stroke patients recruited as part of the clinical trials for neuroprotective agents were studied. Informed consent was signed and obtained from all subjects prior to the imaging studies. Perfusion-weighted imaging was done on a 1.5T clinical MR scanner (Vision, Siemens Medical Systems Inc.). A bolus of contrast agent (0.1 mmol/kg Gd-DTPA) was injected at a rate of ~2 ml/s by hands after the completion of the 5th scan while patients lay still inside the magnet. The perfusion-weighted DSC

images were acquired using a single shot echo-planar imaging sequence and a total of 12 slices were acquired. This sequence was repeated 40 times prior to, during and after the injection of the contrast agent. Other imaging parameters included repetition time (TR) = 2 sec, echo time (TE) = 47 msec, acquisition matrix = 128×128, field-of-view (FOV) = 220×220 mm2, slice thickness (TH) = 6 mm, and inter-slice distance = 1.5 mm.

T_1-weighted images were also acquired at the acute stage. The MR imaging parameters for T_1-weighted images were as follows: TR = 500 sec; TE = 12 msec; acquisition matrix = 256×256; FOV = 220×220 mm2; TH = 6 mm; and inter-slice distance = 1.5 mm. There is also a T_2-weighted images acquired at the one-month follow-up scan. The MR imaging parameters for T_2-weighted images were as follows: TR = 4 sec; TE = 99 msec; acquisition matrix = 256×256; FOV = 220×220 mm2; TH = 6 mm; and inter-slice distance = 1.5 mm.

2.3 Perfusion Quantification Model

The model used for perfusion quantification is based on the principles of tracer kinetics for intravascular paramagnetic contrast agent and relies on the assumption that the tracer remains within blood vessels due to an intact blood-brain barrier (BBB) [54-57]. Briefly, the MR signal-vs.-time curves S(t) can be converted into concentration time curves C(t) according to

$$C(t) = -\frac{k}{TE}\ln\left[\frac{S(t)}{S_0}\right] \tag{3.1}$$

where S_0 is the baseline MR signal and k is a proportionality constant [57]. The value of k depends on the tissue, contrast agent, field strength and the pulse sequence parameters, and is set to 1 ml/g here for the calculation of relative concentration.

The quantification of cerebral hemodynamics is of great importance for the study of ischemic stroke and other physiological phenomenon. CBV (ml/100g) is the fraction of tissue volume occupied by blood within one voxel.

$$CBV = \frac{\int C(t)dt}{\int C_a(t)dt} \tag{3.2}$$

where the arterial input function (AIF), denoted by $C_a(t)$ (100g/ml), is the concentration of the contrast agent in the supplying artery.

$$rCBV = \int C(t)dt \tag{3.3}$$

denotes the relative CBV. CBF (ml/100g/min) is the rate at which blood flows through the microvasculature of a region of tissue.

$$C(t) = CBF \cdot C_a(t) \otimes R(t) \;\; = C_a(t) \otimes \left(CBF \cdot R(t)\right) \tag{3.4}$$

The function $CBF \cdot R(t)$ is known as the impulse response function, where $R(t)$ is the residue function and refers to as the fraction of injected contrast agent that is still present in a region of tissue at time t following an ideal instantaneous unit bolus injection at

time t=0. By definition, $R(0)=1$ and therefore CBF is the value of the impulse response function at t=0. Transfer function is therefore defined as the negative derivative of $R(t)$ as $h(t)=-dR(t)/dt$.

MTT (min) is the mean transit time that the contrast agent spends while passing through a region of tissue and is equal to the ratio of CBV to CBF according to the central volume principle [58].

There is an important assumption for the use of this model regarding the relationship between MRI signal intensity, tracer concentration, residue function, CBV, CBF and MTT. It only considers the first passage of the contrast agent and assumes that the recirculation is negligible or eliminated. Violations of this underlying assumption will seriously affect the evaluation of cerebral hemodynamics and introduce large quantification errors. Thus it is very important to minimize the effects of recirculation prior to the estimation of cerebral hemodynamics.

2.4 Methods to Minimize The Effects of Recirculation

2.4.1 Gamma-variate Fitting (GVF)

The approach proposed by Wu et al was employed for GVF. More detailed descriptions can be found in reference [27]. In short, a simplified logarithm formulation of the gamma-variate function (Equation 3.5) was taken which was then fitted by a

linear regression using the Levenberg-Marquardt method [59, 60]. The initial values for A, B and C (Equation 3.5) were estimated such that the maximum and turning points of the gamma function corresponded to the maximum and turning points of the concentration time curve.

$$C_{\Gamma}(t) = \begin{cases} A \cdot (t - t_0)^B \cdot e^{-(t-t_0)/C} & t > t_0 \\ 0 & t \le t_0 \end{cases}$$
$$\log C_{\Gamma}(t) = \begin{cases} \log A + B \log(t - t_0) - (t - t_0)/C & t > t_0 \\ 0 & t \le t_0 \end{cases} \qquad 3.5$$

2.4.2 Independent Component Analysis (ICA)

Wu et al. [27] have recently proposed a temporal ICA approach to minimize recirculation effects by assuming that the concentration-time curves are a linear superposition of MR signals from arteries, veins, tissues, recirculation, noise and so on. More detailed descriptions of the ICA approach can be found in reference [27]; only steps pertaining to the current studies are given below. First, the temporal ICA was applied to each 5×5 region of interest (ROI) and this process was repeated throughout the entire brain. Second, independent components (IC) were considered as recirculation when the following criteria were met: a late arrival of the contrast agent; a small relative energy; and a large full-width-half-maximum (FWHM). Third, all of the ICs with a late arrival time and whose relative energies were less than the relative energy of the identified recirculation components were regarded as noise components. Finally, the

first passage of contrast agent was reconstructed using all of the ICs with the exception of the recirculation and noise components.

2.4.3 Matched Filter Fitting (MFF)

Before going through the details of the MFF method, parameters pertaining to this approach are defined below. As shown in Figure , time-to-peak (TTP) denotes the time point when the concentration-time curve reaches its maximum. Time-to-arrival (TTA) represents the onset of the bolus by searching from TTP backward for two successive values which have a relative concentration value less than 10% of the maximum relative concentration value. Left (LTP) and right (RTP) turning points of the concentration-time curve reflect the time points reaching the half maximum before and after TTP, respectively.

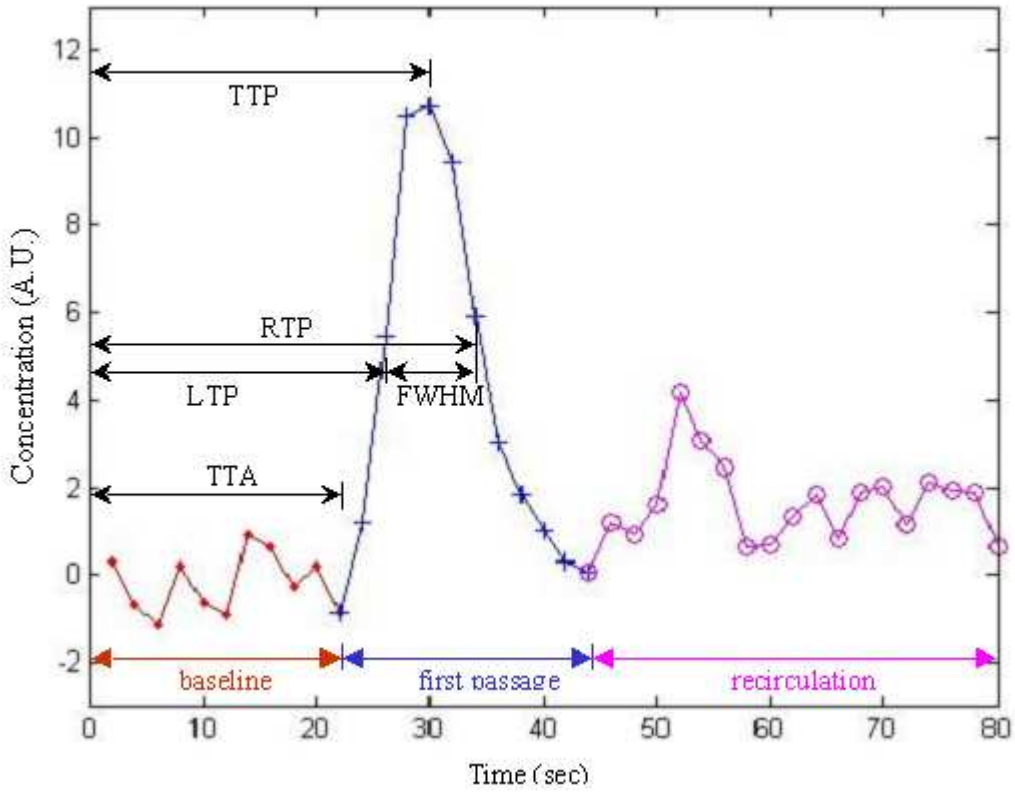

Figure 5. A representative example of the concentration time curve from an acute stroke patient is shown.

The underlying concept of the MFF method stems from the recognition that the first bolus passage could potentially be represented by a gamma-variate function [22-26]. Therefore, a library consisting of possible gamma-variate curves could be established in such a way that one of the gamma-variate curves in the library can best represent the experimentally obtained concentration curve, *C(t)*. Since the concentration curves could vary from subject to subject, the library consisting of the gamma-variate curves was

separately defined for each subject. Each library was obtained through the following three steps. First, mean TTP (TTP_C), TTA (TTA_C) and FWHM ($FWHM_C$) of the whole brain were estimated for each subject, respectively. Second, all of the possible values of *B, C and* t_0 (Eq. [2]) were obtained if the following criteria were met: $TTP_C - FWHM_C/2 < TTP < TTP_C + FWHM_C$; $TTP - FWHM_C < LTP < TTP$; $TTP < RTP < TTP + FWHM_C$; and $TTP - FWHM_C < TTA < LTP$. Parameter *A* was set to unity. Finally, each gamma curve was calculated for each set of these parameters and then set its norm to unity.

To enable MFF, $C(t)$ was projected to the above calculated gamma curves in the base library and the gamma curve $C_\gamma(t)$ with the maximum projection was regarded as the base of $C(t)$, i.e. $C_\gamma(t) = \arg\max\langle C(t) \cdot C_{base}(t) \rangle$. The MFF of $C(t)$ was finally obtained as

$$C_{MFF}(t) = C_\gamma(t) \cdot \langle C(t) \cdot C_\gamma(t) \rangle \tag{3.6}$$

It is immediately evident that the accuracy as well as the computation time of MFF depend on the selection of the time step to derive all of the possible values for *B, C and* t_0 in Eq. [2] (A was set to unity). The smaller the time step is, the more accurate but longer computation time will be. In order to quantitatively determine the interplay between the accuracy, computation time, and time step, time steps between 1/50 and 1/2 of TR with an increment of 1/100 of TR (=2sec in our study) were investigated. The root-mean-square (RMS) errors referring to as the square root of the mean squared deviation

of the fitted curve from the experimentally obtained signal as a function of the time step were calculated.

2.4.4 MFF+ICA Fitting

The main thrust of the proposed approach is to minimize the effects of recirculation for the entire brain independent of the presence or absence of compromised cerebral hemodynamics and to complete the entire data process procedures within a clinically acceptable time frame. To accomplish these two important goals, the MFF and ICA were utilized for each patient such that ICA was used in the lesion areas whereas MFF was applied in the remaining putative normal brain tissues. In this study, the lesion area was delineated using the TTP maps (Figure). Specifically, the mean and SD of the TTP of the left and right hemispheres of the brain were calculated, separately. The hemisphere with a lower mean TTP was considered as the normal hemisphere. Subsequently, pixels with a TTP greater than mean+SD of the normal hemisphere and located in the contralateral hemisphere were defined as the abnormal regions (AR). Finally, ICA was used to minimize recirculation in the AR areas while MFF was used for the remaining pixels, as illustrated in Figure (b).

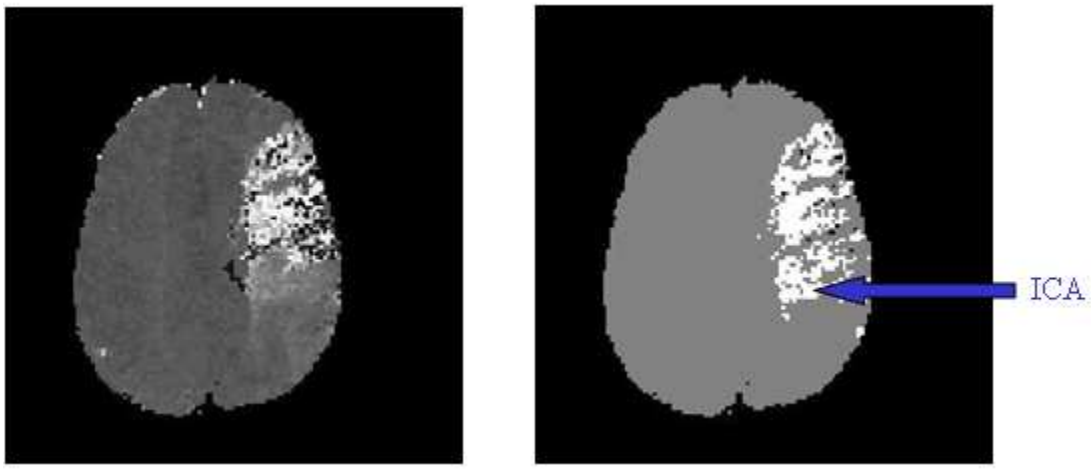

Figure 6. A representative example of the TTP map is shown in (a). With a TTP threshold of mean + SD of the normal hemisphere, the brain can be divided into two regions, the putative normal (gray, b) and the prolonged TTP (arrow, b) regions, respectively. To minimize effects of recirculation, the ICA was employed for the prolonged TTP area (arrow) while the MFF was used for the putative normal region (gray, b).

The major findings are 1) the MFF approach provides statistically comparable results when compared with that obtained using GVF but taking a much shorter processing time for the entire brain (<1 minute for MFF vs 2.5 hours for GVF). 2) The ICA approach is capable of minimizing recirculation in regions where compromised hemodynamics are anticipated whereas both the GVF and MFF fail, consistent with that reported by Wu et al [27]. 3) The proposed hybrid approach, ICA+MFF, successfully minimizes the effects of recirculation for the entire brain within ~3min. 4) Finally, CBF

can be substantially under-estimated while both CBV and MTT can be over-estimated if the effects of recirculation are not effectively minimized.

2.5 Comparisons of different methods of recirculation removal

In order to determine the effectiveness of the proposed recirculation removal method when compared to the currently existing methods, the computation time for recirculation removal and the CBV, CBF, and MTT obtained from each method were obtained. The CBF, CBV and MTT were calculated using the widely employed approaches as described by Ostergaard et al (4) and Wu et al [61] after recirculation was minimized. The arterial input function was chosen from the middle cerebral artery (MCA) in the normal hemisphere. Singular value decomposition with a block-circulant deconvolution matrix was used to deconvolve the concentration curves with the selected arterial input function [61].

To further examine how recirculation will affect the estimates of cerebral hemodynamics in relation to the extent to which the first pass and recirculation is overlapped, the AR regions were further divided into three sub-regions based on the degree of hypoperfusion. Specifically, the three regions were defined as: Reg 1 for mean+SD<TTP<mean+2×SD, Reg 2 for mean+2×SD<TTP<mean+3×SD, and Reg 3 for TTP>mean+3×SD, respectively, where the mean and SD corresponded to the mean and standard deviation of TTP in the normal hemisphere.

A paired t-test was employed to determine whether or not different approaches for recirculation removal resulted in statistical discrepancies for the calculation of cerebral hemodynamics. A $p<0.05$ was considered statistical significance.

All the algorithms described above were coded in Matlab (The Mathworks, Natick, MA) version 7.0.4 and executed on a Dell (Round Rock, Texas) GX270 with a Pentium 4 3.20GHz processor, 2GB of memory, and the Microsoft Windows XP Professional operating system (version 2002).

2.5.1 Comparison of GVF and MFF for recirculation removal

Figure illustrates the average computation time (Figure (a)) and RMS errors (Figure (b)) as a function of the time step used to define the MFF base library. Noted the computation time remains rather stable for all time steps >= 0.1xTR. However, the computation time increases exponentially when the time steps < 0.1xTR. In contrast, although the RMS using MFF is consistently lower than that of GVF for steps < 0.1xTR, the differences between the two approaches are minimal. Nevertheless, the RMS increases approximately linearly with the time steps for steps > 0.1xTR using MFF. Based on the tradeoffs between the accuracy and the computation time, a time step of 0.1xTR was chosen in our study to define the base library for all patients.

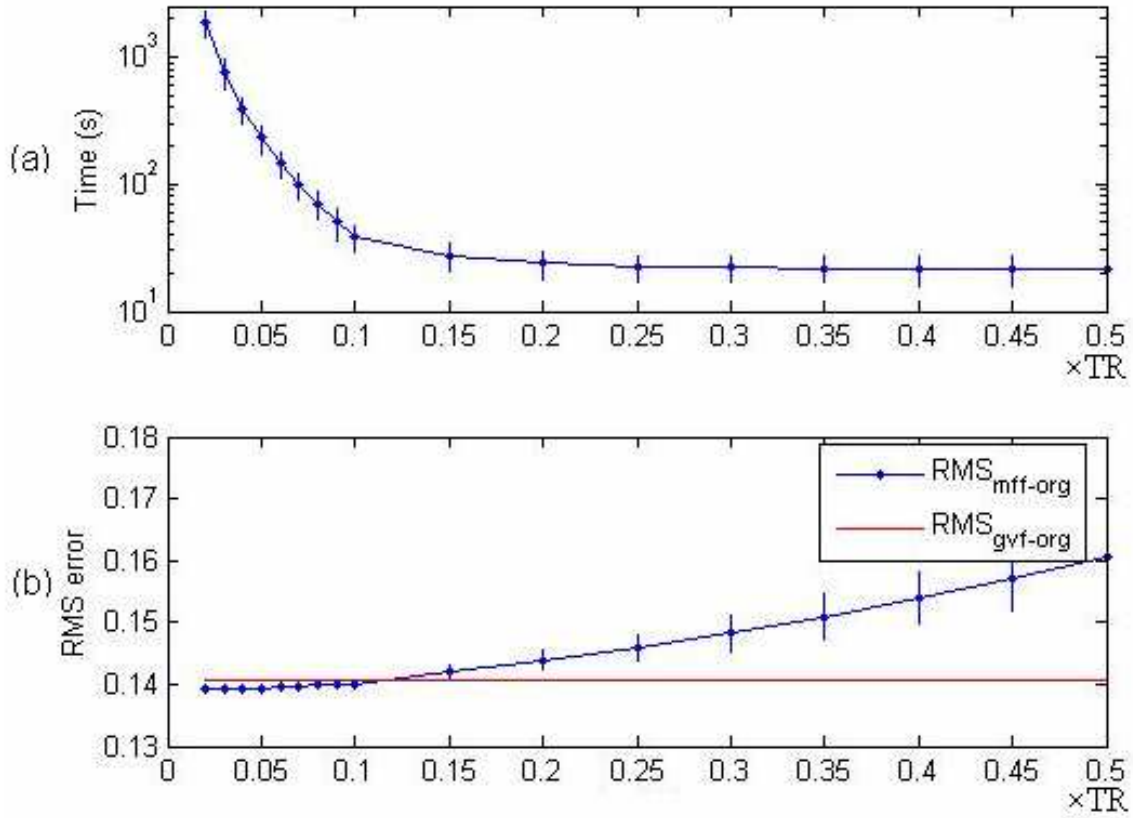

Figure 7. Computational time for MFF approach vs. time steps used to define the base library (a) and RMS errors between the fitted curves and the experimentally acquired concentration curves (b) for all patients.

2.5.2 Comparisons of GVF, MFF and ICA for recirculation removal

Figure demonstrates the effectiveness of recirculation removal among the three different approaches, GVF, MFF and ICA. A TTP map of an acute stroke patient is shown in Figure (a), delineating areas with prolonged TTP values (arrow). The corresponding concentration curves before and after recirculation removal using the

three approaches are shown for the normal (Figure (b)) and the prolonged TTP ROIs Figure (c), respectively. For the ROI with a normal TTP, the first passage and the recirculation of the contrast agent are temporally well separated (diamonds). As a result, all three methods successfully minimize recirculation. Moreover, the GVF (open circles) and MFF (crosses) achieve almost identical results although the GVF takes about 2.5hr whereas MFF only needs less than 1 min to complete recirculation removal. In contrast, for the prolonged TTP ROI (Figure (c)), both the GVF (open circles) and MFF (crosses) approaches fail to minimize the effects of recirculation and only the ICA is capable of minimizing recirculation. These findings suggest that all three methods provide similar results in the normal brain regions, while the ICA is superior to the other two methods in minimizing recirculation in regions with a prolonged TTP.

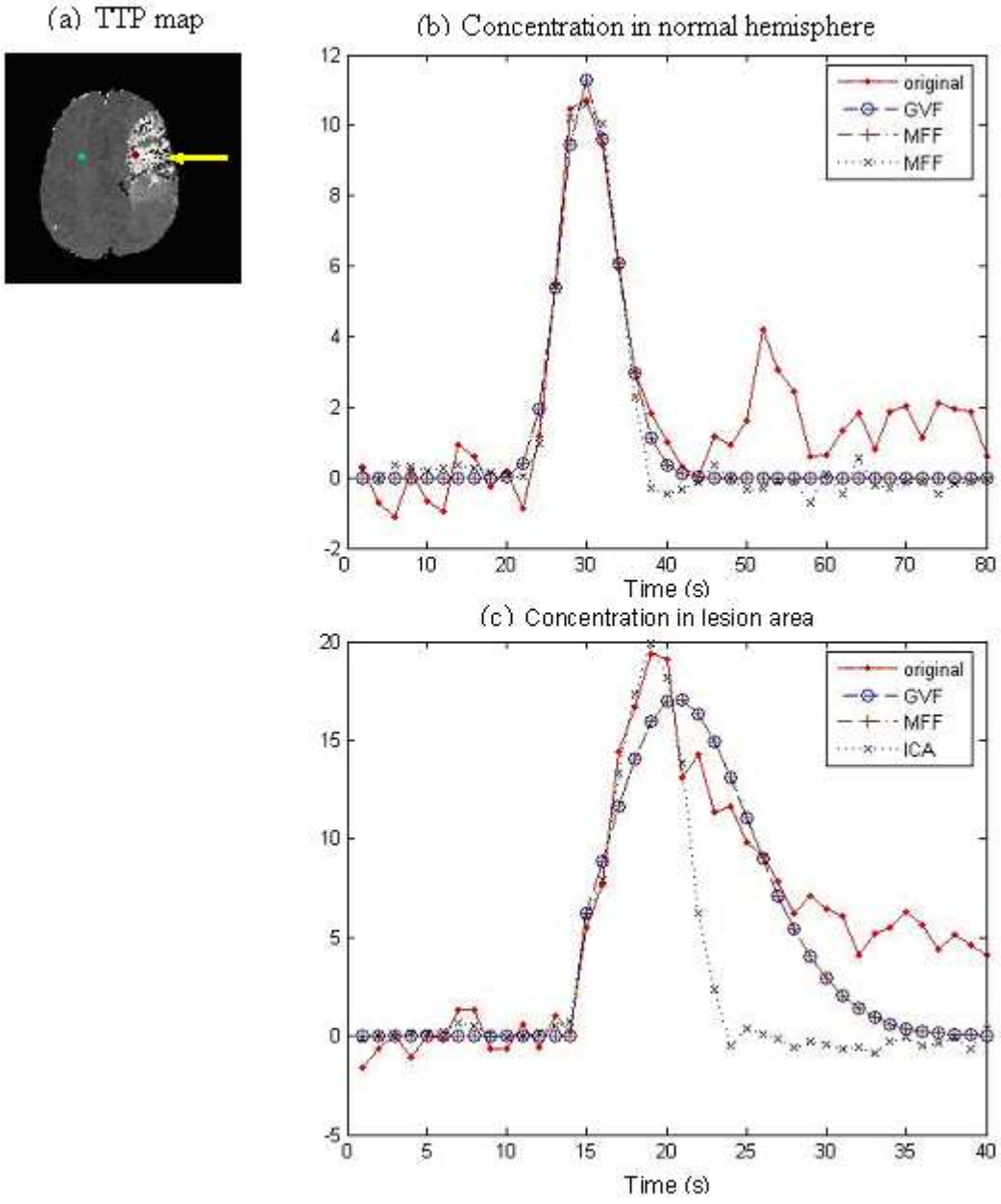

Figure 8. A TTP map of an acute stroke patient is shown in (a) delineating an ischemic lesion with a prolonged TTP. Two experimentally measured concentration curves from two ROIs, one for the normal and the other the prolonged TTP areas (arrow) are shown in (b) and (c) along with the concentration curves after recirculation is minimized using GVF, MFF, or ICA, respectively.

Table 2 summarizes the computation time for all patients using the GVF, ICA, MFF and the proposed MFF+ICA, respectively. The AR volume for all patients is 66.75±25.13cc. Clearly, both the GVF and ICA are time-consuming procedures and take on average ~2 hours for each patient. In contrast, MFF is the fastest approach while the proposed MFF+ICA approach completes the recirculation removal process within 3 minutes.

Table 2. Computation times for different approaches
GVF: gamma-variate fitting
ICA: Independent component analysis
MFF: Matched-filter fitting

Method	Time (mins)
GVF	149.17±27.55
ICA	115.26±17.09
MFF	0.43±0.06
MFF+ICA	2.47±0.97

2.5.3 Effects of recirculation on the estimates of CBF, CBV, and MTT

As shown in Figure , both the MFF and GVF approaches fail to effectively minimize recirculation in regions with a prolonged TTP, leading to potentially inaccurate estimates of cerebral hemodynamics. Figure compares CBV, CBF and MTT after minimizing recirculation using GVF, MFF and MFF+ICA, respectively. It is evident

that GVF and MFF provide very similar results for the estimates of CBF, CBV, and MTT (the relative differences are smaller than 1% for all of the three parameters). In addition, a higher MTT is observed using both GVF and MFF when compared with that obtained using the proposed hybrid approach. The discrepancies in CBF and CBV among the three approaches appear to be less remarkable although the normalized relative difference maps between MFF and MFF+ICA approaches clearly demonstrate the differences in CBF and CBV in the lesion area (fourth column, $\gamma_H = \frac{H_{MFF} - H_{MFF+ICA}}{H_{MFF}}$ where H represents CBF, CBV, or MTT).

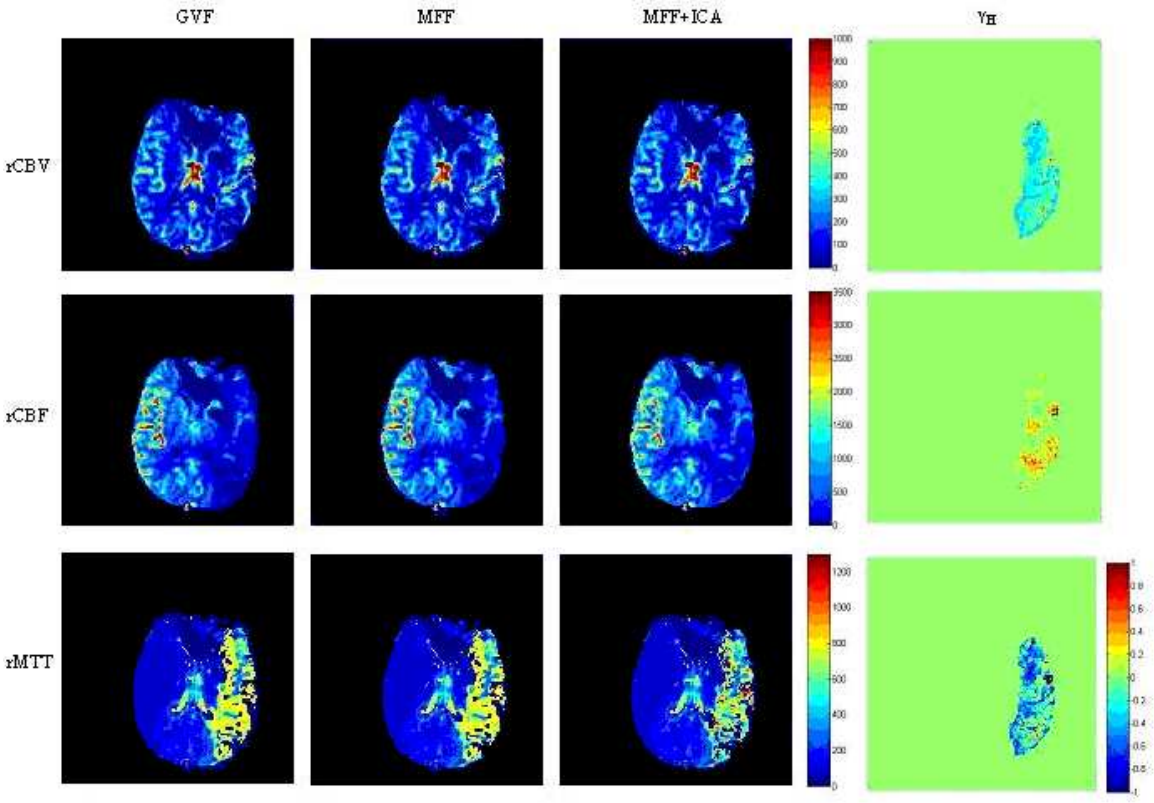

Figure 9. The comparisons of cerebral hemodynamics after minimizing the recirculation effects using three methods are shown: GVF (1st column), MFF (2nd column) and MFF+ICA (3rd column), respectively. The normalized relative differences between the MFF and the MFF+ICA processes are provided in the fourth column.

Table 3 summarizes how CBF, CBV, and MTT differ between the MFF and the proposed MFF+ICA in regions with a prolonged TTP. Specifically, the prolonged TTP areas were divided into three sub-regions based on the criteria outlined in the Materials and Methods section. As expected, CBF, CBV and MTT reduce as TTP becomes longer independent of the approaches used to minimize recirculation. In Reg 1, the proposed

MFF+ICA approach reveals a significantly higher CBF ($p<0.0001$), lower CBV ($p<0.0001$) and shorter MTT ($p<0.0001$) when compared with that obtained using the MFF approach. Similar findings are also observed in Reg 2 although the differences between the two approaches become smaller. Finally, with the exception of MTT ($p<0.007$), the CBF and CBV are statistically identical between the two approaches in Reg 3. The ratios of CBF, CBV and MTT between MFF+ICA and MFF for all three sub-regions are shown in Figure .

Table 3. Comparisons of CBF, CBV, and MTT using MFF and MFF+ICA approaches for the three sub-regions within the prolonged TTP areas

Reg 1: mean+SD < TTP < mean + 2SD
Reg 2: mean+2SD < TTP < mean + 3SD
Reg 3: mean+3SD < TTP
a: $p<0.0001$ between the two approaches
b:$p<0.007$ between the two approaches

	CBF (ml/min/100gm)		CBV (%)		MTT (sec)	
	MFF	MFF+ICA	MFF	MFF+ICA	MFF	MFF+ICA
Reg 1	15.48±4.37[a]	21.49±5.59	22.74±3.05[a]	16.52±2.87	8.46±1.07[a]	5.14±0.91
Reg 2	10.31±2.93[a]	13.16±3.54	16.27±2.79[a]	13.67±2.61	8.81±1.13[a]	6.53±0.87
Reg 3	6.60±2.41	7.56±2.47	10.68±1.02	10.09±0.93	9.09±1.17[b]	8.36±1.12

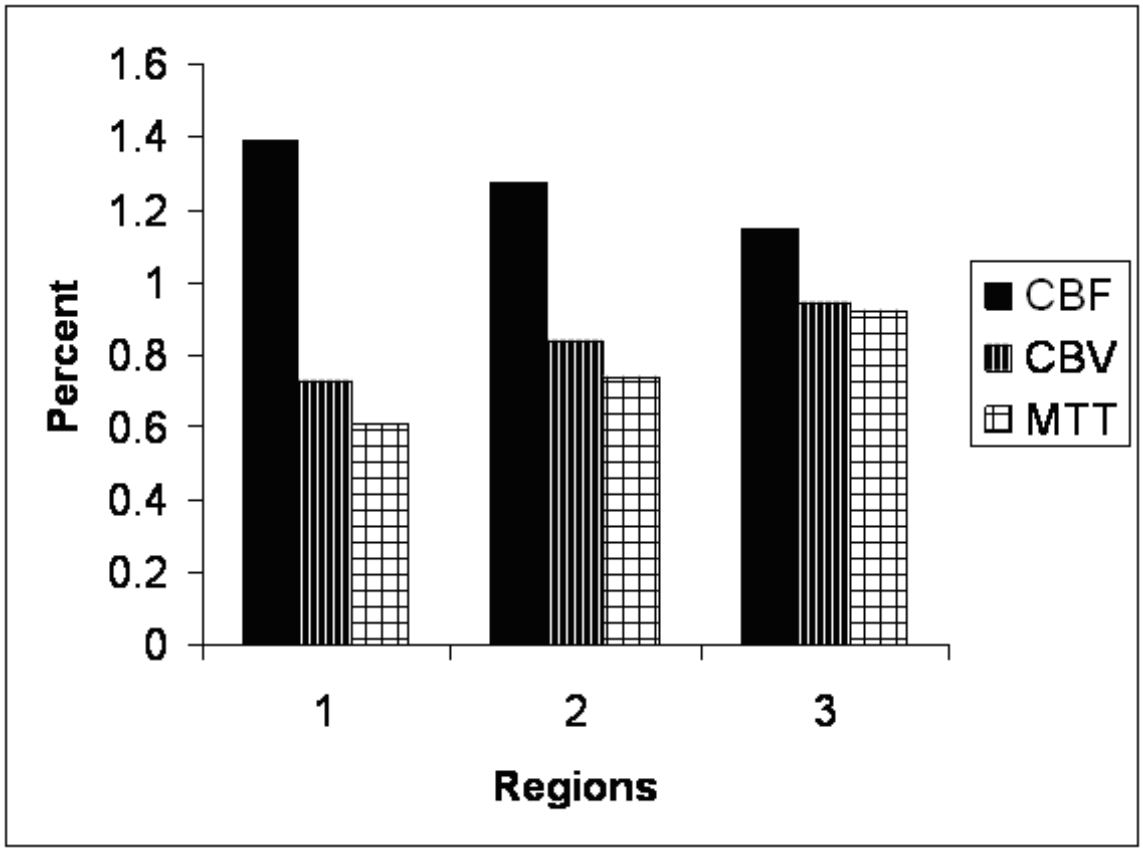

Figure 10. The ratios of CBF, CBV and MTT of the proposed approach to that obtained using the MFF are shown for the three sub-regions of the prolonged TTP regions.

2.5.4 Effects of recirculation on the prediction of infarction area

Infarction areas were manually defined on one-month follow-up T_2 images by a neurologist. ROC curves were used to evaluate the ability of CBF with different recirculation removal in predicting tissue outcome. Among all 10 patients, only 6 had the one-month follow-up scans and Figure 2 compare the ROCs using CBF maps with

and without recirculation removal. CBF with recirculation removal can improve its ability to predict final tissue infarction. More importantly, the proposed approach for recirculation removal works better than the conventional GVF.

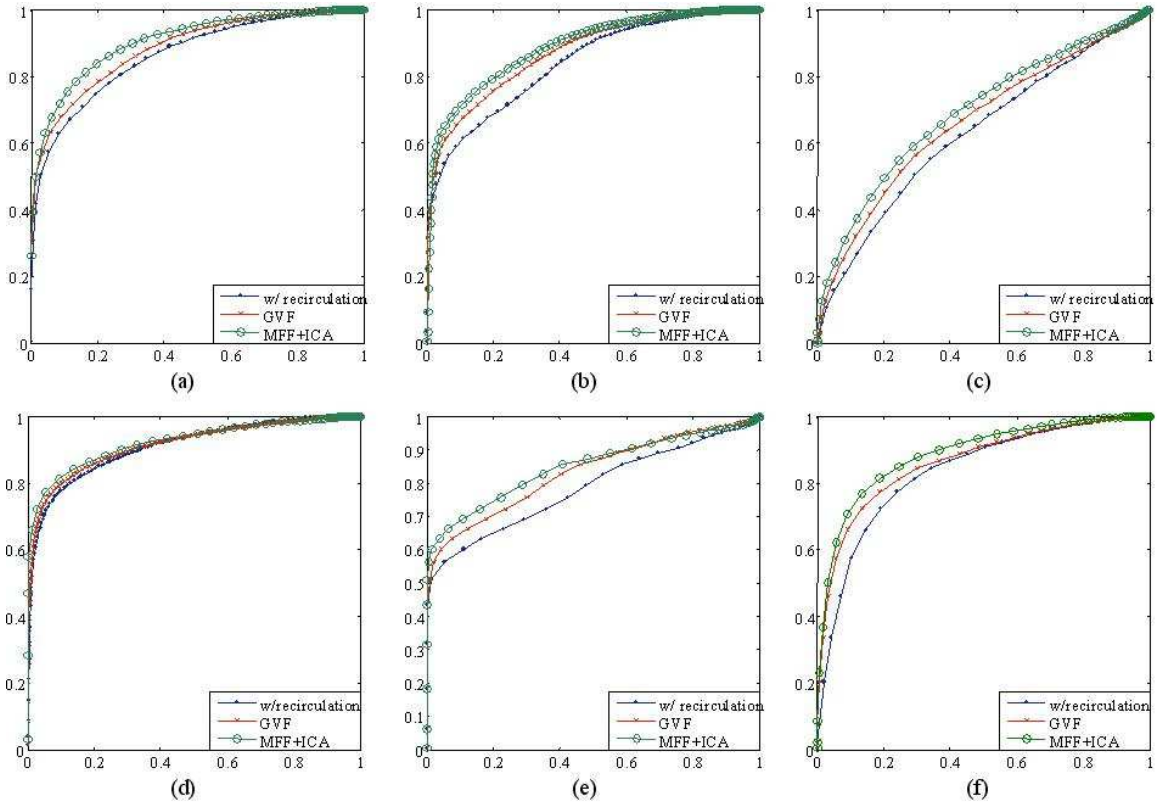

Figure 21. ROC curves for CBF in predicting of tissue outcome

Table 4 summarizes the area-under-curve (AUC) and standard deviation (SD) of lesion prediction using CBF maps in the presence of recirculation (recirc) and using GVF or MFF+ICA for recirculation removal, respectively. It is evident that the poorest

(smallest AUC) results are obtained without recirculation removal. While GVF improves the performance than that without recirculation removal, the new approach offers the best performance, indicating improved predictability of the final lesions. Table 5 illustrates the improvements of AUC among different CBF maps in predicting of final infarction areas. The improvement of AUC among different CBFs was compared using a 2-way ANOVA corrected for repeated measurement, while the estimated AUC was weighted by reverse of the corresponding SD. There is a significant improvement by minimizing the recirculation effects. Moreover, the newly developed approach, MFF+ICA, significantly improves the capability of predicting the final infarction in contrast to the conventional GVF method.

Table 4. Area under curve (AUC) and its standard deviation (SD) for CBF in predicting of tissue outcome.

Patient ID	AUC±SD		
	with recirculation	GVF	MFF+ICA
1	0.808±0.003	0.830±0.002	0.853±0.002
2	0.843±0.004	0.880±0.003	0.901±0.003
3	0.700±0.004	0.712±0.004	0.761±0.004
4	0.879±0.002	0.890±0.002	0.910±0.002
5	0.811±0.012	0.841±0.011	0.870±0.009
6	0.764±0.003	0.775±0.003	0.813±0.003
Average	0.8006	0.8213	0.8515

Table 5. Improvement of area under curve (AUC) among different CBFs in predicting of tissue outcome.

Patient ID	Improvement of AUC		
	recirc vs GVF	recirc vs MFF+ICA	GVF vs MFF+ICA
1	0.022	0.046	0.024
2	0.036	0.057	0.021
3	0.015	0.063	0.049
4	0.012	0.031	0.020
5	0.029	0.059	0.030
6	0.011	0.049	0.038
Average	0.0207	0.0508	0.0301
p-value*	0.0055	0.0004	0.0023

2.6 Discussion

A variety of studies with experimental animals have delineated quantitative changes in CBF and metabolism during and after transient focal ischemia. With middle cerebral artery (MCA) occlusion, brain tissues with CBF below 20 ml/100g/min demonstrate slowing of electrical activity and the appearance neurological deficits. Furthermore, brain regions with a CBF below 10-12 ml/100g/min exhibit loss of cell

membrane integrity manifested by K+ efflux and Ca2+ influx into cells, suggesting irreversible injury [62-72]. These studies suggest a potential relation between CBF values and physiological alterations. In addition, it has been implicated that tissues with CBF values within these two critical threshold values might be viable but nonfunctional, and this theoretical region has been known as the ischemic penumbra [73]. With these results, it is not surprising that many studies have utilized CBF to potentially access the extent of ischemic injury and identify regions of ischemia penumbra [74, 75]. However, one of the prerequisites for the utilization of CBF to provide insights into tissue injury is an accurate measure of CBF.

The accuracy of PET measured CBF has been well documented and PET CBF is considered as the gold standard for in vivo studies. However, an onsite cyclotron is required and the half-life of $^{15}H_2O$ is relatively short. As a result, the utilization of PET for delineating ischemic tissues in a routine clinical set up has been substantially limited to only major medical centers. In contrast, MR is widely available and can provide measures of CBF using either the DSC [47, 48] or the arterial spin labeling [76-78] approaches although improving the accuracy of MR measured CBF remains to be an active research direction. In the context of our study, we will focus our discussion on the DSC approach below.

Several different approaches have been proposed to further improve the accuracy of MR measured CBF using DSC. These studies include the choices of the arterial input function [79, 80], the utilization of SVD [50-52, 81] and cSVD [61] approaches, the minimization of large vessel effects [82], the utilization of frequency domain modeling of the residue function [83], and the derivation of a correction factor to minimize CBF variability resulted from inconsistent cardiac output [84]. While encouraging results on improving the accuracy of CBF estimates have been demonstrated using the above mentioned approaches, relatively little attention has been given as to how recirculation may contribute to errors for the estimates of CBF. In particular, regions with hypoperfusion are most likely to exhibit a substantial overlap between the first passage and recirculation of contrast agent, making it difficult to effectively minimize recirculation using the commonly employed GVF (Fig. 4) and leading to inaccurate estimates of CBF. Yet the status of CBF in these regions is perhaps the most clinically relevant since these regions encompass both ischemic core and penumbra. While the ICA approach proposed by Wu et al [27] is able to successfully minimize recirculation, how cerebral hemodynamics differ between the ICA and GVF have not been systematically evaluated.

Although comparable estimates of cerebral hemodynamics are observed in the putative normal areas for all approaches evaluated, substantial differences are observed

between the proposed hybrid and the MFF approaches (similar to the GVF approach) in regions with a prolonged TTP; the hybrid approach provides a significantly higher CBF than that obtained using the MFF (Table 2). In addition, the extent to which cerebral hemodynamics differ between the two approaches appears to depend on the TTP. This finding is perhaps not surprising since regions with a prolonged TTP are likely to suffer from overlapped first pass and recirculation. As a result, GVF and MFF will fail to delineate first pass from recirculation, leading to inaccurate estimates of cerebral hemodynamics. In the peri-lesion area (Reg 1), the proposed hybrid approach exhibits a CBF value which is 1.39 times higher than that using the MFF approach (Fig. 6). This finding could have profound clinical implications. For example, a region with a CBF value of 18 ml/min/100gm could be incorrectly interpreted as ~13ml/min/100gm when recirculation is not correctly minimized. The former CBF indicates that tissue may still be viable while the latter value may suggest the presence of ischemic core [62-72]. Although the differences between the two approach are somewhat reduced in Reg 2 (a factor of 1.28), the proposed approach remains to provide a significantly higher CBF when compared with that obtained using MFF. Although the CBF differences in Reg 3 between the two approaches do not reach statistical significance, one should be cautious in interpreting this finding. Specifically, given the diminished blood supply to the Reg 3, it will result in minimal MR signal changes, leading to potentially a poor signal-to-

noise ratio (SNR) for the estimates of CBF. Therefore, additional studies may be needed to further investigate how recirculation may impact on the estimates of CBF when the SNR is poor.

In contrast to CBF, the proposed hybrid approach results in a significantly shorter MTT in all three sub-regions in the AR areas while a significantly lower CBV in Reg 1 and 2 but a comparable CBV in Reg 3 when compared with that obtained using the MFF approach. These results are not surprising since the inability of minimizing recirculation using the MFF approach will most likely result in an overestimation of the areas of the concentration curves, leading to an elevated CBV and MTT. Note that the CBV values appear to be higher (Table 3) than the reported results in the literature. The potential partial volume associated with the choice of the arterial input function and the large vessel effects are most likely to explain the observed higher CBV values.

Consistent with the results reported by Wu et al [27], the GVF approach is as effective as the ICA approach in minimizing the effects of recirculation in normal tissues. Therefore, it seems to be logical to only employ the ICA approach for regions where a substantial overlap between the first pass and recirculation is anticipated whereas a different approach capable of minimizing recirculation with a much shorter period of time and providing similar results to that using GVF can be used for the remaining regions in the brain. In this study, we propose to replace the conventional GVF with the

MFF approach for recirculation removal of the normal brain tissues. MFF is a classical method for pattern detection which can be used to obtain the best-matched representation between the experimentally measured concentration curves and a carefully predefined series of gamma-variation functions. As shown in Table 2, the MFF approach on average takes less than one minute to complete the recirculation removal procedures for a time step = 0.1xTR. It is evident that the computation time will increase when a smaller time step is used. As shown in Figure , a marked increase in the computation time is observed for time steps < 0.1xTR. However, despite the substantial increase in computation time for time steps < 0.1xTR, the RMS remains small and stable. Conversely, a noticeable increase of RMS is observed for time steps > 0.1xTR. Therefore, a time step of 0.1xTR was used for all of the patient studies which represent the best tradeoff between the fitting accuracy and computation time.

With the proposed hybrid approach – ICA for regions with a prolonged TTP and MFF for the remaining brain tissues, the total computation time for recirculation removal is < 3min, well applicable even for acute stroke patient studies. Although the TTP values were employed as a means to decide either MFF or ICA for recirculation removal, other parameters such as the arrival time of the contrast agent or the mean transit time should be equally effective. In particular, a rather conservative TTP threshold value (mean + SD of the putative normal hemisphere) was chosen to separate

the TTP lesion from the putative normal brain tissues. Therefore, although was not investigated, we do not foresee that different methods for defining abnormal regions will affect the overall results.

In summary, we have demonstrated the importance of minimizing the effects of recirculation in predicting tissue outcome using CBF in ischemic stroke patients. The newly developed approach, MFF+ICA, significantly improves the capability of predicting the final infarction. Since the overall process time for the newly developed approach only takes about 2.5mins, this application is readily applicable in a routine clinical set up.

3. Robust Hemodynamic Segmentation in DSC-PWI

As mentioned in the previous chapter, the extent to which cerebral blood flow (CBF) is reduced in relationship to the normal CBF values has been utilized as an indicator to discern ischemic injury. However, despite the well known difference in CBF between gray and white matter, relatively little attention has been given as to how CBF may be differently altered in gray and white matter during ischemia. The lack of attention is most likely attributed by the inability to accurately separate gray and white matter particularly during the hyperacute phase. To this end, it is critical to accurate segment DSC-MR images into different tissue types, especially gray matter (GM), white matter (WM) and cerebrospinal fluid (CSF), based on similar bolus transit profiles prior to the analysis of cerebral perfusion and the evaluation of cerebrovascular diseases, particularly during the hyperacute phase. In this chapter, we propose a robust clustering method for automatic classification of perfusion compartments.

3.1 Introduction

Although MR images including perfusion data have two distinct features: *a small number of classes (tissues)* and *high contrast between different tissues* [85, 86], MR images are always corrupted by many factors, such as electronic noise, field inhomogeneity and partial volume effect. In the context of perfusion-weighted images, in addition to the

poor spatial resolution, the expected signal changes in regions of ischemia after the injection of a contrast agent are likely to be minimal. As a result, automated segmentation of gray and white matter of perfusion-weighted images has been challenging. In this chapter, a robust cluster algorithm is proposed for segmenting GM and WM in both normal and abnormal areas on the basis of the differences in their temporal dynamics in perfusion weighted images.

A few methods have been proposed for brain perfusion segmentation. One of the commonly used approaches for classifying signal-vs.-time curves of perfusion data is based on the similarity mapping [87, 88]. One or multiple pixels of the tissue of interest are manually selected first, and the reference signal refers to as the averaged temporal profile [87] or modeled by autoregressive moving average (ARMA) modeling method [88]. A similarity map is then estimated by a measure of distance between perfusion curves and the reference signal. Pixels with higher values on such a map reflect high temporal correlations with the reference function. Finally, image segmentation for the specific tissue of interest is accomplished by thresholding from the histogram of the similarity map. Although this approach is easy to implement, it has two limitations. First, the user input is mandatory to obtain the representative of the tissue of interest, inducing potential biases. Second, only a single tissue pattern can be extracted for each

similarity map and multiple similarity maps are required for multiple tissue segmentation. Together, this technique may be subjective and cumbersome.

Martel et al., applied a factor analysis of dynamic studies (FADS). This approach is based on the principle component analysis (PCA) to segment the arterial and venous structures [89]. Their results, however, revealed that only the first two factor images are dominated by arterial and venous structures, while the other factors cannot be consistently identified.

Kao et al., proposed to combine independent component analysis (ICA), thresholding, and Bayesian estimation (ICA-TBE) techniques to segment perfusion images into five major tissue types: choroids plexus, artery, vein and sinus (VS), GM, and WM [90]. Unfortunately, even in normal subjects, two or three tissue types tended to mix together in one independent-component image, and the final segmentation result showed the overestimates of artery and venous areas.

Recently, Wu et al., utilized the expectation-maximization (EM) algorithm with a finite mixture of multivariate Gaussians (MoMG) for classification of spatiotemporal hemodynamics[91]. The principal components analysis (PCA) was used to reduce the data dimension and therefore facilitated the subsequent EM estimation. The robustness, accuracy, and sensitivity of this method was assessed using the Monte Carlo simulations. The results suggested that the EM-MoMG performed well when tissue

types were less than nine and signal to noise ratio (SNR) was higher than 40. In addition, convincing results were provided in normal volunteers. However, it had difficulties to segment brain perfusion correctly in the presence of ischemic lesion. One of the plausible explanations for the lack of success in stroke patients may be that the classical PCA and Gaussian mixture models are unreliable if outliers (ischemic stroke areas) exist. To this end, we propose a robust clustering method to differentiate not only major tissue types but also pathological and non-pathological areas in DSC-MRI. Because the dimension of perfusion images is usually much larger than the number of preferred tissue types, a robust PCA, combining both projection pursuit technique and robust covariance estimation, is applied to not only reduce the data dimension but also facilitate the detection of the outliers or abnormalities before classification [96-101]. Subsequently, a mixture of multivariate T distribution is employed for tissue classification. The number of tissue classes is determined by minimizing the information criterion of the minimum description length (MDL) [102], reflecting a tradeoff between the goodness-of-fit and the complexity of the model. The model parameters are estimated using the EM algorithm to maximize the posterior probabilities. The T distribution is often used as an alternative to the normal distribution for experimental results which typically exhibit heavier tails than the normal distribution and provide a parametric approach to robust statistics [54, 103, 104]. Once

all of the tissues of interest are labeled, instead of visually examining the segmented images so as to determine the corresponding tissue types (CSF, normal/abnormal GM or WM), the temporal characteristics of the corresponding concentration curves of each class are utilized to delineate different tissue types. The proposed approach was applied to DSC-MRI perfusion data of ischemic stroke patients at the hyperacute phase.

3.2 Robust Approach for Hemodynamic Segmentation

3.2.1 Preprocessing

In order to minimize any confounds from the background noise, the brain regions were first isolated from the noisy background as well as the areas associated with the skull, scalp, and eyeballs by the following three steps. First, we averaged the first 5 images before the injection of a contrast agent serving as the baseline image. A threshold was set as the full-width-tenth-maximum of the signal intensity of the baseline image. Pixels with signal intensity less than this threshold value were assigned to zero while the remaining pixels were assigned to 1. Second, an erosion operation [105, 106] with a 3×3 structuring element was applied to the resultant binary mask in order to remove all the pixels related to the skull and scalp as well as to separate the eyeball areas from the brain using an image labeling approach [107]. The isolated pixels were then set to zero. Third, a flood-fill operation [108] was used to fill holes in the brain

region. In so doing, a brain mask can be effectively extracted and only the pixels in the brain region were subjected to subsequent processes.

3.2.2 Robust Principal Component Analysis (ROBPCA)

Principal component analysis (PCA) performs an orthogonal linear transformation that maps the data to a new coordinate system spanned by the eigenvectors of the covariance matrix. Therefore, the projection on the first coordinate shows the greatest variance, the second coordinate shows the second greatest variance, and so on [109, 110]. PCA can be used for data reduction by projecting the data onto only selected subsets of the first few principal coordinates while retaining the characteristics of the data set that contributes to most of its variance. Since PCA is primary for dimension reduction, it is often the first step for the analysis of high-dimensional data, followed by the discriminant analysis, cluster analysis, or other multivariate techniques. However, classical PCA is based on the eigenvectors of the empirical covariance matrix which is highly sensitive to anomalous observations. As a result, the principal components are often attracted towards outliers and cannot correctly capture the variation of the regular observations.

Instead of using classic PAC, we propose to employ the robust PCA methods, which are much less sensitive to outliers, obtaining reliable principal components and reducing data dimensions. In particular, we have implemented the ROBPCA approach,

describing in details by Hubert et al. [101]. The ROBPCA combines the `projection pursuit' methods to initially reduce data dimensions and the `robust scatter matrix estimation' to obtain robust principal components from the lower-dimensional subspace. The Matlab (The MathWorks, Natick, MA, UCA) program *robpca* and auxiliary functions provided in LIBRA: A Matlab Library for Robust Analysis by Verboven and Hubert. LIBRA is available at the website: http://wis.kuleuven.be/stat/robust/LIBRA.html.

Assuming the MR perfusion data for each subject can be written as an $m \times N$ matrix, where N is the number of pixels in the extracted brain mask, and m is the number of temporal observations. In the context of our study, m was typical equal to 40, corresponding 40 time point images. The ROBPCA approach was employed to reduce the perfusion data to a $10 \times N$ matrix. The *10* principal components were chosen since the number of desired tissue types is less than *10* and the sum of the first *10* eigenvalues retains over 90% of the data variance. The dimension reduction from *40* to *10* dramatically reduces the model complexity in fitting the mixture of T distributions. Moreover, ROBPCA is not only capable of generating more reliable principal components in contaminated datasets (containing outliers), but also allowing the detection of these outlying observations [99-101]. Figure 3 compares the score plots for the first two principal components using classical PCA and ROBPCA, respectively.

Different tissue types are segmented using the proposed approach and are represented with different colors. It is evident that the ROBPCA yields more robust estimates than that using the conventional approach when the abnormal areas behave like outliers. Different tissue types in Figure 3(b) using robust principal components are more clustered together and should be better separated than those in Figure 3(a).

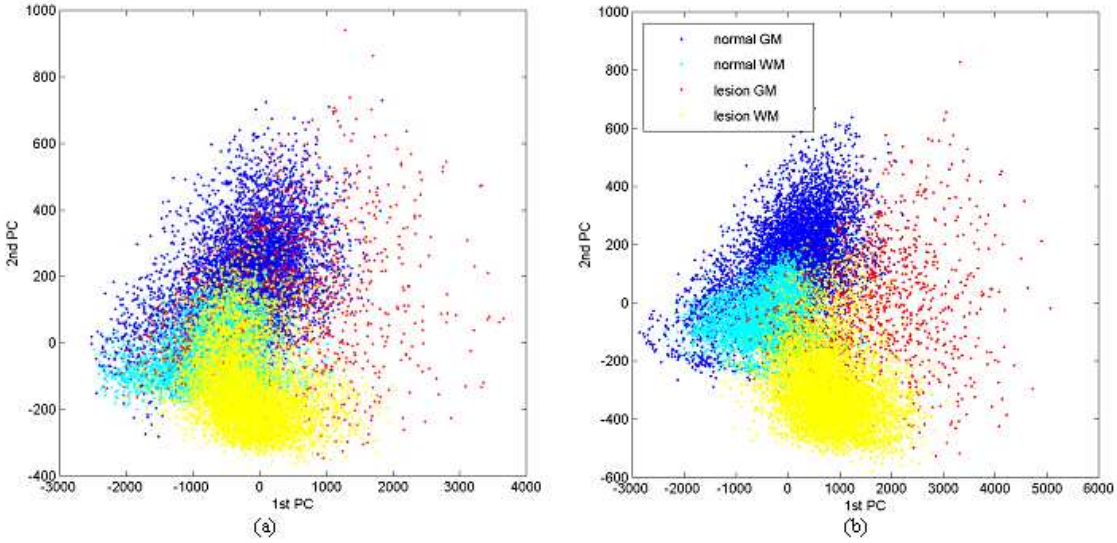

Figure 32. The score plots for 1st and 2nd principal components of perfusion dataset using (a) classical PCA, and (b) robust PCA

3.2.3 Tissue Segmentation with the mixture model of multivariate T distributions

The tissue segmentation was carried out using unsupervised Bayes classifier with a mixture model of multivariate T distribution

$$f_t\left(\mathbf{x}_n;\mu,\Sigma,\upsilon\right)=\frac{\Gamma\left(\frac{\upsilon+p}{2}\right)|\Sigma|^{-1/2}}{(\pi\upsilon)^{\frac{p}{2}}\Gamma\left(\frac{\upsilon}{2}\right)\left(1+\frac{\delta}{\upsilon}\right)^{\frac{\upsilon+p}{2}}} \tag{3.1}$$

where $\delta=(\mathbf{x}-\mu)^T\Sigma^{-1}(\mathbf{x}-\mu)$ (see Appendix A for more descriptions) and υ is the degree of freedom which parameterizes the 'robustness' of the distribution, i.e. how wide the tails are. These model parameters were calculated using the EM algorithm. The EM algorithm consists of two alternating iterative steps: the E-step and M-step (refer to Appendix B for details). In E step, the membership z_{ij} and weight u_{ij} of each data point y_i with respect to the jth component were updated using the conditional expectation based on the model parameters estimated in the previous $(k-1)$th iteration. The M-step was used to estimate the model parameters: proportions π, component means μ and covariance Σ using:

$$\hat{\pi}_j^{(k)}=\frac{\sum_{i=1}^{n}\hat{z}_{ij}^{(k)}}{n} \tag{3.2}$$

$$\hat{\mu}_j^{(k)}=\frac{\sum_{i=1}^{n}\hat{z}_{ij}^{(k)}\hat{u}_{ij}^{(k)}y_i}{\sum_{i=1}^{n}\hat{z}_{ij}^{(k)}\hat{u}_{ij}^{(k)}} \tag{3.3}$$

$$\hat{\Sigma}_j^{(k)} = \frac{\sum_{i=1}^{n} \hat{z}_{ij}^{(k)} \hat{u}_{ij}^{(k)} \left(y_i - \hat{\mu}_j^{(k-1)} \right) \left(y_i - \hat{\mu}_j^{(k-1)} \right)^T}{\sum_{i=1}^{n} \hat{z}_{ij}^{(k)} \hat{u}_{ij}^{(k)}} \tag{3.4}$$

The estimates of these three groups of parameters are rather straightforward since all of them are in a close mathematical form. However, the estimation of the degree-of-freedom, υ, which adjusts the tail shape of the T distribution, is a solution of the following implicit nonlinear equation

$$\left\{ -\psi\left(\frac{\upsilon_j}{2}\right) + \log\left(\frac{\upsilon_j}{2}\right) + 1 + \frac{\sum_{i=1}^{n} \hat{z}_{ij}^{(k)} \left(\log \hat{u}_{ij}^{(k)} - \hat{u}_{ij}^{(k)} \right)}{\sum_{i=1}^{n} \hat{z}_{ij}^{(k)}} + \psi\left(\frac{\upsilon_j^{(k)} + p}{2}\right) - \log\left(\frac{\upsilon_j^{(k)} + p}{2}\right) \right\} = 0 \tag{3.5}$$

Solving this nonlinear equation for all tissue types in each iteration typically involved a one-dimensional search, resulting in a significant computation overhead to the EM algorithm. Moreover, practical problems for solving a nonlinear equation include not only computation but also convergence. Lange et al. [111] and de Ridder [112] suggested to fix ν prior to EM. In the context of our work, multivariate T

distribution was used to replace the multivariate Gaussians due to its tunable tails by varying ν. Therefore, using a predefined ν may lose the advantages of using the multivariate T distribution. Shoham et al. [113] proposed an empirical approximation to provide a fast approximation to the solution ($|\upsilon-\upsilon^*|<.03$, evaluated using simulated data with $5<\upsilon<50$):

$$\upsilon^* = \frac{2}{y+\log y-1} + 0.0416\left(1+erf\left(0.6594\times\log\left(\frac{2.1971}{y+\log y-1}\right)\right)\right) \tag{3.6}$$

where y is an auxiliary variable as

$$y = -\sum_{i=1}^{n}\sum_{j=1}^{g}\hat{z}_{ij}\left[\psi\left(\frac{\upsilon+p}{2}\right)-\log\left(\frac{\upsilon+\delta}{2}\right)-\hat{u}_{ij}\right]/N \tag{3.7}$$

However, the accuracy of this empirical approximation was substantially compromised when experimental data such as MR perfusion-weighted images, was employed. In addition, the utilization of an empirically determined parameter weakens the advantage of using the superior statistical model. In this work, we propose the following strategy to solve this nonlinear equation rapidly and effectively. First, instead of solving a nonlinear function $f(\upsilon) = -\psi\left(\frac{\upsilon}{2}\right)+\log\left(\frac{\upsilon}{2}\right)=c$, where c is a constant combining all of the items which are not related to the variate υ in Equation B8, we tried to solve a more

linear function $f(\tau) = -\psi\left(\exp(\tau)\right) + \tau = c$ by setting $\upsilon = 2\exp(\tau)$. Second, rather than randomly selecting an initial value, we set up a τ -f(τ) table beforehand, where τ were integers from 2 to 500, and the initial value was searched in the table in order to make f(τ) closest to the constant c. The first two steps also helped not to converge to local minimums. Lastly, a least squares search with the carefully selected initial value was used to estimate τ and thus υ.

So far, we have discussed in details regarding tissue classification of perfusion data using the EM estimation with finite mixture of multivariate T distributions. The number of tissue classes g needs to be determined. To this end, we seek an optimal g by minimizing the information criterion of the minimum description length (MDL) [102]:

$$MDL(g) = -\log\left\{\prod_{i=1}^{N}\sum_{j=1}^{g}\hat{\pi}_j P(y_i;\hat{\mu}_j,\hat{\Sigma}_j,\hat{\upsilon}_j)\right\} + J\log(N)$$

where $J=g(t^2+3t+4)/2-1$ (Equation B1). The first item is the log-likelihood of the perfusion dataset with the estimated parameters by the EM algorithm and represents the goodness-of-fit of the model. The second term is the logarithm of the total parameters and denotes the model complexity. Therefore, the optimal number is a balance of these two terms so that the mixed model can accurately describe the data while keeping it as simple as possible.

3.2.4 Procedures

Preprocessing and dimension reduction: Separate the brain from background noise by removing the areas associated with the skull, scalp and eyeballs. Transform all the perfusion data (40×N) to a small subpace (10×N) via ROBPCA.

Initialization: A k-means clustering approach was used to roughly segment the whole ROBPCA subspace into N classes (N=5 in this work). Model parameters were estimated based on the k-means cluster results.

E Step: Update memberships z_{ij} and weights u_{ij} (Equation B3 and B4).

M Step: Update model parameters (Equation B5, B6 and B7).

Repeat E and M steps until convergence: Calculate the complete likelihood L according to Equation B2. Repeat E and M steps until $(L(k+1)-L(k))/L(k)<0.001$.

Clustering: Implement E step one more time to obtain membership information.

3.2.5 Automatically identify the segmented tissue types

The temporal characteristics of the passage of the contrast agent could differ among different tissue types. First, the bolus of contrast agent typically arrives first in the GM and then in the WM. Second, hypoperfusion will result in broadening of the concentration curves, i.e. the full-width-half maximum (FWHM) is wider than those in the normal tissues. Finally, there is minimal contrast agent in CSF, particularly during the first passage. According to these pieces of information, an automatic procedure was

designed to identify different tissue types instead of visually examining the segmentation results and manually assigning tissue categories based on anatomical locations. The flowchart for the identification is shown as follows. The thresholds were set based on the patent subjects that we had. Due to the limited samples (N=10), we are unable to evaluate if these thresholds are optimal or not.

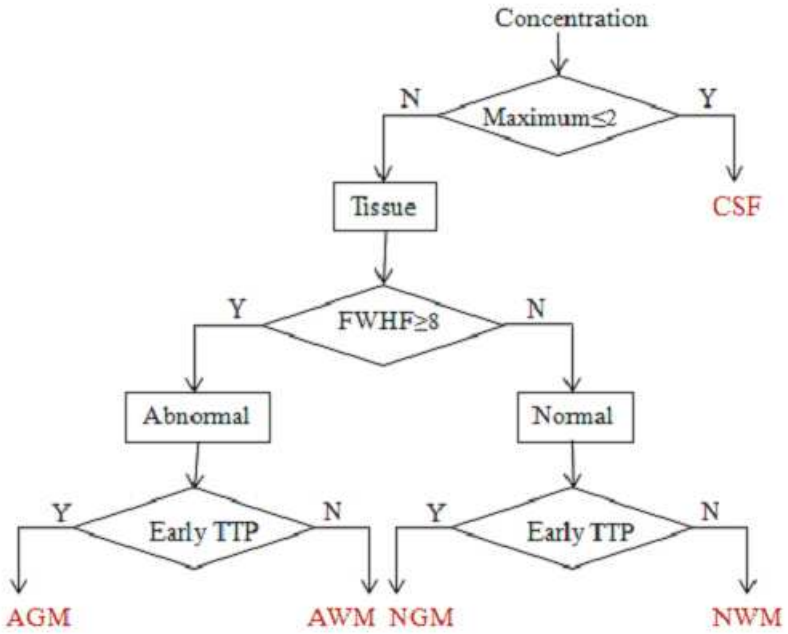

Flowchart for the tissue-type identification.

3.3 Monte Carlo Simulation Study

Monte Carlo simulations were employed to access the performance of the estimation of the cluster number with MDL and to compare the accuracy of the proposed approach with several conventional methods. We simulated perfusion data of

multiple tissue types based on the region of interest (ROI) chosen in one patient so as to emulate those in the real applications. The selected ROIs represent normal GM (NGM), normal WM (NWM), abnormal GM (AGM), abnormal WM (AWM), and cerebrospinal fluid (CSF). Each ROI consists of 500 pixels. The statistics for each tissue type, such as mean signal-vs.-time curve (40×1 vector) and covariance matrices of signal intensities across time (40×40 matrix), were estimated as the hypothetical parameters to create a set of noise-free simulated dynamic images. Matlab functions: *mvnrnd* and *mvtrnd* were used to simulate multivariate normal distribution and multivariate T distribution, respectively.

To evaluate the effects of adding noise and outlier profiles in perfusion data, four groups of simulations with different classification purposes were created: no outliers and moderate noise (SNR=40), no outliers and high noise (SNR=10), outliers and moderate noise, and outliers and high noise. In the cases of no outliers, only three tissue types (NGM, NWM and CSF) were considered and the total numbers of simulated pixel were 1000, 1000 and 500 for NGM, NWM and CSF, respectively. In the cases with outliers, all five tissue types were considered and there were 500 simulated pixels for each of them. Therefore, no matter if outliers were present or not, there were total 2,500 pixels for each run. Monte Carlo simulations were repeated 1000 times in each setting.

Accordingly, the total number of simulated time-series data was 2,500×2 (SNR=10 or 40) × 2 (with or without outliers) × 1000 (runs).

The number of tissue types was estimated in such a way that minimized the information criterion of MDL. In addition to the proposed robust cluster approach, we also applied classical PCA to condense the 40×N (N=2,500 in the simulation) matrix to a 10×N matrix and finite mixture of multivariate Gaussian distributions to classify the simulated perfusion data [91]. The accuracy of the classification for each run of simulation was defined as the proportion of agreement, i.e., the total number of agreements for all of the tissue types vs. the total number of pixels (2,500). The accuracy of the proposed approach was compared with that using the conventional method.

Figure 4 shows the MDL at different cluster numbers and the optimal number is the value that minimizes the MDL from a simulated dataset. The horizontal axis is the number of tissue classes and the vertical axis is the normalized MDL. Both the conventional and robust methods correctly determine the tissue numbers in both moderate and high noise scenarios (Figure 4(a) and (b)). With five-tissue-type simulation, the optimal number of the information criteria of MDL tends to underestimate the correct cluster number using the conventional clustering technique (Figure 4(c)). In contrast, with the proposed approach, the number of classes is

accurately determined for moderate noise situation, but is inaccurately overestimated as 6 when the SNR is decreased to 10 (Figure 4(d)).

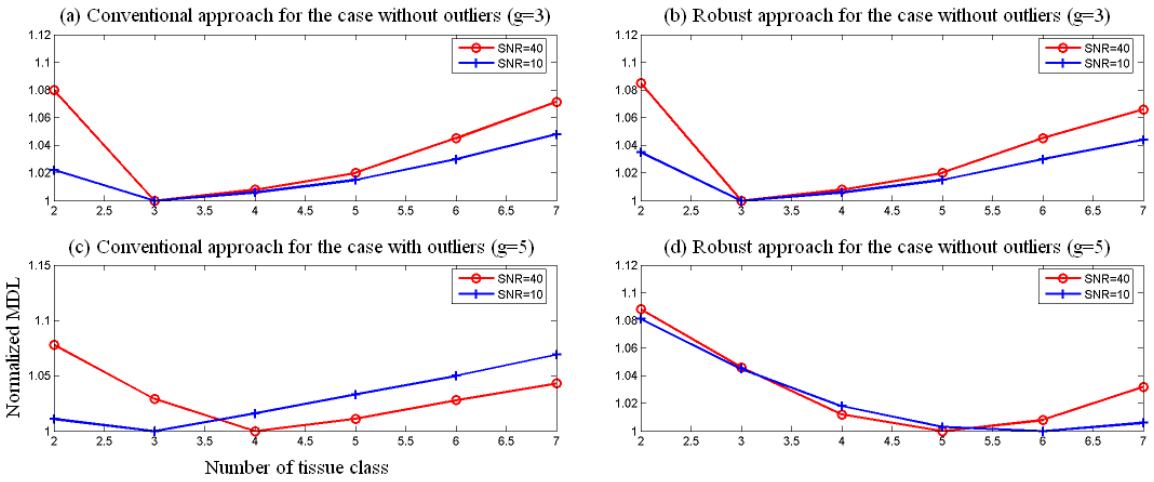

Figure 43. Simulation results for the estimation of optimal number of tissue classes in the sense of minimizing the information criterion of the MDL.

Table 6 shows that averaged accuracy ± standard deviation (SD) for three tissue type and five tissue type simulations with the moderate and high noise levels using both the conventional and robust approaches. In the three-tissue-types case, there are no significant differences between the conventional method and robust technique in both moderate and high noise conditions. But for the case with five-tissue-types, the robust technique shows a significant improvement in the presence of moderate or high noise when comparing with the conventional method.

Table 6. Averaged accuracy for Monte Carlo Simulations (*: p<0.05, **: p<0.001)

	Cases without outliers (g=3)		Cases with outliers (g=5)	
	Moderate noise (SNR=40)	High noise (SNR=10)	Moderate noise (SNR=40) *	High noise (SNR=10) **
Conventional Approach	95.8±0.77%	89.1±1.44%	80.2±7.03%	62.4±12.89%
Robust Approach	95.3±0.74%	88.6±1.51%	92.8±1.13%	78.7±7.35%

3.4 Acute Stroke Patient Study

Perfusion images from ten acute ischemic stroke patients were analyzed. Figure 5 illustrates the segmentation results for one subject. Figure 5(a) shows the color-coded composite images, where each color represents one tissue type. The segmentation of the T_1-weighted images is displayed at Figure 5(b). It has been well known that T_1-weighted images are not sensitive to detect brain tissue abnormalities during the acute stoke stage. Therefore, the T_1 segmentation can only separate the major tissue types, but cannot differentiate the pathological area from the non-pathological brain region. Comparing (a) with (b), the GM/WM/CSF perfusion segmentation compares favorably with the T_1 segmentation. Figure 5(c) shows the one-month follow-up T_2-weighted images. The pixels with higher values in T_2-weighted images (red and bright yellow) represent the

final infracted tissues. Comparing between (a) with (c), it shows that the proposed method could effectively distinguish pathological tissues from normal brain.

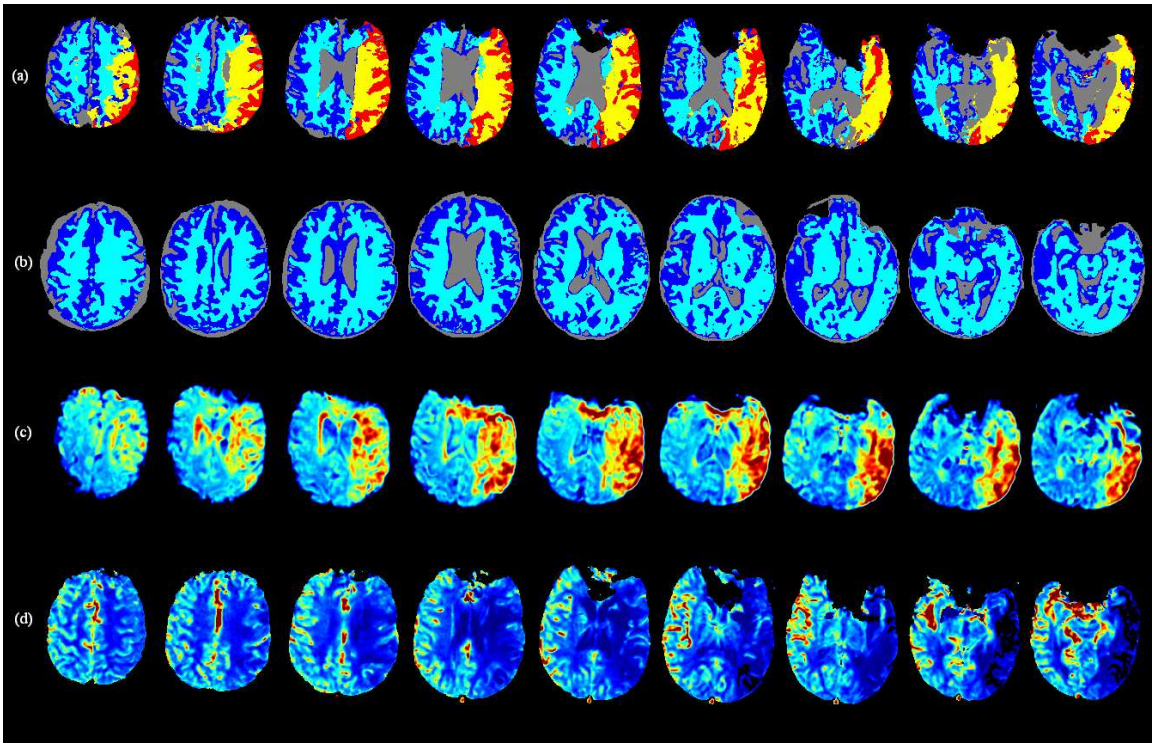

Figure 54. Perfusion segmentation results for one acute stroke patient. (a) The five-tissue-types segmentation for perfusion images within three hours from onset: NGM (blue), NWM (cyan), AGM (red), AWM (yellow), and CSF (gray). (b) The three-tissue-types segmentation in T1-weighted images within three hours from onset: GM (blue), WM (cyan) and CSF (gray). (c) The one-month follow-up T2-weighted images. (d) One perfusion parametric map: rCBF.

Figure 5(d) shows the rCBF maps. Mean CBF values were obtained from normal/abnormal GM and WM, separately using the segmentation results shown in

Figure 5(a). The ratio of normal GM/WM is 2.06±0.29, consistent with the reported results in the literature [28,31,32] while this ratio is reduced to 1.58±0.18 for abnormal GM/WM, suggesting that ischemia leads to preferential reduction of CBF in GM.

Finally, the signal-vs.-time MR signals and the relative concentration courses for each clustering type are shown in Fig. 15. Figure 6(a) and (b) illustrate the averaged signal-vs.-time curves and relative concentration time curves of different tissue classes, respectively. It is evident that the contrast agent arrives earlier and washes out faster in gray matter and normal hemisphere when compared to that for white matter and abnormal hemisphere, respectively. In CSF, there are minimal signal changes, consistent with our expectation.

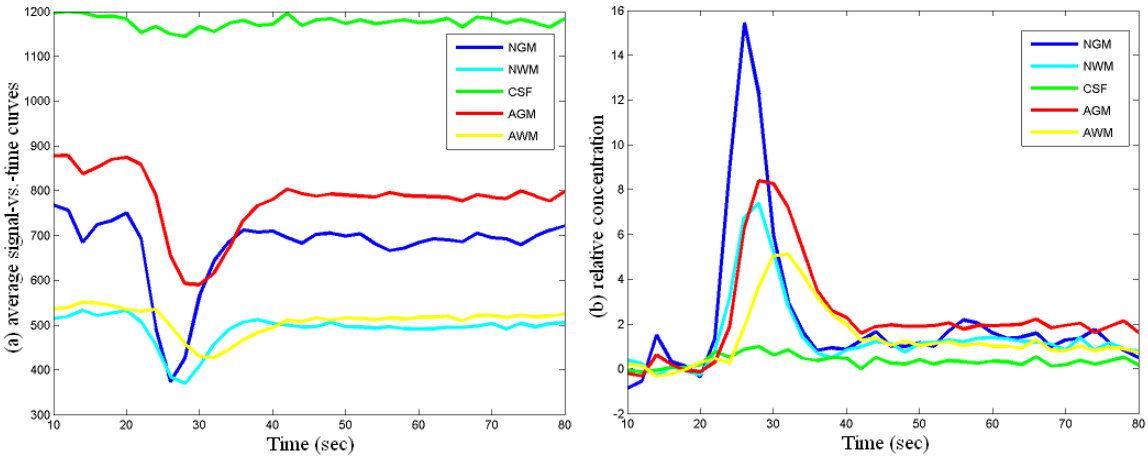

Figure 65. The average signal-vs.-time curves and and relative concentration time curves for different tissue types.

3.5 Discussion

In this chapter, a robust clustering method for high-dimensional image segmentation has been presented based on ROBPCA subspaces and the mixtures of T distribution. In the presence of outliers, ROBPCA yields more robust estimates than the conventional PCA methods. The ability to delineate normal and abnormal tissues also provides a diagnostic tool. The mixture of multivariate T distribution is used to replace the Gaussian mixture models to fit a set of multivariate experimental data which may exhibit heavy tails or atypical observations, such as perfusion images for acute stroke patients. The T distribution has a wider tail than the Gaussians and, moreover, has a robustness tuning parameter, the degree of freedom v, making the tail adjustable. We present a framework for fitting mixtures of multivariate T distribution using the EM algorithm on the basis of maximum likelihood estimation when clustering information is missing. The EM algorithm is useful for both parameter estimation of mixture components and for coping with the label information indicating the component membership. Thus, the proposed robust finite mixture model unites the advantages of both parametric and nonparametric approaches: accuracy and flexibility, respectively.

The Monte Carlo simulations of the proposed robust approach demonstrate comparable with results with that using the conventional method in the absence of

outliers. As described in the Appendix A, the multivariate T distribution is a general extension of multivariate Gaussian distribution and in the extreme case $\upsilon \to \infty$, it represents a Gaussian distribution. When no outliers are present, the mixture of multivariate T distribution on ROBPCA subspaces performs similar as the Gaussian distribution on PCA subspaces, but is slightly less suitable for the fitting of simulated multivariate perfusion data. However, in the presence of outliers, i.e. when the abnormal cerebral perfusion exists, it is much more robust to use the proposed approach than the conventional method. This might due to the two improvements provided by the newly developed approach. First, the abnormal brain perfusion is more separable from the normal using the ROBPCA coordinates than that using PCA. Second, the T distribution with an adjustable tail provides a robust alternative to the Gaussian distribution.

Based on our application to differential multiple spatiotemporal hemodynamics for brain perfusion MR images on acute stroke, the proposed method has several advantages. First, different tissue types can be systematically separated and displayed in one image. Second, the transit profiles of contrast agent in these tissues can be well separated and thus provide information to automatically identify different tissue types. Third, our results show that the proposed approach can separate both pathological and non-pathological hemodynamics. Therefore, it provides an effective imaging technique

to improve the diagnosis and to evaluate the treatment effects. Finally, this method can be extended to other imaging modalities, such as dynamic CT and PET, and to other organs, such as the heart, liver or kidneys using perfusion-weighted images.

4. Functional Connectivity Study in Pediatric Subjects

Functional MRI (fMRI) is a task-related study, which utilizes non-invasive MRI to record the change of oxygen consumption resulted from neuronal activity in the brain while subjects performing specific activities or sensing the external sensory/cognitive inputs. Thus, the corporation of the subjects is mandatory, leading to the difficulty of utilizing conventional fMRI to study the brain function in young children and/or special patient populations, such as Alzheimer's disease and schizophrenia. Functional connectivity MRI (fcMRI), in contrast, has been used to obtain blood-oxygen level dependent (BOLD) signals in a task-free or resting state.

In the next two chapters, fcMRI is used to investigate the brain functional development in the first two years of childhood. The brain growth from 2wks, 1 yr, to 2 yrs is remarkable (Figure 7). To the best of our knowledge, this is the first study not only documenting the presence of cortical functional connectivity in very young healthy children, but also demonstrating how cortical functional connectivity increases in the developing brain.

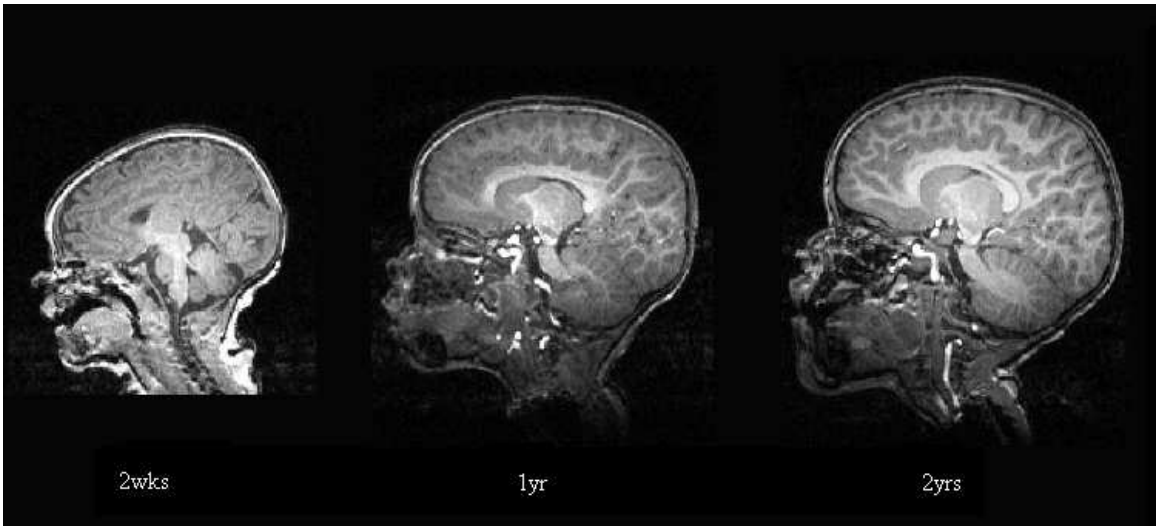

Figure 76. Representative T1-weighted MP-RAGE images are shown for 2wk, 1yr and 2yrs old children.

4.1 Introduction

Biswal et al. first reported the approach of fcMRI [17] in detecting motor-function-related brain regions utilizing the synchronization of low-frequency BOLD signal. Specifically, a time series of T_2^*-weighted images was acquired every 1 or 2 seconds while subjects lie inside an MR scanner in a resting condition. A temporal low pass filter (cutoff frequency ~0.08Hz) was applied pixel-by-pixel to the acquired images. With a reference signal obtained from a region exhibiting brain activation using a finger-tapping fMRI study, temporal correlations were calculated for the entire brain. Their results suggested that regions exhibiting high temporal correlation resembled that obtained with finger-tapping stimulations from the same subjects and that these

observed temporally correlated regions may represent cortical brain functional connectivity. Subsequently, their findings were replicated by many other studies in motor, visual, and auditory cortices by many investigators [17, 18, 37-39]. More importantly, several lines of evidence have recently implicated that fcMRI may reveal a tightly coupled brain neural network, further underscoring the potential utility of fcMRI to shed light on our understanding of brain function.

From the data acquisition aspect, the commonly used imaging sequences for fcMRI are very similar, if not identical, to that of conventional fMRI. However, unlike task-related fMRI where external sensory/cognitive paradigms are required to specifically activate different regions of the brain, fcMRI acquires images during a task-free or resting condition and detects brain regions which are highly temporally correlated. Given the fact that during fcMRI study, subjects are at a resting condition with the absence of complex cognitive demands, this approach could be a powerful tool to delineate brain functional connectivity in young pediatric subjects. To this end, this study focuses on how functional brain connectivity may be present in very young pediatric subjects (0-2 years old) in a sleeping condition. Specifically, this study aims to investigate the following two questions: 1) does cortical functional connectivity exist in healthy pediatric subjects between 0-2yrs old and 2) if so, how does cortical functional connectivity change as a function of age? Our results suggest that functional

connectivity exists as young as two weeks old for both sensorimotor and visual cortices and that functional connectivity is highly age-dependent. Besides these two findings, we also explore the correlation estimation at multiple frequency ranges to characterize the frequency-dependence of functional connectivity at the early age of childhood. Specifically, a highly redundant wavelet analysis approach: maximal overlap discrete wavelet transform (MODWT) is used to separate fcMRI time courses into multiple frequency ranges and their coefficients in time for correlation analysis. Our results reveal that different functional connectivity shows different frequency-dependence.

4.2 Data Acquisition and Preprocessing

4.2.1 Subjects

A total of 52 normal and healthy children were recruited for this study. These children were divided into three sub-groups depending on age: 17 neonates (2-4 weeks), 17 one year old and 18 two years old. Informed consent was obtained from the parents prior to the imaging studies. Since all of the subjects were normal and healthy, no sedation was employed. All of the subjects were imaged during sleep. For the neonate group, a vacuum pillow was used to minimize head motion and hearing protection earplugs were worn for protecting hearing from loud noise. For the one year and two years old groups, only headphone was used.

4.2.2 Imaging Protocols

All images were acquired on a 3T head-only MR scanner (Allegra, Siemens Medical Systems Incs). A 3D MP-RAGE sequence was used to provide anatomical images, co-register among subjects and define the regions of interest (ROIs) to obtain the reference signal for subsequent correlation analysis. The imaging parameters were as follows: repetition time (TR) = 1820ms; echo time (TE) = 4.38 ms; inversion time = 1100ms; slice number = 144; acquisition matrix = 256×256 and voxel size = 1x1x1mm^3. For the fcMRI studies, a T2*-weighted EPI sequence was used to acquired images. The imaging parameters were as follows: TR = 2sec, TE = 32 ms; slice number = 33; acquisition matrix=64×64 and voxel size=4×4×4mm^3 or acquisition matrix = 128×128 and voxel size = 2×2×2mm^3. This sequence was repeated 150 times so as to provide time series images for 5 minutes. The MR images acquired with a matrix size of 128×128 were linearly interpolated into a matrix size of 64×64. The first 10 images of each experiment were discarded, allowing magnetization to reach steady state.

4.2.3 Preprocessing

All fcMRI images were assessed for head movement. In addition, a minimum of three-minutes of fcMRI data series (90 time points) were required for data analysis. Therefore, if serious motion occurred (more than one pixel or >4mm) at the beginning or the end, the time courses were truncated for subsequent data process. Motion artifacts

were observed in eight neonates, six 1yr olds and nine 2yr olds; these subjects were excluded from final data analysis. As a result, nine neonates, eleven 1yr olds and nine 2yr olds were included for the final data analysis.

Moreover, only voxels within the brain area were included in the analysis and the brain region was defined in three steps. First, a brain mask was obtained by setting all pixel values larger than 15% of the maximum intensity to 1 and all values smaller than this threshold to 0. Second, an erosion operation with a 3×3 structure element was applied to the binary brain mask in order to remove all pixels corresponding to skull and scalp areas and to separate brain and the surroundings, such as eyes. Only the brain region is kept and all the others are set to 0. Last, a flood-fill operation was used to fill holes in the brain region.

4.3 Cross-Correlation Analysis (CCA)

To obtain brain functional connectivity maps, all of the acquired images were processed using the procedures outlined in Figure 8. A more detailed description for each step is provided below.

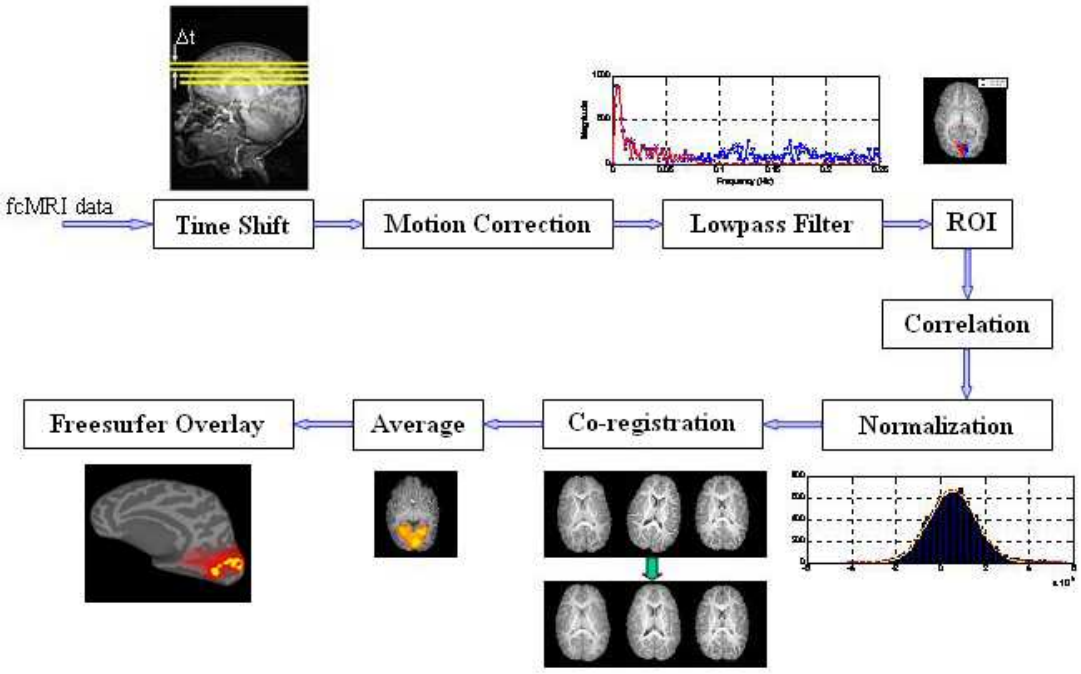

Figure 87. Flowchart for Cross-Correlation Analysis (CCA) in the fcMRI brain development study.

4.3.1 Time Shift Correction

For CCA approach, time synchronization in similar functional areas was used to locate the functional connectivity maps. Since images at different anatomical locations were acquired at a different time, it is imperative to correct for the time differences between different slices. The time difference was corrected through a linear interpolation in the time domain.

4.3.2 Motion Correction

To minimize the potential confounds induced by motion between scans, the Automated Image Registration (AIR) [113, 114] package with 6-parameter rigid-body transformation was used to co-register all time series images to the images of the first scan. The signal intensity as a function of time at multiple randomly selected locations was visually inspected. Experimental data was excluded from the subsequent analysis if we could not identify 90 consecutive motion free time points, and/or severe motion artifacts were identified.

4.3.3 Low-pass Filter

A spatial 3D-Gaussian ($8\times8\times8 mm^3$ and $\sigma=2mm$) filter was applied to the images in order to improve SNR. Subsequently, Fourier transform was used to convert the signal-vs-time of each pixel to the frequency domain, and a low-pass filter with a cutoff frequency of $0.08Hz$ was applied. The filtered signal was then inverse Fourier transformed back to the time domain.

4.3.4 ROI Selection

In order to ensure the consistency of defining ROIs for obtaining the reference function for the subsequent correlation analysis, the fcMRI images were co-registered to the MP-RAGE images using the AIR for each subject [113, 114]. Subsequently, a board

certified neuroradiologist manually drew three ROIs in each hemisphere for a total of 6 ROIs using the two MP-RAGE images, one at the sensorimotor and the other at the visual area, for each subject. Representative examples of the anatomical locations of these ROIs are shown in Figure 9(a) and (b) for the sensorimotor and visual areas, respectively. These manually selected regions were subsequently mapped onto the co-registered T_2*-weighted EPI images to obtain averaged MR signal intensity. Although both the primary motor and sensory cortices were separately identified, the limited spatial resolution leading to potentially partial volume effects in the T_2*-weighted EPI images presented a challenge to separately analyze motor and sensory signal. Therefore, signal intensities from voxels identified as the primary motor and sensory cortices were averaged to derive a single reference function to delineate motor-sensory function.

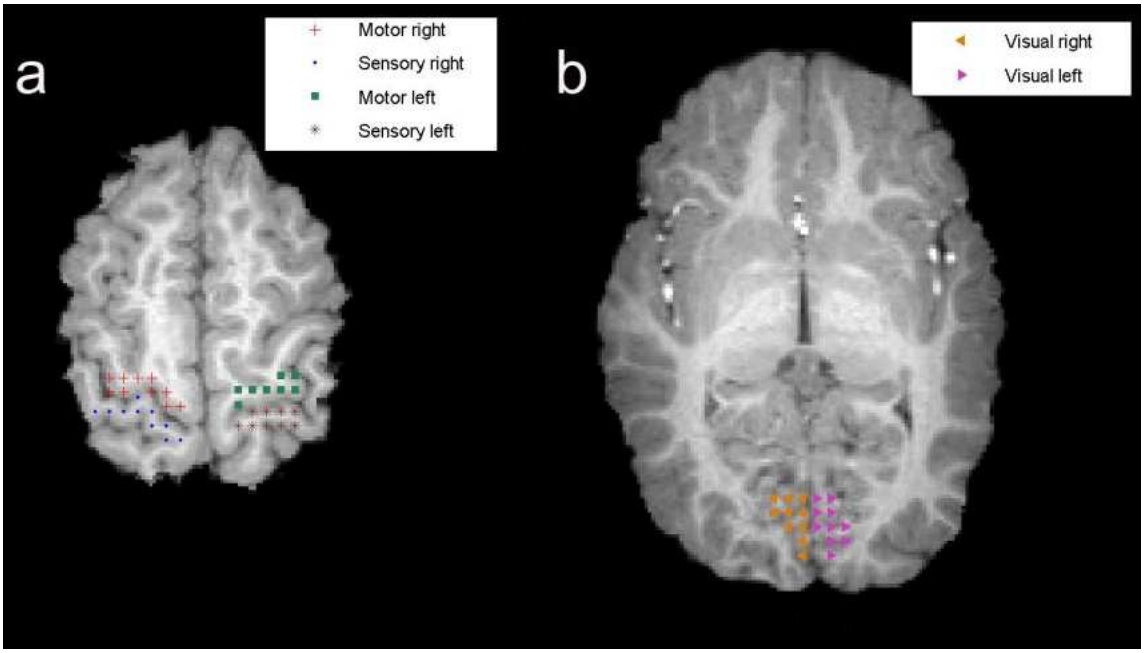

Figure 98. Representative examples of the anatomical locations of the selected ROIs for the sensorimotor (a) and visual areas (b), respectively.

4.3.5 Correlation Analysis

A total of four reference functions, right and left sensorimotor and right and left visual cortices, were used for temporal correlation analysis, respectively. Temporal correlation was conducted pixel-by-pixel and correlation coefficient (cc) maps were obtained.

4.3.6 Correlation Normalization

It has been suggested by Lowe et al [18] that the distributions of in vivo correlation coefficients may not be the same between individuals, across trials in the

same subject, or even across voxels within one experiment. Therefore, it is imperative to normalize the effects of the intrinsic correlations prior to conducting group analysis. To this end, correlation coefficients were converted to t-values according to

$$t=\frac{cc}{\sqrt{cc^2+v^2}} \tag{4.1}$$

where v is the number of the acquired time points and represents the degrees of freedom [18]. The calculated t was then converted to a Z-statistic according to

$$z=\frac{t-\bar{t}}{\sigma} \tag{4.2}$$

where $\bar{t}$ and σ were expected value and standard deviation of the Gaussian fit to the full-width at half-maximum (FWHM) of the t distribution.

4.3.7 Group Analysis

The MP-RAGE images from one of the subjects in each age group were randomly chosen as the template and MP-RAGE images from the remaining subjects were co-registered onto the template using the FMRIB's Linear Image Registration Tool (FLIRT). The group average z-score maps were obtained after registration.

4.3.8 Visualization

Finally, in order to better visualize regions exhibiting the putative brain functional connectivity, Freesufer was employed to generate the brain surface maps

where regions with a z-score > 1 were superimposed. FreeSurfer is an MRI brain imaging software package, developed by Athinoula A. Martinos Center for Biomedical Imaging at Massachusetts General Hospital. By visually examining the FreeSurfer output: 3D brain surfaces with the activation overlays on top for all three age groups, we can easily assess the development of brain functional connectivity for normal and healthy children from 0 to 2 years old.

Cortical functional connectivity in the sensorimotor areas for all three age groups is shown in Figure . Consistent with the adult results reported in the literature, regions showing high temporal correlation are located in the primary sensorimotor areas for all three groups. In addition, both the area and the strength (z scores) increase as a function of age. Similar findings are also observed in the visual area (Figure 10) for the three age groups.

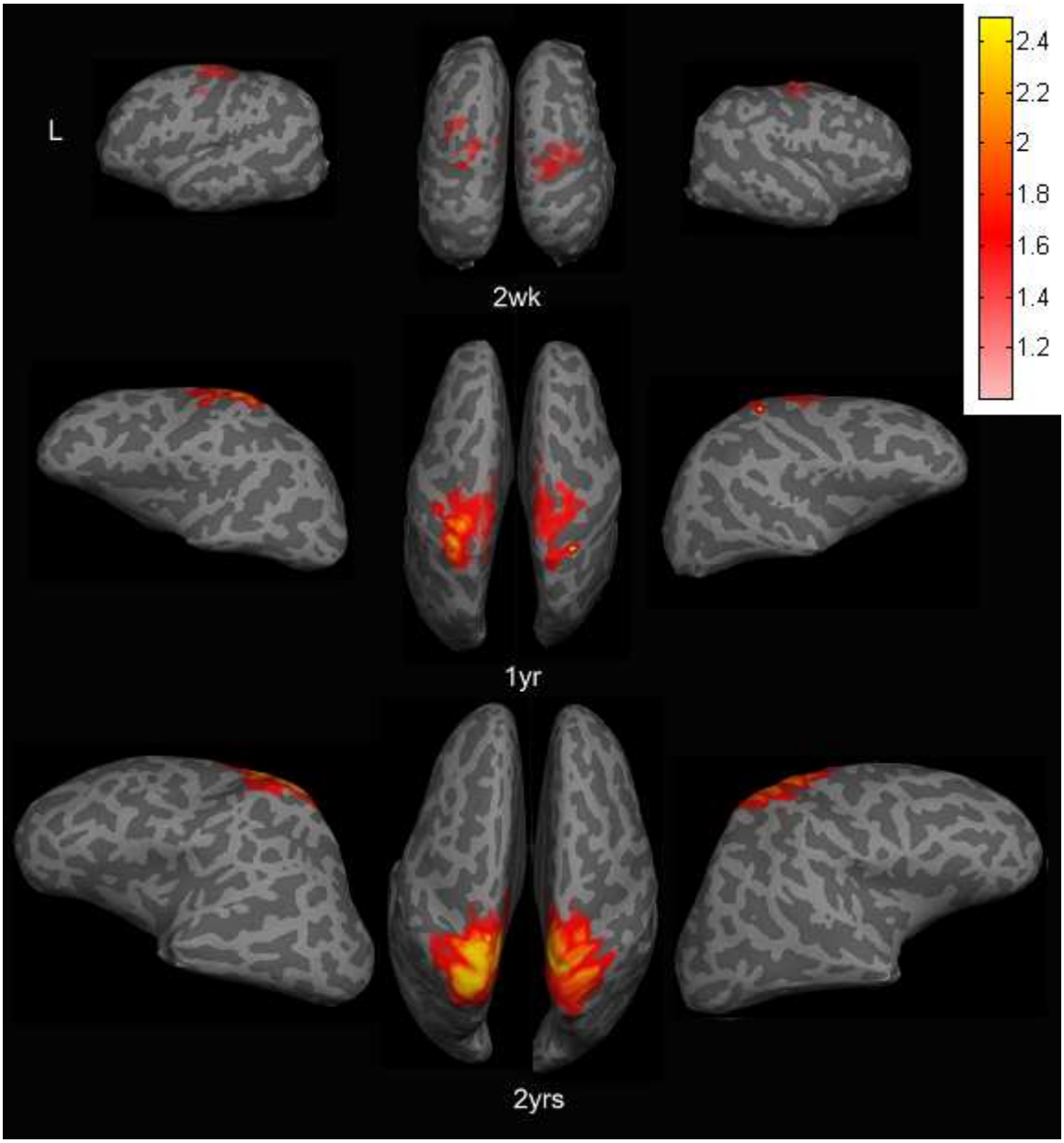

Figure 19. Functional connectivity map in the sensorimotor areas using CCA apparoach for all three age groups.

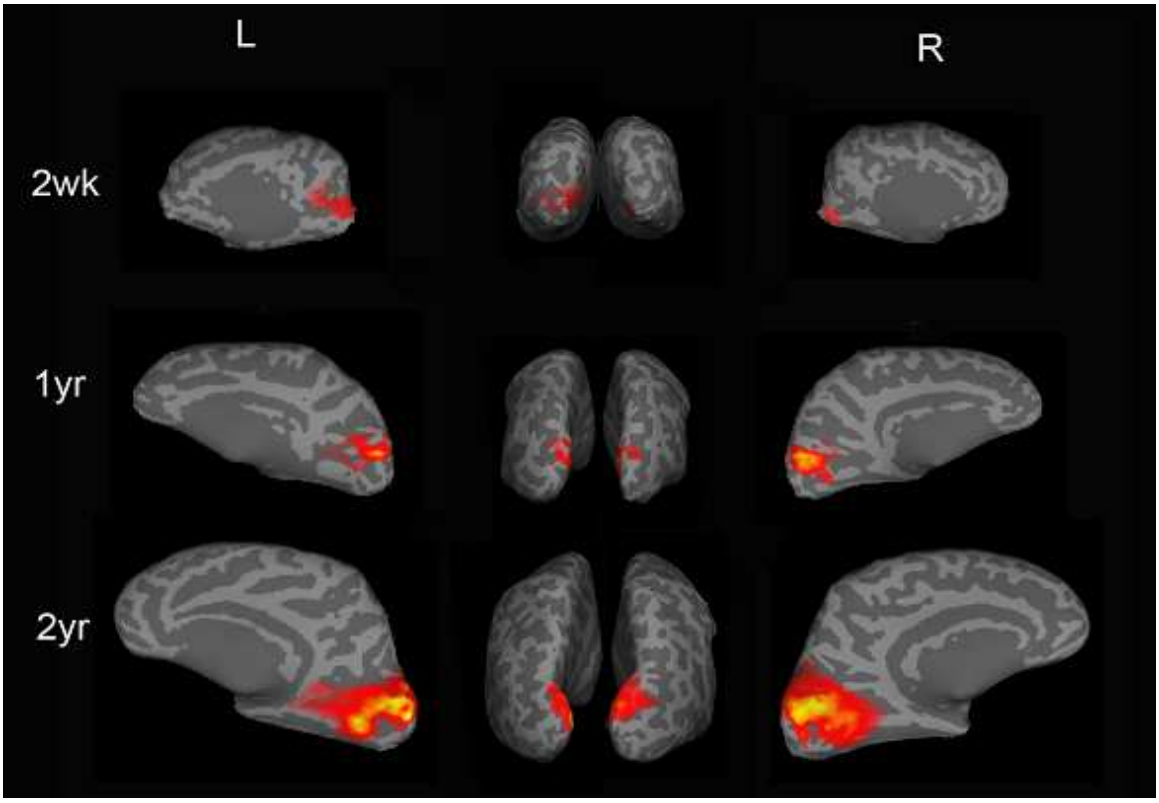

Figure 100. Functional connectivity map in the visual areas using CCA apparoach for all three age groups.

4.3.9 Quantitative Comparison

To quantitatively compare the extent of brain functional connectivity as a function of age, several different parameters were calculated. First, the brain volume exhibiting a z-score greater than 1 was divided by the total intracranial brain volume for each subject, accounting for the differences in head size across different ages. Second, the maximum and minimum percent signal changes in each subject were separately identified for visual and sensorimotor areas. The differences between the two values

were then calculated. The z-score values of each subject in the sensorimotor and visual areas were recorded for each subject. Finally, a normalized histogram analysis was also conducted in regions exhibiting functional connectivity for each age group.

For the group comparison, one-way analysis of variance (ANOVA) with Tukey's multiple comparison was employed. In contrast, a two-tailed paired t-test was employed for comparison between the two cortical areas, namely the sensorimotor and visual cortices. A $p < 0.05$ is considered significance.

Figure 11 shows the quantitative comparisons of the normalized brain volumes cortical connectivity (defined as the brain volume exhibiting cortical connectivity divided by the total intracranial brain volume) and the z-score values in regions exhibiting temporal correlation for all age groups. In the sensorimotor area (Figure 11(a)), the percent brain volumes of cortical connectivity of both the 1yr ($p<0.05$) and 2yr old ($p<0.01$) groups are significantly larger than the 2wk old group while no differences are observed between 1 and 2 yr old groups. In contrast, only the 2yr old group has a significantly larger volume when compared with the neonate group ($p<0.05$) in the visual area (Figure 11(b)). Interestingly, a paired t-test reveals that the percent brain volume of cortical connectivity in the sensorimotor area is significantly larger than that in the visual area for the 1 yr old group ($p<0.05$), suggesting that there may be differences in the growth trajectory of functional connectivity.

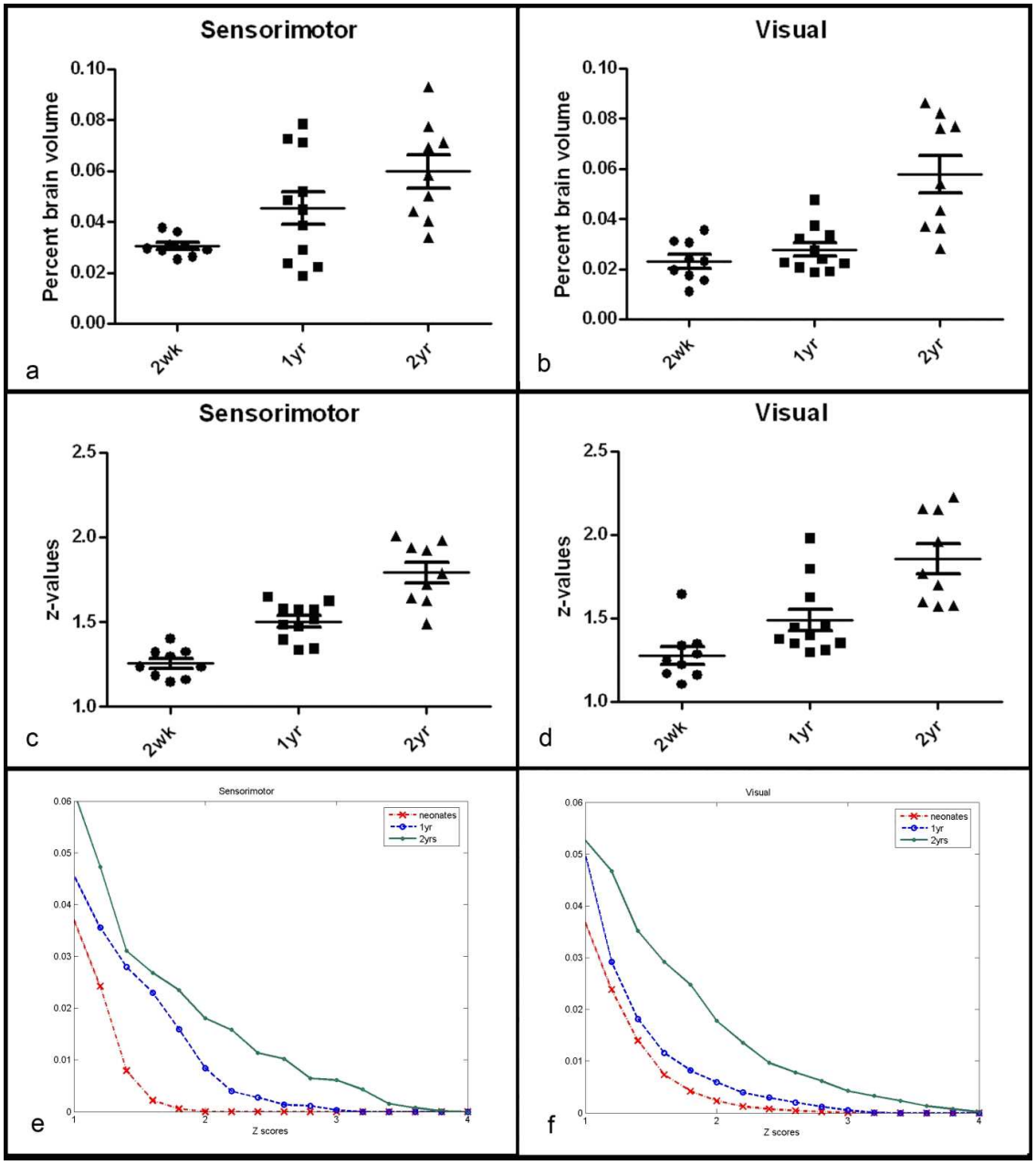

Figure 111. Quantitative comparisons of the normalized brain volumes cortical connectivity in the sensorimotor (a) and visual areas (b). Z-score values in regions exhibiting temporal correlation in the sensorimotor (c) and visual areas (d). Distribution of z-scores in the sensorimotor (e) and visual areas (f).

For the comparison of the z-score values (the "strength" of cortical connectivity) among the three groups, highly significant differences among all three age groups are observed in the sensorimotor area ($p<0.001$); the 2wk old group has the lowest z-score values, followed by the 1yr and 2yr old groups, suggesting that the "strength" of cortical connectivity increases as a function of age (Figure 11(c)). In contrast, the "strength" of cortical connectivity between the 2wk and 1 yr old groups is similar in the visual area (Figure 11(d)) while significantly larger z-score values are observed when comparing the 2 yr old group to the 2wk ($p<0.001$) and 1 yr ($p<0.01$) old groups. No differences are observed between the sensorimotor and visual areas for each age group. Finally, the distribution of z-scores for all three age groups in the sensorimotor and visual areas are shown in Figure 11(e) and (f), respectively. Notice the population toward high z-score values continue to increase from 2wk to 2yr in the sensorimotor area, while this increase is more subtle between 2wk and 1yr old groups in the visual area, consistent with that shown in Figure 11(c) and (d).

4.3.10 Results and Conclusions

4.3.10.1 Seed signals

An example demonstrating manually selected voxels for the primary motor, sensory and visual cortices is shown in Figure 9(a) and (b) using MP-RAGE images

obtained from a 2yr old subject. The averaged MR signals from three subjects, one for each age group in these manually selected regions, are shown in Figure 12(c) and (d) for sensorimotor and visual cortices, respectively. Note these signals were processed using the steps outlined in the section 4.3.4. Several interesting features are noticed in the signal among the three subjects, and between the sensorimotor and visual cortices. First, the signals exhibit a similar pattern to that typically observed in task-activated fMRI studies where both "on" and "off" states are observed ("on" and "off" reflects the increase and decrease in MR signal). Second, the differences between the maximum and minimum percent signal changes for each subject in the sensorimotor and visual cortices are shown in Figure 12(e) and (f), respectively. An age dependent pattern is clearly apparent, the percent signal differences increase as age increases. Although the medians vary significantly among the three groups ($p=0.02$), statistical differences are only observed between the 2wk and 2yr groups for both sensorimotor and visual areas ($p<0.05$) after correcting for multiple comparisons.

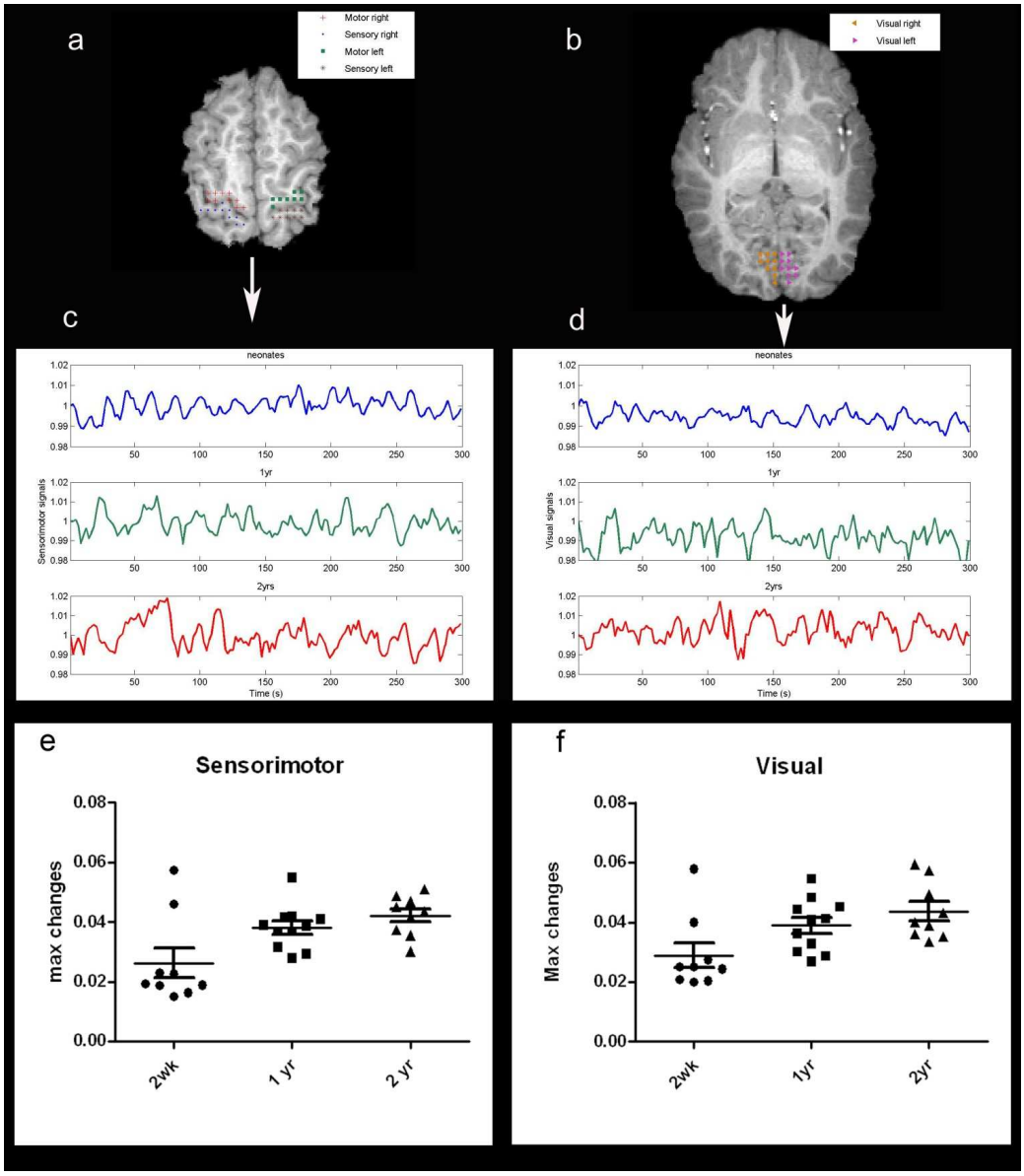

Figure 122. Representative examples for ROI selections and the seed signals in CCA approach. The anatomical locations of the selected ROIs for the sensorimotor and visual areas are shown in (a) and (b), respectively. The averaged seed signals for all three age groups in the sensorimotor and visual areas are shown in (c) and (d), respectively. The differences between the maximum and minimum percent signal changes for each subject in the sensorimotor and visual cortices are shown in (e) and (f), respectively.

4.3.10.2 Brain functional development in the pediatric subjects

In the context of our study, we have observed cortical functional connectivity in all age groups, suggesting that cortical functional connectivity exists at least at 2wks after birth. In addition, cortical functional connectivity appears to increase as a function of age, including an increase in the percent of brain volume as well as the augmentation of the z-score values from the ages of 2wks to 2 yrs old.

Two main features in our results warrant additional discussion. First, although the general pattern of increasing percent brain volume exhibiting high temporal correlation as a function of age is similar in both sensorimotor and visual areas, a progressive increase in volume from 2wks to 2yrs old is observed in the sensorimotor area with the 1 yr and 2 yr old groups showing significantly larger volume of cortical connectivity than that of the neonate groups. In contrast, a subtle increase, followed by a marked elevation in brain volume of cortical connectivity is observed from 2wks, 1yr, to 2yrs in the visual area, respectively. A paired t-test indicates that although no differences between the sensorimotor and visual areas are observed for both the 2wk and 2yr old groups, a larger brain volume in the sensorimotor exhibiting temporal correlation area is observed when compared with that in the visual area at 1 yr old. These findings suggest that there may be a lag in the development of visual connectivity when compared with the sensorimotor area at 1yr old.

Second, similar findings are also observed examining the z-score among the three groups. Highly significantly differences in the z-score values are observed in all three groups in the sensorimotor areas, while no differences are seen between the neonate and 1 yr old groups in the visual area, consistent with results shown in the histogram analysis. These findings suggest again that the strength of cortical connectivity continues to improve from 2wks to 2yrs in the sensorimotor area while a rapid increase in cortical connectivity in the visual area is not observed until between 1yr and 2yrs old.

Although the exact physiological underpinnings accounting for the observed discrepancies in the trajectories of developing senorimotor and visual cortical connectivity from 2wks to 2yrs are largely not known, Chugani et al [117] reported that the most prominent area of metabolic activity in the cerebral cortex is the primary sensorimotor area in infants based on the local cerebral metabolic rates for glucose (ICMRGlc). Specifically, the ICMRGlc at the sensorimotor area is about 93% and 125% of that in adults at 0-1 yr and 1-2yrs, respectively. In contrast, ICMRGlc at the occipital cortex is about 76% and 1.13% of the adults at 0-1yr and 1-2yrs, suggesting the temporal differences in glucose utilization between the sensorimotor and visual areas. Therefore, it appears that our results are consistent with those reported using ICMRGlc.

Nevertheless, more systematic studies will be required to further understand the links between the alteration of glucose utilization and fcMRI in the developing brain

4.4 Correlation analysis in multiple frequency ranges

Next, we explore the estimation of frequency-dependent correlation matrices to characterize functional connectivity between sensory, motor and visual cortices in neonates (2-4 weeks), one and two-years-old children. The overall procedures for the proposed correlation analysis in multiple frequency ranges are shown in Figure 13 and detailed descriptions for each step are given below. The steps identical to CCA are not listed here.

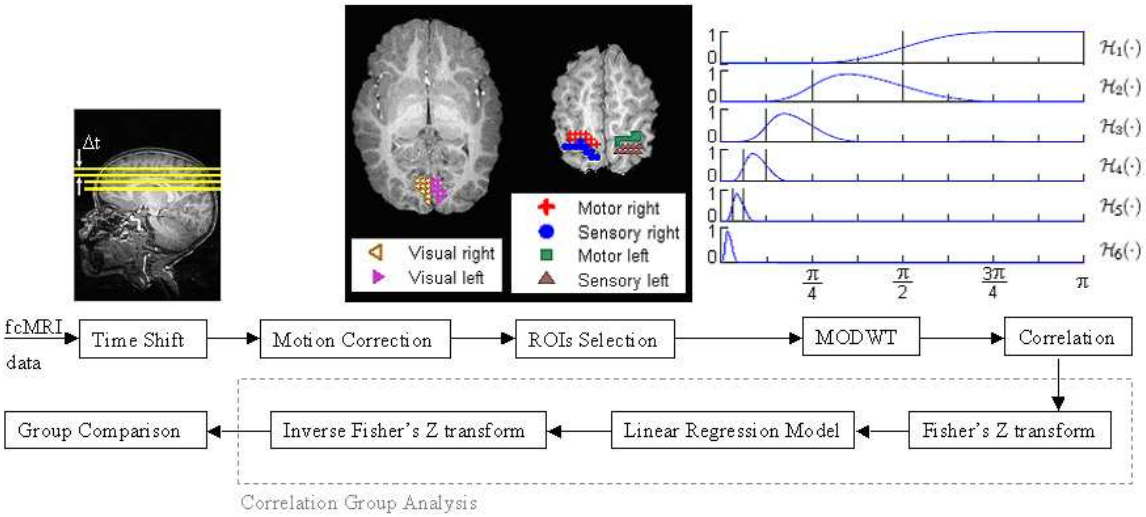

Figure 133. Flowchart for frequency-dependent correlation analysis.

4.4.1 MODWT for signal separation into multiple frequency ranges

Unlike the discrete wavelet transform (DWT), which is orthonormal by filtering and downsampling, maximal overlap discrete wavelet transform (MODWT) [118] can perform multi-resolution analyses in a very redundant way and keep all the coefficients removed from DWT by downsampling. MODWT-based approach resamples data in time and space, and keeps details and smoothness in each level. Therefore, MODWT was used in this study to decompose fcMRI time series into multiple component waveforms with different frequency bands for further statistical analysis. The Wavelet Toolkit for MATLAB is available for download from the WMTSA toolkit web site: http://www.atmos.washington.edu/~wmtsa.

MODWT was applied to each times series in all 6 ROIs by means of the 8-tap Daubechies least asymmetric (LA8) filter that is a better match to our data than Haar and Daubechies class because of its symmetry properties. MODWT-based approach separated the time courses $X(t)$ into a hierarchical series of band-pass filtered detail curves $D_j(t)$ and a hierarchical series of low-pass filtered smooth curves $S_j(t)$, where the index j represents the order of scaling. At the J^{th} level, the signal was decomposed as $X(t) = S_J(t) + \sum_{j=1}^{J} D_j(t)$. The band-pass frequency intervals included B1 0.25-0.5Hz; B2 .125-.25Hz; B3 .063-.125Hz; B4 .031-.063Hz; B5 .016-.031Hz; and B6 0.008-0.016Hz,

respectively. Frequency below <0.008Hz is most likely contaminated by the scanner drifts, other potential confounds and thus was not considered in this study.

4.4.2 Correlation matrices of ROIs at each frequency for each subject

The median of the decomposed wavelet coefficients across all voxels within a specific ROI was first calculated as a robust representative time series in each of the six ROIs at each frequency for all the subjects. A 6×6 correlation matrix based on those representative time series from all 6 ROIs at each frequency band was then obtained. As a result, six correlation matrices were obtained for each subject, representative the six frequency ranges.

4.4.3 Correlation group analysis

Since correlation coefficients were not normally distributed, Fisher's Z-transformation of the correlation coefficients was employed for all frequencies and subjects. Subsequently, a linear regression model was used to analyze the Z-transformed correlation coefficients across all frequencies and subjects for each pair of ROIs. The age was entered as a predictor with three levels in this model. To minimize the effects of outliers on estimates, a robust procedure in Proc Robustreg (SAS v 7.1, Cary, NC) was used to carry out all statistical analysis. We tested the differences among the three age groups for each correlation coefficient. Finally, we took an inverse Fisher's

Z-transformation of the estimated mean level to obtain an estimate of the averaged correlation coefficient for each pair of ROIs in each age group at each frequency, respectively.

4.4.4 Results and Conclusions

Only highly correlated regions (correlation coefficient>.4) were considered. The findings are summarized in Figure 14 and discussed below. First, no correlation was observed in the first two high frequency ranges (B1 & B2). Second, the correlation between right and left visual cortices is consistent throughout B3-B6 for the one and two year old groups, but no correlation was found in the neonate group. Third, the correlation between right and left motor cortices persists for all ages from B4 to B6. Fourth, right and left sensory cortices are highly correlated with each other in B4 and B5 but not B6. Finally, sensory cortex is correlated with motor cortex in B5 and B6 for all ages.

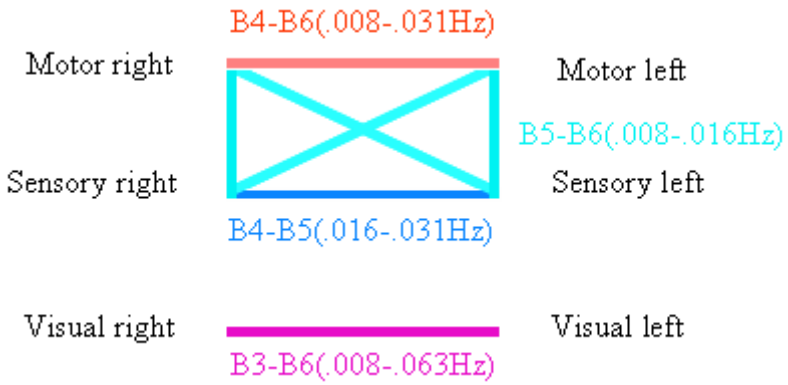

Figure 144. The structure of correlation matrix in different frequency ranges for all three age groups.

Cortical functional connectivity is confirmed in spatially segregated regions; bilateral sensory and motor connectivity is observed for all age groups while bilateral visual cortex connectivity is only observed in the one and two-year old groups. In addition, cortical connectivity is frequency dependent. It is evident that no correlation is observed for the two highest frequency ranges (B1 and B2) in all three cortices evaluated. In contrast, while the low-frequency connectivity is verified in sensory-motor and visual cortices, there are particular frequency ranges related to different cortex connectivity, as listed in Figure 14. Finally, functional correlation between motor and sensory is observed in the frequency ranges of B5 and B6, no correlations are observed between sensory-motor and visual cortices in all the three age groups. While additional studies are needed to further confirm the findings of our current study, this study

represents the first step toward the investigation of brain circuitry during normal brain development using fcMRI and confirms that low frequency fluctuation of resting-condition BOLD signal can serve an indication of neurophysiological development in normal children [17, 37, 46].

5. Spatial ICA in fcMRI for Pediatric Subjects

In this chapter, spatial independent component analysis (ICA) is applied in fcMRI data to separate multiple physiological and artifact-related signal sources. We study the cortical connectivity maps and the activation time courses corresponding to two specific functions: sensorimotor and visual in three age-groups: neonates (2-4 weeks), one and two years old children. Based on our results, the size and the strength (z-score) of activated regions indicate an age-dependent effect, increase as a function of age and these findings agree with the knowledge of brain development in the early age. In addition, Fourier analysis of time courses show the observed activation in both sensorimotor and visual cortices is associated with low frequencies (0.01-0.05Hz) for all subjects.

5.1 Introduction

In the previous chapter, CCA approach has been successfully applied to fcMRI data in detecting sensorimotor- and visual-function-related brain regions Although the reported promising findings, there are two major problems involved with this technique which utilizes the relationship between a seed signal and the whole brain on a voxel-by-voxel basis [43, 44]. First, the obtained functional connectivity maps show a high dependence on the selective of seed signals. Both the size and location of the chosen

ROIs will affect the seed signals and, therefore, the outcomes of the resulting activation maps. For example, Figure 15 shows two sensorimotor-funtion-related connectivity maps using CCA approaches for the same subjects. The seed signals for these two maps are estimated from two groups of region-of-interests (ROIs), which both consist of a small number of voxels, but are chosen from different locations in the visual cortex. Although the obtained connectivity maps overlap with each other in many areas close to central sulcus, there are clear differences that are visible to naked eyes. Second, CCA is applied to each individual voxel independently and, thus, ignores the relevance between adjacent voxels.

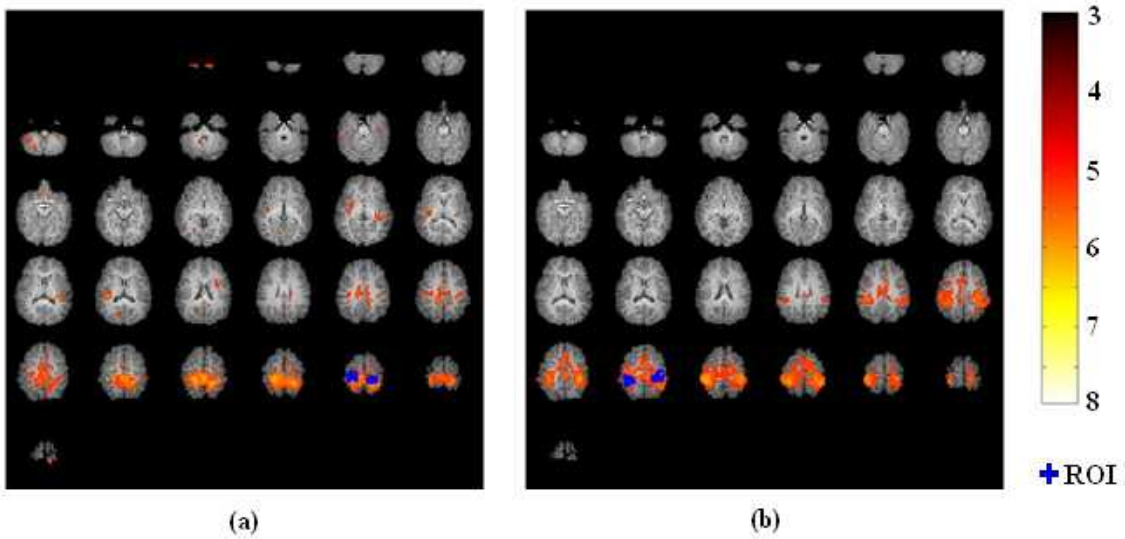

Figure 155. Sensorimotor-function-related connectivity maps using CCA approach with seed signals calculated from two groups of region-of-interests (ROIs) at different locations in visual cortex for the same subject.

As an effective alternation to circumvent the problems of the CCA approach, Independent component analysis (ICA) requires no predefined seed signals or prior knowledge about spatial/temporal patterns of brain activity and performs a blind source separation based on 2nd and higher order relations between voxels. The rationale for the application of spatial ICA (sICA) to fMRI experiments is based on two complementary principles of brain functional organization: *localization* and *connectionism* [45]. *Localization* states that each individual function, e.g. motor, is localized to a small set of specific brain areas while *connectionism* represents that the brain activity associated with a given task may be the functional integration of activity in multiple brain regions. By maximizing both the statistical independence and the non-Gaussianity of the source signals, spatial ICA can decompose fMRI signals into various sources consisting of a unique time course of activation and a corresponding 3D component map. Each brain function may be represented by one or more resulting spatially-independent sources. Spatial ICA was first applied to fcMRI data analysis on anesthetized child patients (5 to 12 years old) by Kiviniemi et al. [46] and then on normal adult subjects by van de Ven VG et al. [44] and Ma L et al. [43]. It has been reported in these applications that spatial ICA was able to identify functional connectivity in sensory and motor cortices, as well as in several parietal and frontal regions. The frequency analysis of function-related time courses showed a dominant peak at 0.03 Hz on anesthetized child patients [46] and a prevailing

frequency band within the extremely low range (0.01-0.05 Hz) on normal adults [44]. Moreover, based on the overall performance and the robustness to structured noise reported by Ma L et al., spatial ICA appears to be superior to CCA [43]. Based on these previous findings, fcMRI was employed in this study to examine cortical connectivity in neonates (2-4wks), one-year and two-years old children in a state of sleep. Spatial ICA was applied to identify the signal sources of different functional activities and Bayesian information criterion (BIC) was used to estimate the optimal number of independent components (ICs). Results were visually inspected and the ICs that depict functionally connectivity in two predefined anatomical regions: visual and sensorimotor cortices were identified for further investigation. Their spatial, frequency, and connectivity characteristics were analyzed afterwards in order to get the information about the brain function and how it develops in the very early age (0-2 years).

5.2 Spatial ICA analysis for fcMRI

Figure 16 shows the procedures to obtain brain functional connectivity maps using spatial ICA approach. A more detailed description for each step particular for spatial ICA technique is provided below. For those steps similar to CCA method, please refer to the previous chapter for more details.

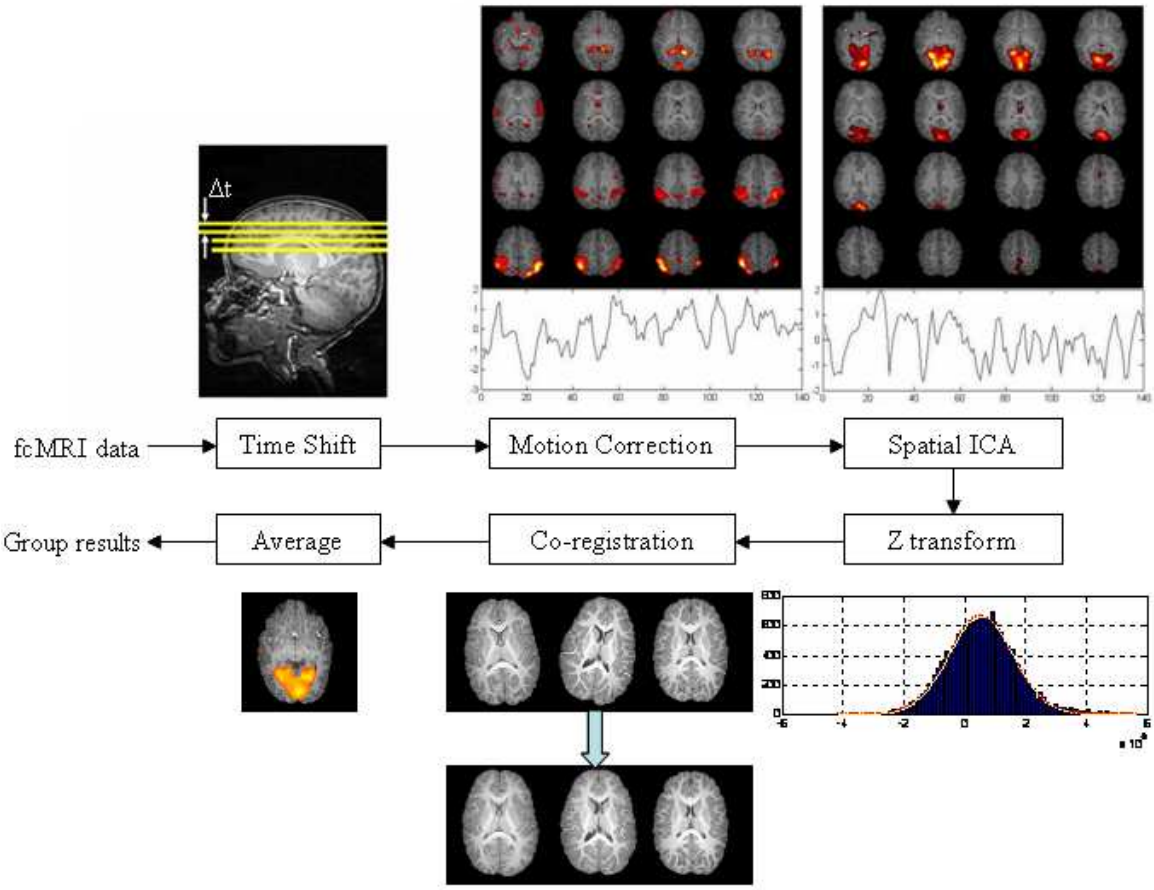

Figure 166. Flowchart for spatial ICA technique in the fcMRI brain development study.

5.2.1 Spatial ICA

The ICA had ability to separate spatially independent signal sources related to nondeterministic physiological fluctuations as well as artifacts from resting state datasets. Currently, the two open questions for Spatial ICA on fcMRI analysis are how to determine the optimal number of independent sources and how to determine the

threshold. To address the first question, BIC was adopted in this work to approximate the number of independent sources to balance the goodness of fit and the complexity. The estimated numbers were quite consistent within one and two years old group, but had a lot of variations for neonate cases, which might due to the functional connectivity in newborns was less sensitive and the signal-to-noise ratio (SNR) were worse than others. For the second question, one fix threshold was set for all the groups in order to obtain the activation maps at the same statistical significance level for further analysis.

Spatial ICA was implemented with the infomax ICA algorithm [115], a freely available DTU toolbox developed in the MATLAB programming environment, and the number of independent components were estimated using Bayes Information Criterion (BIC) [116].

Spatial ICA decomposed fcMRI data into several sources consisting of a unique time courses of activation and a corresponding 3D component map. Each brain function may be represented by one resulting spatially-independent source. The independent maps were then converted to z maps for thresholding using the equation $Z_i = \frac{I_i - \mu}{\sigma}$, where I_i is the *i*-th voxel value in the component map, and μ & σ are the mean & standard deviation of all the voxels of the same map. The resulting z maps were then thresholded by $|Z| \geq 3$ to make the so-obtained activation maps for all the subjects had the same level of statistical significance. We overlaid the component maps onto the co-

registered MP-RAGE images of the same subject, and then visually examined the spatial ICA results to identify the components that corresponding to sensorimotor and visual functions. In addition, the corresponding time courses were collected for spectrum analysis to investigate the full-width-half-maximum (FWHM) frequency range associated with sensorimotor and visual functions.

5.2.2 Postprocessing

For each pediatric group, one MP-RAGE template was chosen for group analysis. All the activation maps were co-registered to the template of the same ages using the transfer matrix between their own MP-RAGE images and the template. Because the maps have been co-registered with the MP-RAGE images of the same subjects, the activation maps within groups were thus all registered to the same template after the above co-registration procedure. FSL affine registration was chosen here for cross-subjects registration. Finally, group results were averaged from the registered activation maps.

5.2.3 Results

5.2.3.1 Number of spatially-independent sources for fcMRI data

The numbers of independent components estimated using BIC vary for different neonate datasets, but are quite consistent for one and two years

old group. Explicitly, for neonates, the number of independent sources could be any number between 9 and 13; for one year olds, the number is 14 for nine cases and 13 for the other two; for two year olds, the number is 14 for eight cases and 15 for one subject.

5.2.3.2 Selection of IC sources for sensorimotor and visual cortices

All the spatial ICA results were visually examined while the 3D independent component maps were overlaid onto the co-registered MP-RAGE images of the same subjects. One component corresponding to sensorimotor function, which was located near central sulcus, was identified for all the subjects except for one neonate case, and one component that represented functional connectivity of visual cortex, which was located in the occipital lobe, was recognized for all the subjects in one and two years old group, but there was no single visual component found for the whole neonate group.

5.2.3.3 Spatial distribution of sensorimotor and visual functions

Figure 17 shows all the z-maps corresponding to sensorimotor function overlay onto the anatomical images and only one slice was chosen for each case. The overlays for neonate, one year old and two years old subjects were shown in the top, middle and bottom rows, respectively. Figure 18 illustrates all the z-maps representing the activation of visual function for one (top row) and two (bottom row) years old children. The

observed activation areas looked consistent in the locations for both sensorimotor and visual functions.

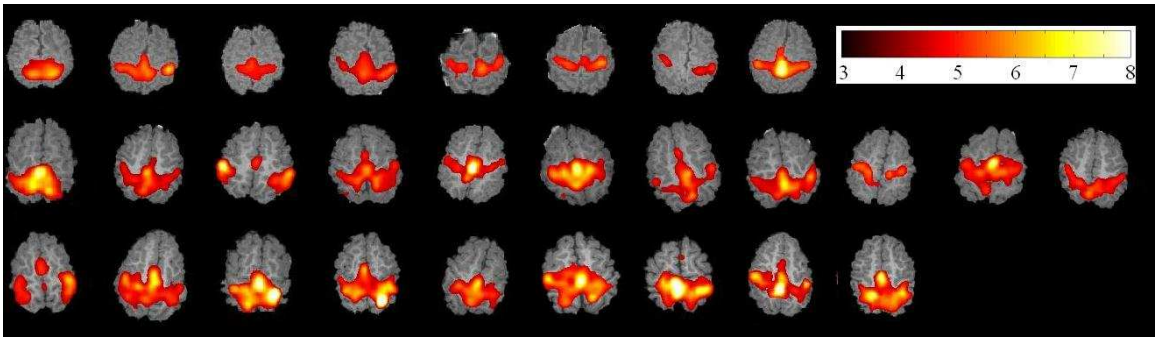

Figure 177. Single-slice illustration for independent sources associated with sensorimotor cortex. The neonates, one and two years old subjects were displayed in the top, middle and bottom rows, repectively.

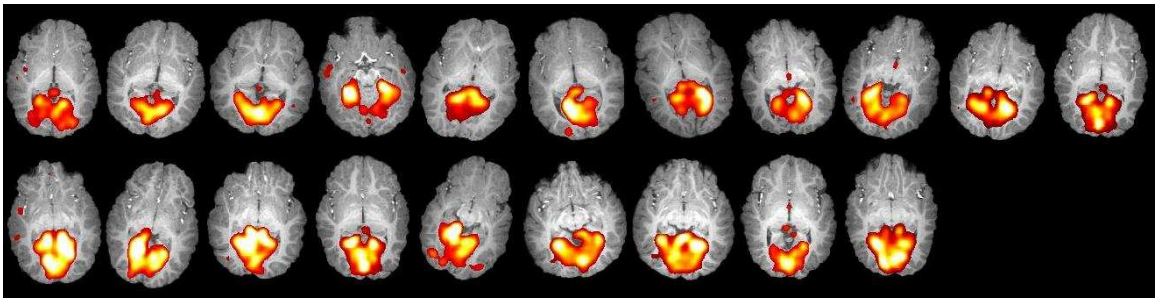

Figure 188. Single-slice illustration for independent sources associated with visual cortex. The one and two years old subjects were displayed in the top and bottom rows, repectively.

5.2.3.4 Frequency analysis of the time courses of functional activation

Frequency plots of the chosen component time courses for the first subject in each age-group (Figure 17 and Figure 18) were presented in Figure. The fluctuation at low frequency range (<0.05Hz) had major contributions to the spectrum in all the cases. FWHM of the time courses corresponding to sensorimotor and visual functional connectivity were always within the low frequency range (0.01-0.05Hz) for all the subjects. These findings were similar to all the previous reports [17, 18, 39, 44, 46].

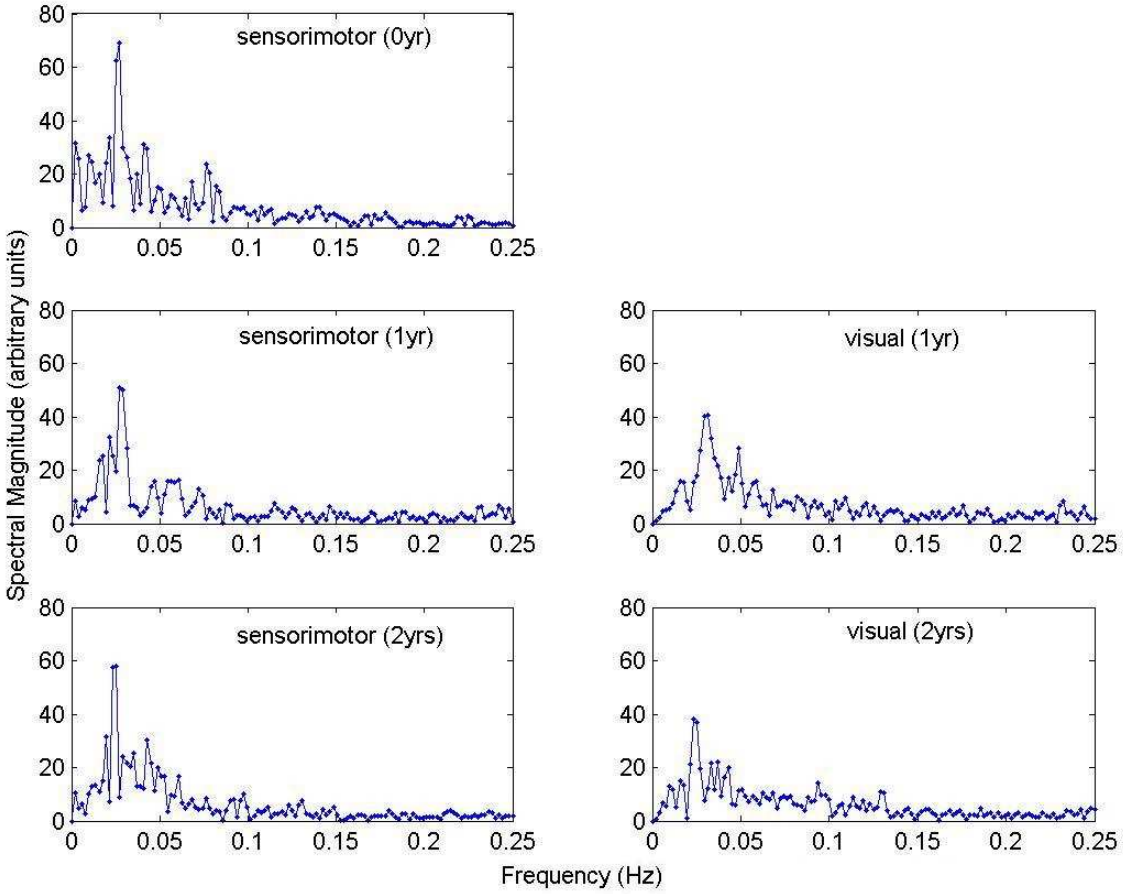

Figure 29. Spectrum illustration of the selected time courses related to sensorimotor and visual functions for neonate, one-year-old and two-years-old examples.

5.3 Automatic component identification for spatial ICA

As a data-driven method, sICA requires no predefined seed signals or prior knowledge about spatial/temporal patterns of brain. The spatial ICA is able to separate

the resting-state fcMRI datasets into spatially independent signal sources, which are related to nondeterministic physiological fluctuations as well as motion artifacts. However, the spatial ICA results need to be visually examined in order to determine the ICs which are corresponding to functional connectivity based on their anatomical locations, as stated in section 5.2.3.2. For example, the component corresponding to sensorimotor function is located near central sulcus, and the component that represents functional connectivity of visual cortex is located in the occipital lobe. As evident, this final step also requires user inputs, can introduce biases and is tedious.

Based on the Frequency analysis of the time courses of functional activation, the fluctuation at low frequency range (<0.05Hz) had major contributions to the spectrum in all the cases. FWHM of the time courses corresponding to sensorimotor and visual functional connectivity were always within the low frequency range (0.01-0.05Hz) for all the subjects as shown in Figure. Moreover, after examining the spatial ICA results for all the fcMRI datasets, we observe an interesting phenomenon: the activation areas for the components showing the high-frequency dependence are all related to big vessels. For example, Figure 19 lists three activation maps (left column) and the spectrum (right column) of their corresponding time courses for the representative neonate (top row), one-year-old (middle row) and two-years-old (bottom row) subjects.

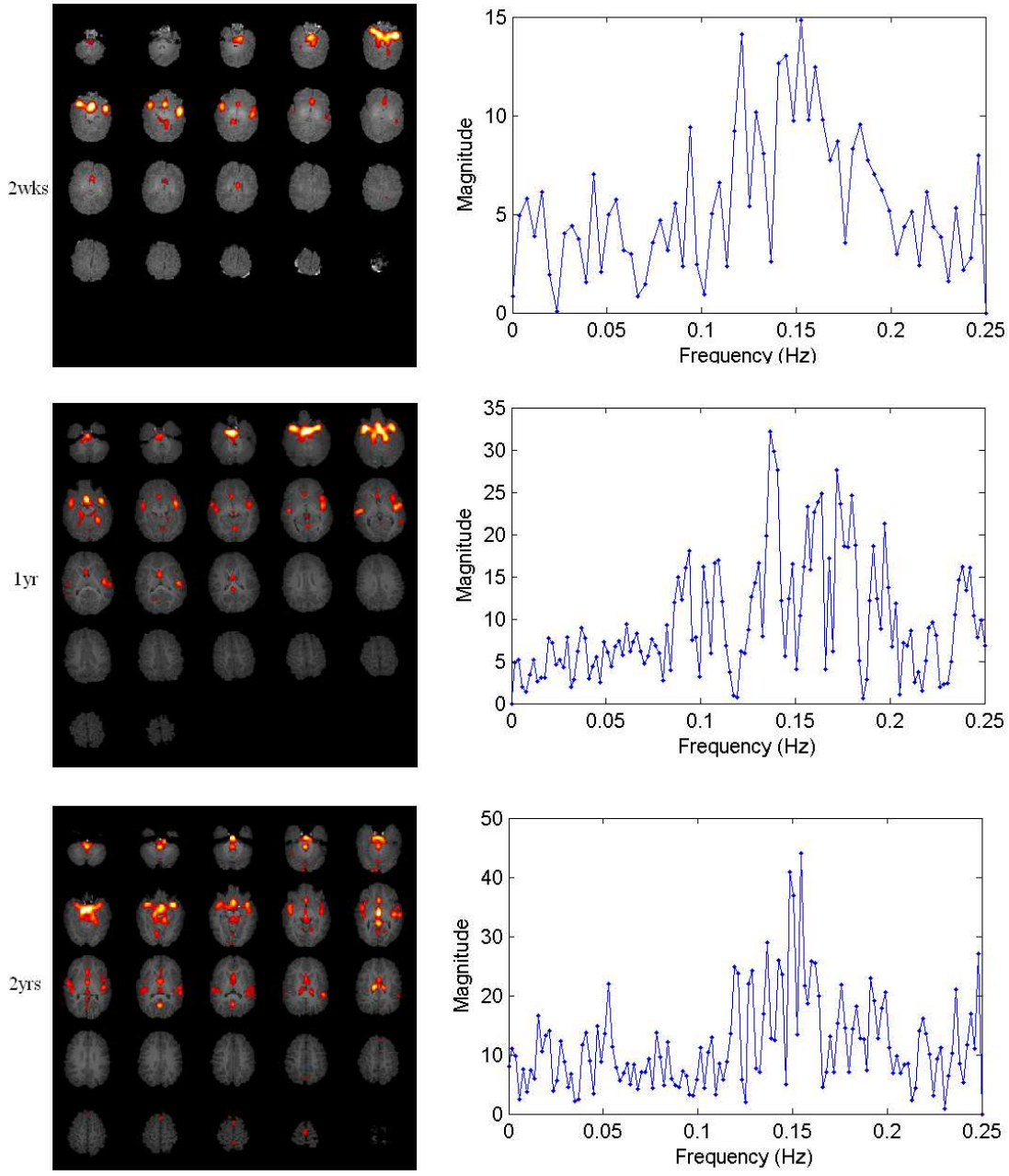

Figure 190. Representive exmaples of high-frequency ICs for neonate (top row), one-year-old (middle row) and two-years-old subjects (bottom row). Activation overlays are shown in the left column and the spectrum illustrations of the corresponding time courses are shown in the right column.

Based on these findings associated with the spatial ICA results, we propose an automatic procedure to determine the components that most likely reflect brain functional connectivity. The proposed automatic identification involves two steps. First, boundary detector was used to exclude the motion-related sources that could be either low or high frequencies. Second, since the low-frequency synchronization (cutoff frequency ~0.08Hz) has been implicated to be responsible for brain connectivity, a spectrum analysis was performed and only sources showed low-frequency activations (<0.08Hz) were kept. The sICA maps of the chosen sources were converted to Z maps with a normal distribution using Z-test so as to allow group analysis. For comparison, sensorimotor and visual activation maps calculated using CCA approach were also combined together.

The average Z maps for the neonate, one-year and two-year old groups are shown in Figure 20 using CCA and Figure 21 using sICA, respectively. Comparing these two figures, it is evident that the functional connectivity maps are similar between CCA and sICA approaches, suggesting that the proposed automated approach is effective. Activations are observed in the primary sensorimotor and visual cortices through all three age groups. It is apparent that both the size and the strength of the activation areas increase as a function of age.

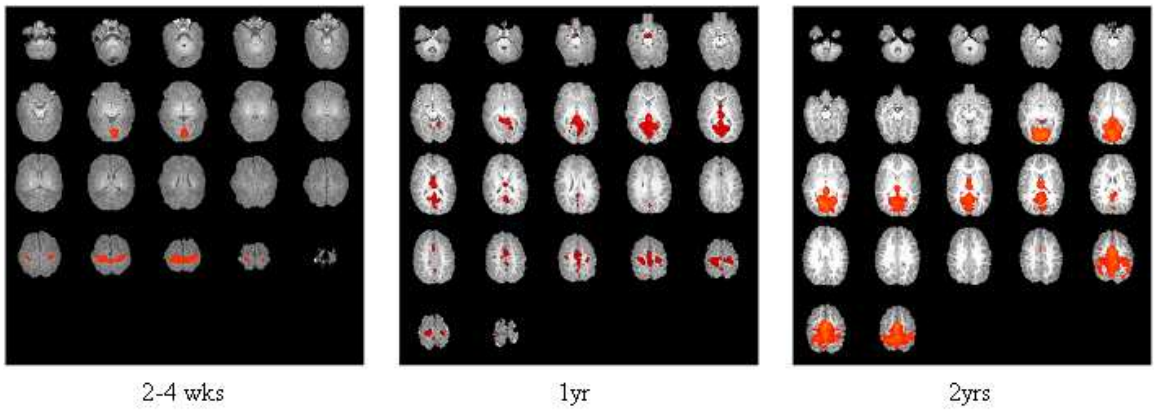

Figure 201. Group average for brain functional connectivity using CCA in normal and healthy peadiatric subects.

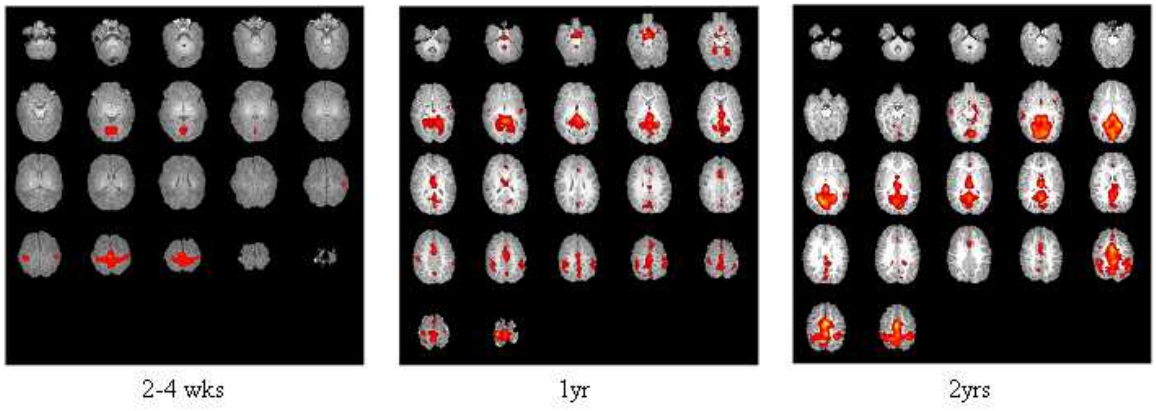

Figure 212. Group average for brain functional connectivity using sICA in normal and healthy peadiatric subjects.

5.4 Conclusions and Discussions

As a data-driven, distribution-based method, spatial ICA is applicable to separate multiple function-related activation dynamics from the artifacts using the

estimated number of sources based on BIC. The obtained spatial and frequency characteristics of the functional sources agree with the previous knowledge of brain function and its development for normal pediatric subjects. Since this approach does not require any task-related activation, it offers a means to shed light on our understanding of functional development in all ages.

The proposed automated selection approach for independent components reflecting functional connectivity is feasible and results are similar between CCA and sICA. Nevertheless, it appears that sICA provides additional regions exhibiting functional connectivity which are not seen using CCA. Specifically, the results between CCA and sICA are extremely similar in the neonate group but discrepancies are observed for both 1 and 2 yrs old groups. One could speculate that sICA reveals additional regions exhibiting functional connectivity beyond the sensorimotor and visual cortices identified based on CCA. Further analysis will be required to determine the physiological underpinnings of these discrepancies between sICA and CCA

One of the major limitations for the fcMRI studies, however, is that the complexity of our mind may never be at a resting condition, especially in the awake state of adult subjects. This is despite the fact that subjects were instructed to think of nothing during the scanning procedures. In contrast, the very young pediatric subjects (<2yrs) in this study may more resemble the true default mode of brain function at these

ages as it may be reasonable to believe that the external environmental factors are minimal and complex thinking processes are yet to be developed in these young minds. Our results suggest that there is a continued improvement in cortical functional connectivity from 2wks to 2yrs old. Nevertheless, one must be cautious that the brain at these ages is undoubtedly undergoing tremendous development in synaptic connection and is extremely dynamic. Therefore, results obtained in our studies will be age-specific and are unlikely to be generalized to different age populations. Nonetheless, the simplicity of fcMRI regarding data acquisition should greatly facilitate further investigation of different age groups with a much smaller age interval between groups, so as to allow detailed investigation of the early brain development of the tightly coupled neuronal network.

6. Summary and Extensions

In this chapter, the contributions of this dissertation are briefly summarized, and then the possible further developments to extend our work are discussed.

6.1 Summary

My doctoral research focuses on the signal processing and post analysis in time series of functional magnetic resonance imaging (fMRI) for human brain mapping. There are totally four major contributions made in this dissertation.

First, we proposed a new methodology to effectively minimize the effects of recirculation independent of the presence or absence of ischemic lesions, and to provide quantitative measures of cerebral hemodynamics, especially CBF, for DSC-MR perfusion data. Therefore, we could provide more accurate estimation of the tissue outcome for acute ischemic stroke patients.

Second, we proposed a robust clustering method for high-dimensional image segmentation based on ROBPCA subspaces and mixtures of T distribution. The new method could separate gray and white matter in both pathological and non-pathological areas for DSC-MR perfusion data of ischemic stroke patients at the hyperacute phase. This approach could be extended to other image datasets, such as CT perfusion, breast MRI to detect cancer tumors.

Third, we applied the fcMRI experiments on neomates, one and two years old normal children to not only prove the presence of cortical functional connectivity in very young healthy children, but also to demonstrate how cortical functional connectivity increases in the developing brain. This is the original research to study the brain development in the pediatric subjects. Moreover, we proposed a statistical method to delineate frequency-dependent brain connectivity among brain activation regions.

Finally, we proposed an automatic procedure combined with spatial ICA approach to determine the brain functional connectivity. The new technique requires no predefined seed signals or prior knowledge about spatial/temporal patterns of brain, and therefore provides a practical way to study brain functional connectivity and insights into normal brain development in pediatric subjects.

6.2 Future Research Arenas

In this dissertation, we have demonstrated that functional connectivity exists in children as early as 2wks old and results are highly age-dependent. However, the research was a cross-sectional study and focused on functional connectivity in the primary motor, somatosensory and visual cortices. In the future, this work should be extended to more cortical connectivity, and more important, we should be able to study the development of functional connectivity for the same subjects at multiple ages. In this section, we report some preliminary results on a longitudinal study where BOLD

synchronization was employed to explore the development of cortical connectivity in the Broca's and Wernicke's areas and Anterior Cingulate cortex (ACC) in pediatric subjects from 2wks to 2 yrs old.

A total of 8 children were recruited where 3 subjects were scanned at both 2-4 weeks and one year old, and 5 subjects were scanned at one and two years old. Informed consent was obtained from the parents prior to imaging. All of the subjects were imaged during sleep (no sedation was employed). The protocols and methods are same as those described in Chapter 4. After the preprocessing, a board certified neuroradiologist manually drew 3 ROIs located in the Broca's and Wernicke's areas and ACC, respectively, for each subject. Cross correlation was then conducted throughout the entire brain using each voxel in each ROI as the reference signal. The cross correlation coefficients were converted to z-scores with a normal distribution. Representative Z map for each ROI was finally obtained using a robust median operation. Pixels with a z-score > 1 were considered as the activated voxels.

Figure 22 shows the functional connectivity overlays in Broca's (up row) and Wernicke's (middle row) areas, and ACC (bottom row) for neonate (1st column), one year (2nd column) and two year olds (3rd column). Individual subjects are represented by different colors. It is evident that the "putative" cortical connectivity is age-dependent. The number of "activated" voxels increases as a function of age although it appears to be

non-linearly dependent on the age. Specifically, a marked increase of activated voxels is observed in the Broca's and Wernicke's areas from 1yr to 2 yrs old while a major increase is observed from 2wks to 1yr old in the ACC area. In addition, the ACC area appears to have more activations when compared with those in the Broca's and Wernicke's areas at 1yr old, suggesting that the development of attention may pre-date the development of language. Moreover, it appears that there are some overlaps between the results obtained using ROIs defined in the Broca's and Wernicke's areas, respectively. In other words, when the signal in the Broca's area was used as the reference function for correlation analysis, high temporal correlation is observed in the Wernicke's area and vice versa, suggesting functional connections between the Broca's and Wernicke's areas. This finding is not surprising since the Broca's area is connected to the Wernicke's area by the arcuate fasciculus and these two areas are known to involve in the understanding and comprehension of spoken language.

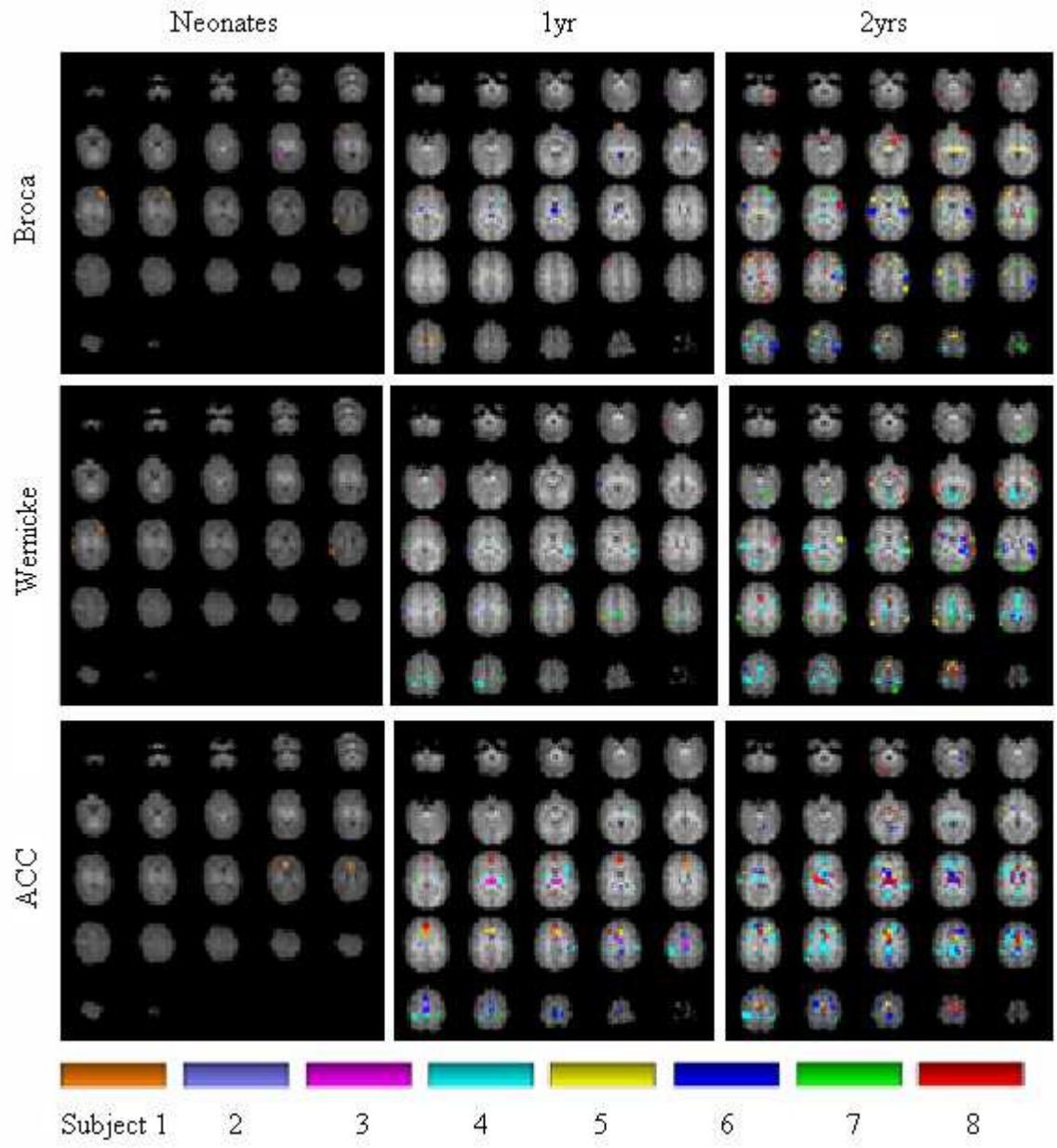

Figure 223. Functional connectivity overlays in Broca's (up row) and Wernicke's (middle row) areas, and ACC (bottom row) for neonate (1st column), one year (2nd column) and two year olds (3rd column).

Appendix A – Multivariate *T* distribution

Multivariate Gaussian distributions have been increasingly used to statistically model a wide variety of nature phenomena due to their asymptotic properties and computation convenience [43-45]. The model parameters can be easily estimated by the iterative expectation-maximization (EM) algorithm [46, 47]. However, the fitting of Gaussian distributions lacks robustness to the data with atypical points or with longer than normal tails [46]. Two-component Gaussian mixture is used to extend this parametric family for potential outliers or observations with heavy tail.

$$f\left(\mathbf{x};\mu,\Sigma,\varepsilon,c\right)=(1-\varepsilon)f_{gauss}\left(\mathbf{x};\mu,\Sigma\right)+\varepsilon f_{gauss}\left(\mathbf{x};\mu,c\,\Sigma\right)$$

where c is large and ε is small, which mean that only small proportion of data show a relatively large variance. Furthermore, a more general form is proposed by Huber [48].

$$f\left(\mathbf{x};\mu,\Sigma,u\right)=\int f_{gauss}\left(\mathbf{x};\mu,\Sigma/u\right)f(u)du \tag{A1}$$

where u is assumed to be a chi-squared random variable with the degree of freedom υ, i.e.

$u \sim f_{gamma}\left(\frac{\upsilon}{2}, \frac{\upsilon}{2}\right)$. Utilizing $\Gamma(\alpha) = \int_0^\infty u^{\alpha-1} e^{-u} du$, The mixture model (A1) can be written as

$$f_t\left(\mathbf{x}; \mu, \Sigma, \upsilon\right) = \frac{\Gamma\left(\frac{\upsilon + p}{2}\right) |\Sigma|^{-1/2}}{(\pi\upsilon)^{\frac{p}{2}} \Gamma\left(\frac{\upsilon}{2}\right) \left(1 + \frac{\delta}{\upsilon}\right)^{\frac{\upsilon+p}{2}}} \tag{A2}$$

where $\delta = (\mathbf{x} - \mu)^T \Sigma^{-1} (\mathbf{x} - \mu)$. This distribution (A2) is the well-known multivariate *T* distribution. It is identified as an alternative to the Gaussian distributions for robust statistics because it has a tunable tail and is less sensitive to atypical observations [35, 49]. The degree of freedom υ parameterizes the 'robustness' of the distribution, i.e. how wide the tails are. The extreme case $\upsilon \to \infty$ represents a Gaussian distribution and the case υ=1 corresponds to a wide tailed multivariate Cauchy distribution.

Appendix B – EM estimation for mixtures of multivariate *T* distribution

The condensed data is denoted by a matrix **Y** with the dimension m×n (m=10 after ROBPCA process). Each data point y_i (i=1,…,n) is considered as a sample from a g-component mixture of *T* distributions given by

$$f(y_i;\Psi)=\sum_{j=1}^{g}\pi_j f(y_i;\mu_j,\Sigma_j,\upsilon_j)$$

where the model parameters $\Psi=(\pi_1,\cdots,\pi_{g-1};\theta_1,\cdots,\theta_g;\upsilon_1,\cdots,\upsilon_g)$ and $\theta_j=(\mu_j,\Sigma_j)$. There are *g-1* parameters of π_j, *tg* parameters of μ_i, *(t+1)tg/2* parameters of Σ_i, and *g* parameters of υ_j. Thus, the total number of the unknown parameters is

$$J=g(t^2+3t+4)/2-1 \qquad \text{(B1)}$$

which represents the complexity of the proposed model.

The best-fitting parameters are determined by maximizing the likelihood of the data, i.e. the probability of obtaining the given dataset from the model. To facilitate the EM algorithm, two sets of auxiliary variables are first introduced with the knowledge that *T* distribution is an extension of Gaussian families as deducted in Appendix A:

z_{ij}: membership of data point y_i to jth component (z_{ij}=1 indicates y_i belongs to jth component; 0 otherwise).

u_{ij}: weight representing 'typicality' of y_i with respect to jth component.

$$P\left(z_{ij}=1\right)=\pi_j$$

$$P\left(u_{ij}\mid z_{ij}=1\right)=f_{gamma}(\frac{\upsilon_j}{2},\frac{\upsilon_j}{2})$$

$$P\left(y_i\mid u_{ij},z_{ij}=1\right)=f_{gauss}(\mu_i,\Sigma_i/u_{ij})$$

The complete-data likelihood can be written as

$$L_c(\Psi)=\prod_{i=1}^{n}\prod_{j=1}^{g}\left[P(y_i\mid u_{ij},z_{ij})P(u_{ij}\mid z_{ij})P(z_{ij})\right]^{z_{ij}} \tag{B2}$$

$$\begin{aligned}&=\sum_{i=1}^{n}\sum_{j=1}^{g}z_{ij}\log\pi_j+\sum_{i=1}^{n}\sum_{j=1}^{g}z_{ij}\left\{-\frac{1}{2}\log\left|\Sigma_j\right|-\frac{u_{ij}}{2}(y_i-\mu_j)^T\Sigma_j^{-1}(y_i-\mu_j)\right\}\\&-\log\Gamma\left(\frac{\upsilon_j}{2}\right)+\frac{\upsilon_j}{2}\log\frac{\upsilon_j}{2}+\frac{\upsilon_j}{2}\left(\log u_{ij}-u_{ij}\right)-\frac{1}{2}\log u_{ij}-\frac{p}{2}\log 2\pi\Bigg\}\\&=\log L_{1c}(\pi)+\log L_{2c}(\upsilon)+L_{3c}(\theta)\end{aligned}$$

E step

In E step, the memberships and weights are updated using the conditional expectation based on the model parameters estimated in the previous *(k-1)*th iteration.

$$\hat{z}_{ij}^{(k)}=E(z_{ij}\mid y_i;\Psi^{(k-1)})=\sum_{z_{ij}=0,1}z_{ij}P(z_{ij}\mid y_i;\Psi^{(k-1)})=P(z_{ij}=1\mid y_i;\Psi^{(k-1)})$$

$$=\frac{\hat{\pi}_j^{(k-1)}P(y_i;\hat{\mu}_j^{(k-1)},\hat{\Sigma}_j^{(k-1)},\hat{\upsilon}_j^{(k-1)})}{\sum_{j=1}^{g}\hat{\pi}_j^{(k-1)}P(y_i;\hat{\mu}_j^{(k-1)},\hat{\Sigma}_j^{(k-1)},\hat{\upsilon}_j^{(k-1)})} \tag{B3}$$

$$P(u_{ij} \mid y_i, z_{ij}=1) = \frac{P(u_{ij}, y_j \mid z_{ij}=1)}{P(y_j \mid z_{ij}=1)} = \frac{P(y_j \mid u_{ij}, z_{ij}=1)P(u_{ij} \mid z_{ij}=1)}{P(y_j \mid z_{ij}=1)}$$

$$\sim u^{\frac{\upsilon_j+m}{2}-1} e^{-\frac{\upsilon_j+\delta}{2}u} \sim gamma(\frac{\upsilon_j+m}{2}, \frac{\upsilon_j+\delta(y_i,\mu_j,\Sigma_j)}{2}) = gamma(\alpha,\beta)$$

$$\hat{u}_{ij}^{(k)} = E(u_{ij} \mid y_i, z_{ij}=1; \Psi^{(k-1)}) = \frac{\alpha}{\beta} = \frac{\upsilon_j^{(k-1)}+m}{\upsilon_j^{(k-1)}+\delta(y_i,\mu_j^{(k-1)},\Sigma_j^{(k-1)})} \quad \text{(B4)}$$

M step

The model parameters are computed in M step by maximizing posterior probability. Specifically, we take derivatives of conditional expectation of the complete-data log likelihood with respect to parameters $\pi_j, \mu_j, \Sigma_j, \upsilon_j$, respectively, and set them to zero to yield

$$\hat{\pi}_j^{(k)} = \frac{\sum_{i=1}^{n} \hat{z}_{ij}^{(k)}}{n} \quad \text{(B5)}$$

$$\hat{\mu}_j^{(k)} = \frac{\sum_{i=1}^{n} \hat{z}_{ij}^{(k)} \hat{u}_{ij}^{(k)} y_i}{\sum_{i=1}^{n} \hat{z}_{ij}^{(k)} \hat{u}_{ij}^{(k)}} \quad \text{(B6)}$$

$$\hat{\Sigma}_j^{(k)} = \frac{\sum_{i=1}^{n} \hat{z}_{ij}^{(k)} \hat{u}_{ij}^{(k)} \left(y_i - \hat{\mu}_j^{(k-1)}\right)\left(y_i - \hat{\mu}_j^{(k-1)}\right)^T}{\sum_{i=1}^{n} \hat{z}_{ij}^{(k)} \hat{u}_{ij}^{(k)}} \quad \text{(B7)}$$

and $\upsilon_j^{(k)}$ is a solution of the equation

$$\left\{ -\psi\left(\frac{\upsilon_j}{2}\right) + \log\left(\frac{\upsilon_j}{2}\right) + 1 + \frac{\sum_{i=1}^{n} \hat{z}_{ij}^{(k)} \left(\log \hat{u}_{ij}^{(k)} - \hat{u}_{ij}^{(k)}\right)}{\sum_{i=1}^{n} \hat{z}_{ij}^{(k)}} + \psi\left(\frac{\upsilon_j^{(k)} + p}{2}\right) - \log\left(\frac{\upsilon_j^{(k)} + p}{2}\right) \right\} = 0 \tag{B8}$$

References

[1] Barbier EL, Lamalle L, Decorps M, "Methodology of brain perfusion imaging," J Magn Reson Imaging, vol. 13, pp. 496-520, April 2001.

[2] Calamante F, Gadian DG, Connelly A., "Delay and dispersion effects in dynamic susceptibility contrast MRI: simulations using singular value decomposition," Magn Reson Med, vol. 44, pp. 466-73, Sep 2000.

[3] Calamante F, Morup M, Hansen LK., "Defining a local arterial input function for perfusion MRI using independent component analysis," Magn Reson Med, vol. 52, pp. 789-97, Oct 2004.

[4] Ostergaard L, Sorensen AG, Kwong KK, Weisskoff RM, Gyldensted C, Rosen BR., "High resolution measurement of cerebral blood flow using intravascular tracer bolus passages. Part II: Experimental comparison and preliminary results," Magn Reson Med, vol. 36, pp. 726-36, 1996.

[5] Ostergaard L, Weisskoff RM, Chesler DA, Gyldensted C, Rosen BR., "High resolution measurement of cerebral blood flow using intravascular tracer bolus passages. Part I: Mathematical approach and statistical analysis," Magn Reson Med, vol. 36, pp. 715-25, Nov 1996.

[6] Rempp KA, Brix G, Wenz F, Becker CR, Guckel F, Lorenz WJ., "Quantification of regional cerebral blood flow and volume with dynamic susceptibility contrast-enhanced MR imaging," Radiology, vol. 193, pp. 637-41, Dec 1994.

[7] Rosen BR, Belliveau JW, Chien D, "Perfusion imaging by nuclear magnetic resonance," Magn Reson Q, vol. 5, pp. 263-81, 1989.

[8] Rosen BR, Belliveau JW, Aronen HJ, Kennedy D, Buchbinder BR, Fischman A, Gruber M, Glas J, Weisskoff RM, Cohen MS, et al., "Susceptibility contrast imaging of cerebral blood volume: human experience," Magn Reson Med, vol. 22, pp. 293-9, Dec 1991.

[9] Wu O, Ostergaard L, Weisskoff RM, Benner T, Rosen BR, Sorensen AG., "Tracer arrival timing-insensitive technique for estimating flow in MR perfusion-weighted imaging using singular value decomposition with a block-circulant deconvolution matrix," Magn Reson Med, vol. 50, pp. 164-74, July 2003.

[10] Brown MA, Semelka RC, MRI Basic Principles and Applications, third ed. New Jersey: John Wiley and Sona, Inc, 2003.

[11] Hornak JP, The basics of MRI, 1996.

[12] Webb S, The Physics of Medical Imaging. Philadelphia and New York: Adam hilger, Bristol, 1998.

[13] Axel L, "Cerebral bolld flow determination by rapid sequence computed tomography. Radiology," Radiology, vol. 137, pp. 679-686, 1980.

[14] Bryan RN, Levy LM, Whitlow WD, Killian JM, Preziosi TJ, Rosario JA, "Diagnosis of acute cerebral infarction: comparison of CT and MR imaging," Am J Neuroradiol, vol. 12, pp. 611-620, 1991.

[15] Rivers CS, Wardlaw JM, Armitage PA, Bastin ME, Carpenter TK, Cvoro V, Hand PJ and Dennis MS, "Do acute diffusion- and perfusion-weighted MRI lesions identify final infarct volume in ischemic stroke," Stroke, vol. 37, pp. 98-104, 2006.

[16] Friston KJ, Frith CD, Liddle PF, Frackowiak RS, "Functional connectivity: the principal-component analysis of large (PET) data sets," J Cereb Blood Flow Metab, vol. 13, pp. 5-14, 1993.

[17] Biswal BB, Yetkin FZ, Haughton VM, Hyde JS, "Functional connectivity in the motor cortex of resting human brain using echo-planar MRI," Magnetic resonance in medicine, vol. 34, pp. 537-41, 1995.

[18] Lowe MJ, Mock BJ and Sorenson JA, "Functional Connectivity in Single and Multislice Echoplanar Imaging Using Resting-State Fluctuations," NeuroImage, vol. 7, pp. 119-132, 1998.

[19] Karonen JO, Vanninen RL, Liu Y, Østergaard L, Kuikka JT, Nuutinen J, Vanninen EJ, "Combined diffusion and perfusion MRI with correlation to single-photon emission CT in acute ischemic stroke: ischemic penumbra predits infarct growth," Stroke, vol. 30, pp. 1583-1590, 1999.

[20] von Kummer R, Allen KL, Holle R, Bozzao L, Bastianello S, Manelfe C, Bluhmki E, Ringleb P, Meier DH, Hacke W, "Acute stroke: usefulness of early CT findings before thrombolytic therapy," Radiology, vol. 205, pp. 327-333, 1997.

[21] Yuh, WT, Crain MR, Loes DJ, Greene GM, Ryals TJ, Sato Y, "MR imaging of cerebral ischemia: findings in the first 24 hours," Am J Neuroradiol, vol. 12, pp. 621-629, 1991.

[22] Perkio, J., Aronen H. J., Kangasmaki A., Liu Y., Karonen J., Savolainen S., and Ostergaard L., "Evaluation of four postprocessing methods for determination of cerebral blood volume and mean transit time by dynamic susceptibility contrast imaging," Magn Reson Med, vol. 47, pp. 973-81, May 2002.

[23] Murase, K., Yamazaki Y., and Shinohara M., "Autoregressive moving average (ARMA) model applied to quantification of cerebral blood flow using dynamic susceptibility contrast-enhanced magnetic resonance imaging," Magn Reson Med Sci, vol. 2, pp. 85-95, Jul 1 2003.

[24] Lee, M. C., Cha S., Chang S. M., and Nelson S. J., "Partial-volume model for determining white matter and gray matter cerebral blood volume for analysis of gliomas," J Magn Reson Imaging, vol. 23, pp. 257-66, Mar 2006.

[25] Thompson HK, Jr., Starmer CF, Whalen RE, and McIntosh HD, "Indicator Transit Time Considered as a Gamma Variate," Circ Res, vol. 14, pp. 502-15, Jun 1964.

[26] Rempp KA, Brix G, Wenz F, Becker CR, Guckel F, and Lorenz WJ, "Quantification of regional cerebral blood flow and volume with dynamic susceptibility contrast-enhanced MR imaging," Radiology, vol. 193, pp. 637-41, Dec 1994.

[27] Wu, Y, An H, Krim H, and Lin W, "An independent component analysis approach for minimizing effects of recirculation in dynamic susceptibility contrast magnetic resonance imaging," J Cereb Blood Flow Metab, Jul 19 2006.

[28] Røhl L, Østergaard L, Simonsen CZ, Vestergaard-Poulsen P, Andersen G, Sakoh M, Le Bihan D, Gyldensted C, "Viability Thresholds of Ischemic Penumbra of Hyperacute Stroke Defined by Perfusion-Weighted MRI and Apparent Diffusion Coefficient," Stroke, vol. 32, pp. 1140-1146, 2001.

[29] Dohmen C, Kumura E, Rosner G, Heiss WD, Graf R, "Adenosine in relation to calcium homeostasis: comparison between gray and white matter ischemia," J Cereb Blood Flow Metab, vol. 21, pp. 503-510, 2001.

[30] Stys PK, Ransom BR, Waxman SG, Davis PK, "Role of extracellular calcium in anoxic injury of mammalian central white matter," Proc Natl Acad Sci, vol. 87, pp. 4212-4216, 1990.

[31] Arakawa S, Wright PM, Koga M, Phan TG, Reutens DC, Lim I, Gunawan MR, Ma H, Perera N, Ly J, Zavala J, Fitt G, Donnan GA, "Ischemic thresholds for gray and white matter: a diffusion and perfusion magnetic resonance study," Stroke, vol. 37, pp. 1211-1216, 2006.

[32] Bristow MS, Simon JE, Brown RA, Eliasziw M, Hill MD, Coutts SB, Frayne R, Demchuk AM, Mitchell JR, "MR perfusion and diffusion in acute ischemic stroke: human gray and white matter have different thresholds for infarction," J Cereb Blood Flow Metab, vol. 25, pp. 1280-1287, 2005.

[33] Kwong KK, Belliveau JW, Chesler DA, Goldberg IE, Weisskoff RM, Poncelet BP, Kennedy DN, Hoppel BE, Cohen MS, Turner R, et al, "Dynamic magnetic resonance imaging of human brain activity during primary sensory stimulation," Proceedings of the National Academy of Sciences, vol. 89, pp. 5675-9, 1992.

[34] Ogawa S, Lee TM, Kay AR and Tank DW, "Brain Magnetic Resonance Imaging with Contrast Dependent on Blood Oxygenation," Proceedings of the National Academy of Sciences, vol. 87, pp. 9868-9872, 1990.

[35] Ogawa S, Tank DW, Menon R, Ellermann JM, Kim S, Merkle H and Ugurbil K, "Intrinsic Signal Changes Accompanying Sensory Stimulation: Functional Brain Mapping with Magnetic Resonance Imaging," Proceedings of the National Academy of Sciences, vol. 89, pp. 5951-5955, 1992.

[36] Anderson AW, Marois R, Colson ER, Peterson BS, Duncan CC, Ehrenkranz RA, Schneider KC, Gore JC and Ment LR, "Neonatal auditory activation detected by functional magnetic resonance imaging," Magnetic Resonance Imaging, vol. 19, pp. 1-5, 2001.

[37] Beckmann CF, DeLuca M, Devlin JT and Smith SM, "Investigations into resting-state connectivity using independent component analysis," Philosophical Transactions of the Royal Society, vol. 360, pp. 1001-1013, 2005.

[38] Cordes D, Haughton VM, Arfanakis K, Wendt GJ, Turski PA, Moritz CH, Quigley MA and Meyerand ME, "Mapping Functionally Related Regions of Brain with Functional Connectivity MR Imaging," American Journal of Neuroradiology, vol. 21, pp. 1636-1644, 2000.

[39] Biswal BB, Kylen JV and Hyde JS, "Simultaneous Assessment of Flow and BOLD Signals in Resting-State Functional Connectivity Maps," 1997.

[40] Percival DB, Walden AT, "Wavelet Methods for Time Series Analysis," 2000.

[41] Bullmore E, Fadili J, Maxim V, Sendur L, Whitcher B, Suckling J, Brammer M, and Breakspaer M, "Wavelets and functional magnetic resonance imaging of the human brain," NeuroImage, vol. 23, pp. 234-249, 2004.

[42] Achard S, Salvador R, Whitcher B, Suckling J, and Bullmore E, "A Resilient, Low-Frequency, Small-World Human Brain Functional Network with Highly Connected Association Cortical Hubs," The Journal of Neuroscience, vol. 26, pp. 63-72, 2006.

[43] Ma L, Wang B, Chen X and Xiong J, "Detecting functional connectivity in the resting brain: a comparison between ICA and CCA," Magnetic Resonance Imaging, vol. 25, pp. 47-56, 2007.

[44] van de Ven VG, Formisano E, Prvulovic D, Roeder CH and Linden DEJ, "Functional connectivity as revealed by spatial independent component analysis of fMRI measurements during rest," Human Brain Mapping, vol. 22, pp. 165-178, 2004.

[45] McKeown MJ, Makeig S, Brown GG, Jung TP, Kindermann SS, Bell AJ, Sejnowski TJ, "Analysis of fMRI data by blind separation into independent spatial components," Hum Brain Mapp, vol. 6, pp. 160-188, 1998.

[46] Kiviniemi V, Kantola JH, Jauhiainen J, Hyvärinen A and Tervonen O, "Independent component analysis of nondeterministic fMRI signal sources," NeuroImage, vol. 19, pp. 253-260, 2003.

[47] Rosen, B. R., Belliveau J. W., Aronen H. J., Kennedy D., Buchbinder B. R., Fischman A., Gruber M., Glas J., Weisskoff R. M., and Cohen M. S., "Susceptibility contrast imaging of cerebral blood volume: human experience," Magnetic Resonance in Medicine, vol. 22, pp. 293-9; discussion 300-3, 1991.

[48] Rosen, B. R., Belliveau J. W., Vevea J. M., and Brady T. J., "Perfusion imaging with NMR contrast agents," Magnetic Resonance in Medicine, vol. 14, pp. 249-65, 1990.

[49] De Crespigny, A. J., Wendland M. F., Derugin N., Kozniewska E., and Moseley M. E., "Real-time observation of transient focal ischemia and hyperemia in cat brain," Magnetic Resonance in Medicine, vol. 27, pp. 391-7, 1992.

[50] Ostergaard, L., Weisskoff R. M., Chesler D. A., Gyldensted C., and Rosen B. R., "High resolution measurement of cerebral blood flow using intravascular tracer bolus passages. Part I: Mathematical approach and statistical analysis," Magnetic Resonance in Medicine, vol. 36, pp. 715-25, 1996.

[51] Ostergaard, L., Johannsen P., Host-Poulsen P., Vestergaard-Poulsen P., Asboe H., Gee A. D., Hansen S. B., Cold G. E., Gjedde A., and Gyldensted C., "Cerebral blood flow measurements by magnetic resonance imaging bolus tracking: comparison with [(15)O]H2O positron emission tomography in humans," Journal of Cerebral Blood Flow & Metabolism, vol. 18, pp. 935-40, 1998.

[52] Ostergaard, L., Smith D. F., Vestergaard-Poulsen P., Hansen S. B., Gee A. D., Gjedde A., and Gyldensted C., "Absolute cerebral blood flow and blood volume measured by magnetic resonance imaging bolus tracking: comparison with positron emission tomography values," Journal of Cerebral Blood Flow & Metabolism, vol. 18, pp. 425-32, 1998.

[53] Yamauchi, H., Fukuyama H., Nagahama Y., Nabatame H., Nakamura K., Yamamoto Y., Yonekura Y., Konishi J., and Kimura J., "Evidence of misery perfusion and risk for recurrent stroke in major cerebral arterial occlusive diseases from PET," Journal of Neurology, Neurosurgery & Psychiatry, vol. 61, pp. 18-25, 1996.

[54] David L Thomas, Mark F Lythgoe, Gaby S Pell, Fernando Calamante and Roger J Ordidge, "The measurement of diffusion and perfusion in biological systems using magnetic resonance imaging," Phys. Med. Biol, vol. 45, pp. 97-138, 2000.

[55] KL, Zierler, "Theoretical basis of indicator-dilution methods for measuring flow and volume," Circ. Res., vol. 10, pp. 393-407, 1962.

[56] KL, Zieler, "Equations for measuring blood flow by external monitoring of radioisotopes," Circ. Res., vol. 16, pp. 309-321, 1965.

[57] Østergaard L, Weisskoff RM, Chesler DA, Gyldensted C, Rosen BR, "High resolution measurement of cerebral blood flow using intravascular tracer bolus passages. Part I: mathematical approach and statistical analysis," Magnetic resonance in medicine, vol. 36, pp. 715-725, 1996.

[58] Calamante F, Gadian DG, Connelly A, "Connelly A, Delay and dispersion effects in dynamic susceptibility contrast MRI: simulation using singular value decomposition," Magnetic resonance in medicine, vol. 44, pp. 466-473, 2000.

[59] Marquardt, DW, "An algorithm for least squares estimation of non-linear parameters," J Sot Ind. Appl. Math, vol. 11, 1963.

[60] Levenberg, K, "A method for the solution of certain problem in least squares," Quart. Appl. Math, vol. 2, pp. 164-168, 1944.

[61] Wu, O., Ostergaard L., Weisskoff R. M., Benner T., Rosen B. R., and Sorensen A. G., "Tracer arrival timing-insensitive technique for estimating flow in MR perfusion-weighted imaging using singular value decomposition with a block-circulant deconvolution matrix," Magn Reson Med, vol. 50, pp. 164-74, Jul 2003.

[62] Jones, T. H., Morawetz R. B., Crowell R. M., Marcoux F. W., FitzGibbon S. J., DeGirolami U., and Ojemann R. G., "Thresholds of focal cerebral ischemia in awake monkeys," J Neurosurg, vol. 54, pp. 773-82, Jun 1981.

[63] Ueda, T., Sakaki S., Yuh W. T., Nochide I., and Ohta S., "Outcome in acute stroke with successful intra-arterial thrombolysis and predictive value of initial single-photon emission-computed tomography," J Cereb Blood Flow Metab, vol. 19, pp. 99-108, Jan 1999.

[64] Bell, B. A., Symon L., and Branston N. M., "CBF and time thresholds for the formation of ischemic cerebral edema, and effect of reperfusion in baboons," J Neurosurg, vol. 62, pp. 31-41, Jan 1985.

[65] Morawetz, R. B., Jones T. H., Ojemann R. G., Marcoux F. W., DeGirolami U., and Crowell R. M., "Regional cerebral blood flow during temporary middle cerebral artery occlusion in waking monkeys," Acta Neurol Scand Suppl, vol. 64, pp. 114-5, 1977.

[66] Morawetz, R. B., DeGirolami U., Ojemann R. G., Marcoux F. W., and Crowell R. M., "Cerebral blood flow determined by hydrogen clearance during middle cerebral artery occlusion in unanesthetized monkeys," Stroke, vol. 9, pp. 143-9, Mar-Apr 1978.

[67] Morawetz, R. B., Crowell R. H., DeGirolami U., Marcoux F. W., Jones T. H., and Halsey J. H., "Regional cerebral blood flow thresholds during cerebral ischemia," Fed Proc, vol. 38, pp. 2493-4, Oct 1979.

[68] Carter, L. P., Crowell R. M., Sonntag V. K., and Spetzler R. F., "Cortical blood flow during extracranial-intracranial bypass surgery," Stroke, vol. 15, pp. 836-9, Sep-Oct 1984.

[69] Gaines, C., Carter L. P., and Crowell R. M., "Comparison of local cerebral blood flow determined by thermal and hydrogen clearance," Stroke, vol. 14, pp. 66-9, Jan-Feb 1983.

[70] Pena, H., Gaines C., Suess D., Crowell R. M., Waggener J. D., and DeGirolami U., "Effect of mannitol on experimental focal ischemia in awake monkeys," Neurosurgery, vol. 11, pp. 477-81, Oct 1982.

[71] Marcoux, F. W., Morawetz R. B., Crowell R. M., DeGirolami U., and Halsey J. H., Jr., "Differential regional vulnerability in transient focal cerebral ischemia," Stroke, vol. 13, pp. 339-46, May-Jun 1982.

[72] Latchaw, Richard E., Yonas Howard, Hunter George J., Yuh William T.C., Ueda Toshihiro, Sorensen A. Gregory, Sunshine Jeffrey L., Biller Jose, Wechsler Lawrence, Higashida Randall, and Hademenos George, "Guidelines and Recommendations for Perfusion Imaging in Cerebral Ischemia: A Scientific Statement for Healthcare Professionals by the Writing Group on Perfusion Imaging, From the Council on Cardiovascular Radiology of the American Heart Association, 10.1161/01.STR.0000064840.99271.9E," Stroke, vol. 34, pp. 1084-1104, April 1, 2003 2003.

[73] Astrup, J., Siesjo B. K., and Symon L., "Thresholds in cerebral ischemia - the ischemic penumbra," Stroke, vol. 12, pp. 723-5, Nov-Dec 1981.

[74] Lee, T. Y., Murphy B. D., Aviv R. I., Fox A. J., Black S. E., Sahlas D. J., Symons S., Lee D. H., Pelz D., Gulka I. B., Chan R., Beletsky V., Hachinski V., Hogan M. J., Goyal M., Demchuk A. M., and Coutts S. B., "Cerebral blood flow threshold of ischemic penumbra and infarct core in acute ischemic stroke: a systematic review," Stroke, vol. 37, p. 2201; author reply 2203, Sep 2006.

[75] Murphy, B. D., Fox A. J., Lee D. H., Sahlas D. J., Black S. E., Hogan M. J., Coutts S. B., Demchuk A. M., Goyal M., Aviv R. I., Symons S., Gulka I. B., Beletsky V., Pelz D., Hachinski V., Chan R., and Lee T. Y., "Identification of penumbra and infarct in acute ischemic stroke using computed tomography perfusion-derived blood flow and blood volume measurements," Stroke, vol. 37, pp. 1771-7, Jul 2006.

[76] Alsop, D. C., Detre J. A., and Grossman M., "Assessment of cerebral blood flow in Alzheimer's disease by spin-labeled magnetic resonance imaging," Ann Neurol, vol. 47, pp. 93-100, Jan 2000.

[77] Wang, J., Alsop D. C., Li L., Listerud J., Gonzalez-At J. B., Schnall M. D., and Detre J. A., "Comparison of quantitative perfusion imaging using arterial spin labeling at 1.5 and 4.0 Tesla," Magn Reson Med, vol. 48, pp. 242-54, Aug 2002.

[78] Detre, J. A., Zhang W., Roberts D. A., Silva A. C., Williams D. S., Grandis D. J., Koretsky A. P., and Leigh J. S., "Tissue specific perfusion imaging using arterial spin labeling," NMR Biomed, vol. 7, pp. 75-82, Mar 1994.

[79] van Osch, M. J. P., Vonken E. P. A., Bakker C. J. G., and Viergever M. A., "Correcting partial volume artifacts of the arterial input function in quantitative cerebral perfusion MRI," Magnetic Resonance in Medicine, vol. 45, pp. 477-485, 2001.

[80] Chen, J. J., Smith M. R., and Frayne R., "The impact of partial-volume effects in dynamic susceptibility contrast magnetic resonance perfusion imaging," J Magn Reson Imaging, vol. 22, pp. 390-9, Sep 2005.

[81] Carroll, T. J., Haughton V. M., Rowley H. A., and Cordes D., "Confounding effect of large vessels on MR perfusion images analyzed with independent component analysis," AJNR Am J Neuroradiol, vol. 23, pp. 1007-12, Jun-Jul 2002.

[82] Chen, J. J., Smith M. R., and Frayne R., "Advantages of frequency-domain modeling in dynamic-susceptibility contrast magnetic resonance cerebral blood flow quantification," Magn Reson Med, vol. 53, pp. 700-7, Mar 2005.

[83] Lin, W., Celik A., Derdeyn C. P., An H., Lee Y. Z., Videen T., Ostergaard L., and Powers W. J., "Minimizing inaccuracy and variability for quantitative estimates of CBF in unilateral carotid artery occlusion patients: a PET and MR study," J Magn Reson Imaging, vol. 14, pp. 659-667, April 21-27, 2001 2001.

[84] Selvathi D, Arulmurgan A, Thamarai Selvi S, Alagappan S, "MRI image segmentation using unsupervised clustering techniques," ICCIMA'05, 2005.

[85] Zhang Y, Brady M, Smith S, "Segmentation of brain MR images through a hidden Markov random field model and the expectation-maximization algorithm," IEEE Transactions on medical imaging, vol. 20, pp. 45-57, January 2001.

[86] Rogowska J, Preston K, Hunter GJ, Hamberg L, Kwong K, Saloun O, Wolf GL, "Applications of similarity mapping in dynamic MRI," IEEE Transactions on medical imaging, vol. 14, pp. 480-486, 1995.

[87] Wiart M, Rognin N, Berthezene Y, Nighoghossian N, Froment JC and Baskurt A, "Perfusion-based segmentation of the human brain using similarity mapping," Magnetic resonance in medicine, vol. 45, pp. 261-268, 2001.

[88] Martel AL, Moody AR, Allder SJ, Delay GS, Morgan PS, "Extracting parametric images from dynamic contrast-enhanced MRI studies of the brain using factor analysis," Medical image analysis, vol. 5, pp. 29-39, 2001.

[89] Kao YH, Guo WY, Wu YT, Liu KC, Chai WY, Lin CY, Hwang YS, Liou AJK, Wu HM, Cheng HC, Yeh, TC, Hsieh JC, and Teng MMH, "Hemodynamic segmentation of MR brain perfusion images using independent component analysis, thresholding, and Bayesian estimation," Magnetic resonance in medicine, vol. 49, pp. 885-894, 2004.

[90] Wu YT, Chou YC, Guo WY, Yeh TC and Hsieh JC, "Classification of spatiotemporal hemodynamics from brain perfusion MR images using expectation-maximization estimation with finite mixture of multivariate Gaussian distributions," Magnetic resonance in medicine, vol. 57, pp. 181-191, 2007.

[91] Maronna R, Martin D, Yohai V, Robust statistics - theory and methods: Wiley, 2006.

[92] Huber PJ, Robust statistics: Wiley, 1981 (republished in paperback, 2004).

[93] Hampel FR, Ronchetti EM, Rousseeuw PJ, Stahel WA, Robust statistics - the approach based on influence functions: Wiley, 1986 (republished in paperback, 2005).

[94] Rousseeuw PJ, Leroy AM, Robust regression and outlier detection: Wiley, 1987 (republished in paperback, 2003).

[95] Rousseeuw PJ, "Least median of squares regression," Journal of the American Statistical Association, vol. 79, pp. 871-880, 1984.

[96] Rousseeuw PJ, Multivariate estimation with high breakdown point vol. B: Reidel Publishing Company, Dordrecht, 1985.

[97] Rousseeuw PJ, Van Driessen K, "A fast algorithm for the minimum covariance determinant estimator," Technometrics, vol. 41, pp. 212-223, 1999.

[98] Hubert M, Rousseeuw PJ, Verboven S, "A fast robust method for principal components with applications to chemometrics," Chemometrics and Intelligent Laboratory Systems, vol. 60, pp. 101-111, 2002.

[99] Hubert M, and Engelen S, "Robust PCA and classification in biosciences," Bioinformatics, vol. 20, pp. 1728-1736, 2004.

[100] Hubert M, Rousseeuw PJ, Vanden Branden K, "ROBPCA: a new approach to robust principal components analysis," Technometrics, vol. 47, pp. 64-79, 2005.

[101] Schwarz G, "Estimating the dimension of a model," Ann Statist, vol. 6, pp. 461-464, 1978.

[102] Peel D, McLachlan GJ, "Robust mixture modelling using the t distribution," Statistics and Computing, vol. 10, pp. 339-348, 2000.

[103] Chen S, Wang H, Luo B, "Greedy EM algorithm for robust t-mixture modeling," Proc. of ICIG'04, IEEE, 2004.

[104] van den Boomgaard, van Balen, "Image transforms using bitmapped binary images," Computer vision, graphics, and image processing: graphical models and image processing, vol. 54, pp. 254-258, May 1992.

[105] Haralick RM, Shapiro LG, Computer and robot vision vol. I: Addison-Wesley, 1992.

[106] Haralick RM, Shapiro LG, Computer and robot vision vol. I: Addison-Wesley, 1992.

[107] Soille P, Morphological Image Analysis: Principles and Applications: Springer-Verlag, 1999.

[108] Jolliffe I.T., Principal component analysis, 2nd ed. NY: Springer, 2002.

[109] Smith Lindsay I, "A tutorial on principal components analysis," Feb 26 2002.

[110] Lange KL, Little RJA, Taylor JMG, "Robust statistical modeling using the t distribution," Journal of the American Statistical Association, vol. 84, pp. 881-896, 1989.

[111] de Ridder, and V. Franc, "subspace mixture models using t-distributions," Proceedings of the British machine vision conference 2003, Norwich, UK, 2003.

[112] Shy Shoham, Matthew R Fellow, and Richard A. Normann, "Robust, automatic spike sorting using mixtures of multivariate t-Distribution," J Neurosci Methods, pp. 111-122, 2003.

[113] Woods RP, Grafton ST, Holmes CJ, Cherry SR, Mazziotta JC, "Automated image registration: I. General methods and intrasubject, intramodality validation," Journal of Computer Assisted Tomography, vol. 22, pp. 139-152, 1998.

[114] Woods RP, Grafton ST, Watson JDG, Sicotte NL, Mazziotta JC, "Automated image registration: II. Intersubject validation of linear and nonlinear models," Journal of Computer Assisted Tomography, pp. 153-165, 1998.

[115] Sejnowski, A. Bell and T.J., "An Information-Maximization Approach to Blind Separation and Blind Deconvolution," Neural Computation, vol. 7, pp. 1129-1159, 1995.

[116] Hansen, L. K. and Larsen, J. and Kolenda, T, "Blind Detection of Independent Dynamic Components," In proc. IEEE ICASSP'2001, vol. 5, pp. 3197--3200, 2001.

[117] Chugani, H. T., Phelps, M. E. and Mazziotta, J. C., "Positron emission tomography study of human brain functional development," Ann. Neurol. 22 (1987), pp. 487–497.

[118] Percival DB and Walden AT, "Wavelet Methods for Time Series Analysis," Cambridge: Cambridge University Press, 2000.

Biography

Quan Zhu earned the BSEE and MSEE degree from the Communication University of China (previously the Beijing Broadcast Institute) in Beijing, China, in 1998 and 2001, respectively, and the MSEE degree from Duke University, Durham, in 2003. Her research interests are statistical signal/image processing. She has been a professional member of American Heart Association and American Stroke Association since September 2007. She was awarded Trainee Research Prize for the scientific presentation titled: Correlation analysis in multiple frequency range for functional brain connectivity in normal pediatric subjects at the 93rd Scientific Assemble and Annual Meeting of the Radiological Society of North America in November 2007.